PhD Thesis

Doctoral Program Science and Technology of New Materials

Phosphate-based catalysts for the WGS reaction: Synthesis, reactivity and mechanistic considerations

Sara Mª Navarro Jaén

Supervisors

Oscar Hernando Laguna Espitia

José Antonio Odriozola Gordon

Chapter I

General Introduction

1.1. History and background of the Water-Gas Shift reaction

The production of water gas (Eq. 1.1), consisting in an equimolar mixture of CO and H_2, was first discovered in 1780 by the Italian researcher Felice Fontana, when he quenched incandescent coke with water under a glass bell jar. The composition of the mixture was later determined by Lavoisier [1-3].

$$C + H_2O \leftrightarrow CO + H_2 \qquad \text{Eq. 1.1}$$

Nevertheless, the reaction was first patented in 1888 by Ludwig Mond and Carl Langer [4], whose work was focused on the ammonia synthesis from coal and coke. Mond developed the producing process of the so-called Mond gas, which is the reaction product obtained from the reaction of air and steam passed through coal/coke (CO_2, CO, H_2, N_2, …) [2, 5], which became the basis for future coal gasification processes. Mond and Langer were also the pioneers using fuel cells, feed with coal-derived Mond gas [6].

However, feeding pure hydrogen to the fuel cell was a hard task, since large amounts of CO were present in the Mond gas, thus poisoning the Pt electrode. Therefore, Mond solved this problem by passing a mixture of the Mond gas and steam through finely divided nickel at 400 °C, producing CO_2 and more H_2. After CO_2 elimination by alkaline wash, the H_2-rich stream could be feed to the fuel cell [2, 5, 7]. Consequently, the Water-Gas Shift reaction (WGS, Eq. 1.2) was discovered.

$$CO + H_2O \leftrightarrow CO_2 + H_2 \qquad \text{Eq. 1.2}$$

In 1914, an industrial application of the WGS reaction was found in the production of water gas within the Haber-Bosch process [8] for the synthesis of ammonia. Bosch and Wild discovered that when the water gas coming from reforming processes was passed through an iron-chromium (Fe-Cr) catalyst at 450-600 °C, the CO was converted into CO_2 by means of the WGS reaction [9]. Afterwards, a second stage was introduced on the process, using the same catalyst but operating in the 320-360 °C temperature range and reducing the CO content to 3000-4000 ppm. Due to the operation temperatures of the Fe-based catalysts, they were denominated high-temperature (HT) catalysts. The discovery in the 1960s of the Cu-based low-temperature (LT) catalyst, which operated at lower temperatures, together with the improvements in the HT Fe-based catalysts,

gave rise to an enhancement in the CO reduction content, being below a 0.5% of the reformate steam [2, 10].

As a fundamental part of ammonia synthesis and coal gasification to produce hydrogen, the WGS reaction still maintains an important position in the chemical industry. Nowadays, the WGS reaction is carried out in two adiabatic reactors, one operating at high temperature (350-450 °C) using HT Fe-Cr catalysts, and a second one operating at low temperature (190-250 °C) using Cu-based catalysts [11]. In order to meet the increased demand of hydrogen production, natural gas instead of coal has been used as feedstock and the catalysts formulations have been improved in order to increase the yields and adjust the H_2-to-CO ratio of the product, mainly for ammonia and methanol synthesis but also for Fischer-Tropsch processes and refining operations [5].

Additionally, during the last two decades, the WGS reaction has attracted great interest as an important stage within fuel cell technology. Fuel cells generating electricity from the reaction of hydrogen with oxygen have became popular for their use in transport applications, among others [9]. Since this work will be focused on the study of the WGS reaction within this context, further details about the aspects to be considered are presented in the next section.

1.2. Fuel cell technology for mobile applications and Water-Gas Shift reaction

The use of fuel cells for mobile applications emerges as a consequence of the depletion of fossil fuels and the environmental problems derived from their use [12-14]. In the search for new energy sources, the use of hydrogen as energy vector has been highlighted, since it is considered the cleanest energy option, it can be stored and transported easily and burns producing only water as byproduct; additionally, hydrogen possesses a high calorific value (122 $kJ \cdot g^{-1}$) [15], being a perfect candidate to replace fossil fuels [16-18]. Thus, hydrogen can be exploited as energy carrier in hydrogen-fuel cells, which use the chemical energy of the hydrogen to produce electricity. These devices could be able to replace the typical internal combustion engines in motorized vehicles [18].

The most promising fuel cell technology for transport applications seems to be the Polymer Electrolyte Membrane Fuel Cell (PEMFC) [19-21]. A schematic diagram of the overall process

taking place on it is presented in Figure 1.1. Hydrogen is ionized to protons and electrons at the anode of the cell and, afterwards, protons migrate through a membrane to the cathode, where the reaction to produce water takes place.

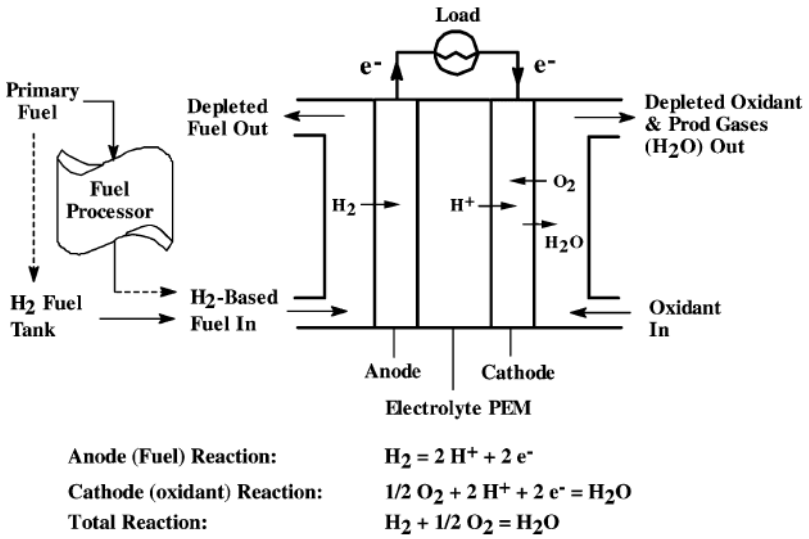

Figure 1.1. Schematic diagram of the PEMFC. Reprinted from [22]

A fundamental aspect to take into account for the successful application of the PEMFCs is the purification of the hydrogen feed. Since the hydrogen is generally produced from reforming processes, the presence of CO traces on the feed is unavoidable [22, 23]. Considering that the anode of the cell is typically consisting on Pt, which is poisoned by irreversible adsorption of CO [24, 25], the reduction of the latter until levels < 10 ppm is mandatory. Among the fuel processing stages used for this purpose, the WGS reaction constitutes the most important process, since it removes the greatest part of the CO [26].

In this case, the WGS operation conditions change substantially with respect to the industrial ones previously described. For fuel cell applications, the catalyst bed must have a reduced volume and weight in order to be economical; the employed catalyst must be stable to withstand start-up and shut-down conditions and additionally, pre-reduction procedures have to be avoided. In this sense, the industrial Fe and Cu-based catalysts present several drawbacks [9, 18]. For instance, the presence of excess fuel from the reformer induces coke formation on the Fe-based catalyst [27, 28], whereas the Cu-based catalyst is pyrophoric in its reduced state and experiments deactivation in the presence of condensed water, due to leaching of the active phase or formation

of surface carbonates [27-30]. Consequently, the search for alternative catalyst formulations becomes essential.

1.3. Selection of the catalyst: the importance of the WGS reaction mechanism

A considerable number of studies has been already devoted to the search for catalyst formulations able to fulfill the previously mentioned requirements. A general conclusion derived from these studies is the suitability of noble metals for this purpose.

In this context, Au, Pt, Rh and Ru have been widely investigated metals [9]. Nevertheless, Rh and Ru-based catalysts are prone to produce methane by means of the methanation reaction under WGS conditions [31-33], which makes them unsuitable for this reaction. As for Au, it has demonstrated to be an exceptional catalyst in the low temperature range (180-230 °C), whereas Pt presents higher rates and better tolerance to the stream composition than Au from 250 °C [34]. Consequently, WGS studies over Au and Pt catalysts in the low and medium temperature range, respectively, have been extensively studied.

Additionally, the support has demonstrated to play a crucial role with regard to the WGS performance. Noble metals supported on non-reducible supports such as Al_2O_3 or SiO_2 have demonstrated a poor catalytic performance in the WGS reaction [35, 36]. However, catalysts constituted by noble metals supported on partially reduced supports have been proposed as promising materials for the WGS reaction according to the literature. Some typical examples are Au/Fe_2O_3 [37, 38], Au/CeO_2 [38, 39], Au/TiO_2 [40], Pt/CeO_2 [38, 41-43], Pt/ZrO_2 [44], Pt/TiO_2 [45], Pt/Fe_2O_3 [46] or Pd/CeO_2 [47].

The obtained results have allowed to confirm that in noble metal based catalysts, both the active phase and the support have a significant control in the overall performance, in turn influencing the WGS reaction mechanism [48-50]. Two reaction mechanisms have been generally accepted for the WGS reaction: the redox or dissociative mechanism, and the associative or regenerative one.

In the redox mechanism, CO is adsorbed on metal sites, diffuses at the metal/support interface and reacts with lattice oxygen of the support to yield CO_2. This step results in the formation of

oxygen vacancies and consequently, reduction of the support. H_2O adsorbs and dissociates mainly on the reduced sites of the support, thus re-oxidizing them and producing H_2. According to that, this mechanism implies the reaction of the reactants, CO and H_2O, with the surface of the solid [5, 9, 51-53].

In the associative mechanism, CO and H_2O are adsorbed on the catalyst active sites giving rise to the formation of an intermediate such as formate, carbonate or hydrogen carbonate, which reacts or decomposes to generate the reaction products, CO_2 and H_2 [54-56]. The exact location of these intermediates (support, metal site or metal/support interface) remains still controversial [53].

In 2008, Gokhale et al. [57] proposed, based on DFT calculations, that the WGS associative mechanism in Cu catalysts is more favorable to occur through a carboxyl intermediate. Since the activation energy for the formation of a carboxyl group is lower than that for the formation of a formate group, the authors suggest that the intermediate acting during the WGS reaction is a carboxyl group, acting formate groups as spectators. By means of this study, they discard the typical associative mechanism, and stablish that only the redox and the associative carboxyl-mediated mechanism are possible. The favored occurrence of the latter has been afterwards reported by other authors in Cu/CeO_2 catalysts [58, 59]. A graphical representation of the two possible WGS reaction paths is presented in Figure 1.2.

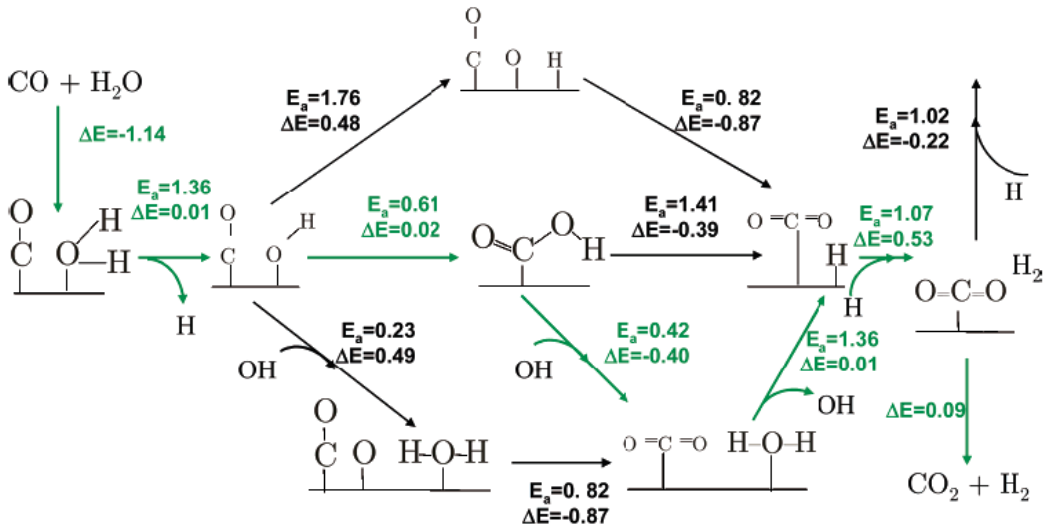

Figure 1.2. Reaction scheme of the redox and carboxyl-mediated WGS mechanisms. Reprinted from [57]

Without regard of the mechanism, the dissociation of H_2O has been generally described as the rate-limiting step [11, 26, 27, 60, 61].

According to the mentioned mechanistic considerations, the superior WGS catalytic performance when using partially reducible oxides (i. e. CeO_2, TiO_2, Fe_2O_3, ZrO_2) with respect to the non-reducible ones, has been attributed to the presence of oxygen vacancies in the support structure, which act as catalytic sites for the dissociation of water [50, 62-64]. The presence of these defects is directly related to the electronic properties of the material, which are influenced by the presence of redox pairs in the support structure [65, 66].

In this context, CeO_2 has been extensively studied as support for the WGS reaction due to its exceptional properties, combining an elevated oxygen storage capacity along with the existence of the Ce^{3+}/Ce^{4+} redox pair in its structure [23, 67]. In addition, this property can be implemented by the addition of doping agents in the CeO_2 lattice [18, 68]. In this sense, González-Castaño et al. [69] enhanced the concentration of oxygen vacancies in a $Pt/CeO_2/Al_2O_3$ catalyst by the addition of Zr and Fe, which resulted in an enhanced mobility of OH and H species during the WGS reaction. This result demonstrated a direct correlation between the concentration of oxygen vacancies and the water dissociation ability of the support. An additional advantage of the Zr and Fe doping was the enhancement of the catalyst resistance towards the formation of carbonaceous species on the catalyst surface.

A similar work was later developed by García-Moncada et al. [11]. In this case, the authors introduced a new concept within WGS catalysts design: the use of ionic conductors, consisting in aliovalent doping of transition or rare earth metal oxides. These compounds provide structural oxygen vacancies, facilitating the diffusion of ions such as O^-, O^{2-}, OH^-, H^+ or H_3O^+, derived from oxygen and water dissociation [70]. By the addition of ZrEu, MoEu and NbEu ionic conductors, the formulation of a $Pt/CeO_2/Al_2O_3$ was significantly enhanced in terms of oxygen vacancies, which had a direct influence on the WGS catalytic performance.

According to these works, two concepts have to be considered for the design of a new generation of WGS catalysts able to overcome the H_2O dissociation step: the presence of cerium in the support structure and the introduction of ionic conduction properties.

Regarding the ionic conduction properties, phosphate-type materials have demonstrated exceptional features.

For instance, alkali orthophosphates have demonstrated great potential for fuel cell and gas sensing applications [71, 72]. The cubic phases of these materials are specially interesting, since PO_4^{3-} groups in face-centered cubic lattices have a high degree of rotational freedom, enhancing proton mobility. Protons are attached to these tetrahedral groups at the vertices of the cubic structure and move from one tetrahedron to another, through the so-called “cog-wheel” or “paddle wheel” mechanism [73]. Zirconium phosphates have been also applied as proton exchange membrane in fuel cells due to their proton conduction properties [74]. Proton transport in these materials are dominated by surface transport through the interlayer regions in the presence of water [75], which is favored by the presence of OH groups in the interlayer region [76]. Particular attention has been paid to rare earth metal phosphates in fields such as fuel cells, gas sensors and ceramic membranes, due to their exceptional thermal and chemical stability. Additionally, it is well-known that these materials undergo phase transformations with the temperature [77, 78], which determines their conduction properties.

Results derived from the aforementioned studies have demonstrated that conduction properties in phosphate-type materials depend on several factors, as the absence or presence of humidity, the population of surface OH groups or the crystal structure of the solid, which influences the acid-base properties and the type and population of structural defects [73, 76, 77].

According to the work of García-Moncada et al. [11] previously mentioned, it could be reasonable the extrapolation of the conduction properties observed in phosphate-type materials to WGS catalytic systems.

Thus, an interesting phosphate-type candidate for this application is $CePO_4$. The presence of cerium in its structure could influence its electronic properties by the existence of the Ce^{3+}/Ce^{4+} redox pair, as reported for CeO_2. Additionally, $CePO_4$ could present two different crystal structures: the rhabdophane-type phase, $CePO_4 \cdot nH_2O$ ($0.5 < n < 1$) or the monazite-type phase, $CePO_4$, schematized in Figure 1.3.

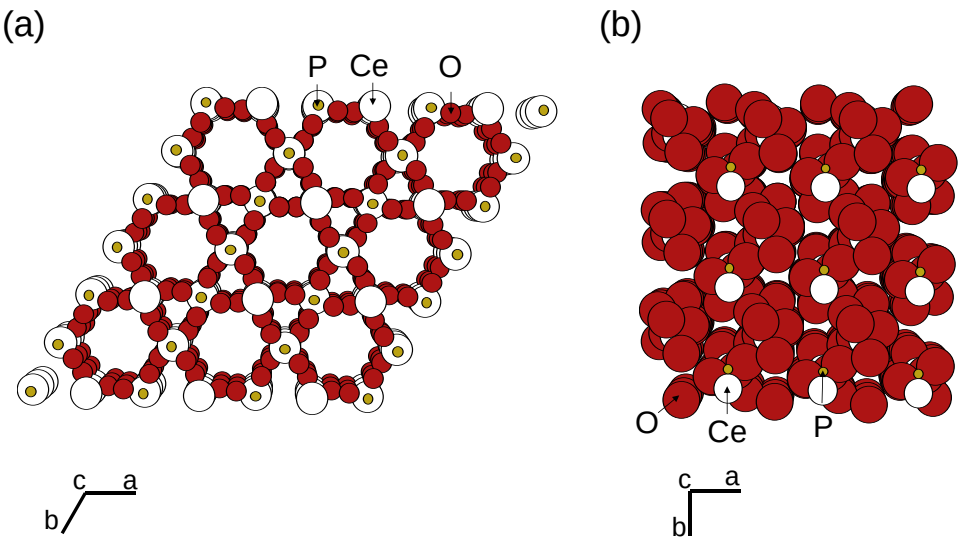

Figure 1.3. View along the *c* axis of (a) rhabdophane-type phase, (b) monazite-type phase of $CePO_4$

The rhabdophane-type phase presents hexagonal structure and contains a series of parallel channels along the *c* axis, where water molecules are located. The monazite-type phase presents monoclinic structure, which results from the complete dehydration of the rhabdophane-type phase [78, 79]. Consequently, the structural differences between both $CePO_4$ phases could be reflected in their conduction properties and therefore, in their behavior during the WGS reaction.

1.4. Objectives and organization of the PhD Thesis

Considering the aforementioned aspects**,** this PhD Thesis will focus on the study of the two phases of $CePO_4$ as supports for Pt WGS catalysts. The synthesis, characterization and catalytic activity results of both supports and catalysts are described and discussed. Additionally, mechanistic studies will be presented in order to elucidate the role of the water molecule in the WGS reaction mechanism over these solids.

This PhD Thesis consists on six chapters, including the present one.

Chapter II presents the fundamentals of the techniques employed along this work, as well as the experimental conditions used.

In Chapter III, the synthesis and physicochemical characterization of the prepared materials is presented and discussed.

Chapter IV deals with the catalytic activity results of the prepared supports and catalysts on the WGS reaction. The obtained catalytic performances are then related to the interaction of the solids with the water molecule and the reactive mixture by means of infrared (IR) spectroscopy studies.

In Chapter V, the structural characteristics of the solids are related to the WGS reaction mechanism observed on them, through the results obtained by ^{18}O and $C^{18}O_2$ isotopic exchange techniques.

Chapter VI presents the preliminary study of Pt catalysts supported on other phosphate-type supports containing Ca and Ti. Their structural features, catalytic behavior on the WGS reaction and interaction with the water molecule are discussed and compared with those observed in the $CePO_4$ systems.

1.5. References

1. Burns, D.T., G. Piccardi, and L. Sabbatini, *Some people and places important in the history of analytical chemistry in Italy.* Microchimica Acta, 2008. **160**: p. 57-87.
2. Mendes, D., et al., *The water-gas shift reaction: from conventional catalytic systems to Pd-based membrane reactors-a review.* Asia-Pacific Journal of Chemical Engineering, 2010. **5**(1): p. 111-137.
3. Lavoisier, A.L., *Oeuvres de Lavoisier*. Vol. 2. 1862, Paris: Imp. Impériale.
4. Mond, L. and C. Langer, *Improvements in obtaining hydrogen. British Patent 12608*. 1888: England.
5. Smirniotis, P. and K. Gunugunuri, *Water Gas Shift Reaction: Research Developments and Applications*. 1st ed. 2015: Elsevier.
6. Hoogers, C., *Fuel Cell Technology Handbook*. 2002: CRC Press.
7. Quirck, R.P., *Kirk-Othmer Encyclopedia of Chemical Engineering Technology*. Vol. 2. 1963: Wiley-VCH.
8. Bosch, C. and W. Wild, *Canadian Patent 153 379*. 1914.
9. Ratnasamy, C. and J.P. Wagner, *Water Gas Shift Catalysis.* Catalysis Reviews, 2009. **51**(3): p. 325-440.
10. Ruettinger, W.F. and O. Ilinich, *Encyclopedia of Chemical Processing*, ed. S. Lee. 2006: Taylor & Francis.
11. García-Moncada, N., et al., *New concept for old reaction: Novel WGS catalyst design.* Applied Catalysis B: Environmental, 2018. **238**: p. 1-5.

12. Höök, M. and X. Tang, *Depletion of fossil fuels and anthropogenic climate change- A review.* Energy Policy, 2013. **52**: p. 797-809.

13. Hoel, M. and S. Kverndokk, *Depletion of fossil fuels and the impacts of global warming.* Resource and Energy Economics, 1996. **18**: p. 115-136.

14. Chiari, L. and A. Zecca, *Constraints of fossil fuels depletion on global warming projections.* Energy Policy, 2011. **39**: p. 5026-5034.

15. Han, S.-K. and H.-S. Shin, *Biohydrogen production by anaerobic fermentation of food waste.* International Journal of Hydrogen Energy, 2004. **29**: p. 569-577.

16. Turner, J.A., *Sustainable Hydrogen Production.* Science, 2004. **305**: p. 972-974.

17. LeValley, T.L., A.R. Richard, and M. Fan, *The progress in water gas shift and steam reforming hydrogen production technologies – A review.* International Journal of Hydrogen Energy, 2014. **39**(30): p. 16983-17000.

18. Pal, D.B., et al., *Performance of water gas shift reaction catalysts: A review.* Renewable and Sustainable Energy Reviews, 2018. **93**: p. 549-565.

19. Trimm, D.L. and Z.I. Önsan, *Onboard Fuel Conversion for Hydrogen-Fuel-Cell-Driven Vehicles.* Catalysis Reviews, 2001. **43**(1-2): p. 31-84.

20. Higier, A., et al., *Polymer electrolyte fuel cell (PEMFC) based power system for long-term operation of leave-in-place sensors in Navy and Marine Corps applications.* International Journal of Hydrogen Energy, 2017. **42**(7): p. 4706-4709.

21. Emonts, B., et al., *Fuell cell drive system with hydrogen generation in test.* Journal of Power Sources, 2000. **86**: p. 228-236.

22. Song, C., *Fuel processing for low-temperature and high-temperature fuel cells: Challenges and opportunities for sustainable development in the 21st century.* Catalysis Today, 2002. **77**: p. 17-49.

23. González-Castaño, M., et al., *O 2 -assisted Water Gas Shift reaction over structured Au and Pt catalysts.* Applied Catalysis B: Environmental, 2016. **185**: p. 337-343.

24. Moreno, B., J.R. Jurado, and E. Chinarro, *Pt–Ru–Co catalysts for PEMFC synthesized by combustion.* Catalysis Communications, 2009. **11**(2): p. 123-126.

25. Chen, C.-Y. and K.-P. Huang, *Performance and transient behavior of the kW-grade PEMFC stack with the Pt Ru catalyst under CO-contained diluted hydrogen.* International Journal of Hydrogen Energy, 2017. **42**(34): p. 22250-22258.

26. González-Castaño, M., et al., *Tailoring structured WGS catalysts: Impact of multilayered concept on the water surface interactions.* Applied Catalysis B: Environmental, 2018. **222**: p. 124-132.

27. Byron, S.R.J., M. Loganathan, and M.S. Shanthaz, *A Review of the Water Gas Shift Reaction Kinetics.* International Journal of Chemical Reactor Engineering, 2010. **8**.

28. Wheeler, C., et al., *The water-gas shift reaction at short contact times.* Journal of Catalysis, 2004. **2223**: p. 191-199.

29. Mhadeshwar, A.B. and D.G. Vlachos, *Is the water-gas shift reaction on Pt simple?: Computer-aided microkinetic model reduction, lumped rate expression, and rate-determining step.* Catalysis Today, 2005. **105**: p. 162-172.

30. Kusar, H., S. Hocevar, and J. Levec, *Kinetics of the water-gas shift reaction over nanostructured copper-ceria catalysts.* Applied Catalysis B: Environmental, 2006. **63**: p. 194-200.

31. Thinon, O., et al., *Screening of bifunctional water-gas shift catalysts.* Catalysis Today, 2008. **137**: p. 29-35.

32. Iizuka, T., Y. Tanaka, and K. Tanabe, *Hydrogenation of CO and CO2 over rhodium catalysts supported on various metal oxides.* Journal of Catalysis, 1982. **76**: p. 1-8.

33. Yaccato, K., et al., *Competitive CO and CO2 methanation over supported noble metal catalysts in high throughput scanning mass spectrometer.* Applied Catalysis A: General, 2005. **296**: p. 30-48.

34. Gonzalez-Castaño, M., et al., *Pt vs. Au in water–gas shift reaction.* Journal of Catalysis, 2014. **314**: p. 1-9.

35. Zhai, Y., et al., *Alkali-stabilized Pt-OHx species catalyze low-temperature water-gas shift reactions.* Science, 2010. **329**(5999): p. 1633-6.

36. Wang, Y., et al., *Silica-encapsulated platinum catalysts for the low-temperature water-gas shift reaction.* Applied Catalysis B: Environmental, 2012. **127**: p. 342-350.

37. Andreeva, D., et al., *Low temperature water gas shift reaction over Au-α-Fe_2O_3.* Journal of Catalysis, 1998. **158**: p. 354-355.

38. Luengnaruemitchai, A., S. Osuwan, and E. Gulati, *Comparative studies of low temperature water gas shift reaction over Pt-CeO_2, Au-CeO_2 and Au-Fe_2O_3 catalysts.* Catalysis Communications, 2003. **4**: p. 215-221.

39. Andreeva, D., et al., *Low temperature water gas shift reaction over Au-CeO_2 catalysts.* Catalysis Today, 2002. **72**: p. 51-57.

40. Boccuzzi, D.F., et al., *Gold, silver and copper catalysts supported on TiO_2 for pure hydrocarbon production.* Catalysis Today, 2002. **75**: p. 169-175.

41. Panagiotopoulou, P., et al., *Water-gas shift activity of doped Pt/CeO_2 catalysts.* Chemical Engineering Journal, 2007. **134**: p. 16-22.

42. Goguet, A., et al., *Study of the origin of the deactivation of a Pt/CeO_2 catalyst during inverse water gas shift (RWGS) reaction.* Journal of Catalysis, 2004. **226**: p. 382-392.

43. Germani, G. and Y. Schuurman, *Water gas shift reaction kinetics over structured Pt-CeO_2/Al_2O_3 catalysts.* AICh.E. Journal, 2006. **52**: p. 1806-1813.

44. Xue, E., M. O'Keefe, and J.R.H. Ross, *Water gas shift conversion using a feed with a low steam to carbon monoxide ratio and containing sulfur.* Catalysis Today, 1996. **30**: p. 107-118.

45. Panagiotopoulou, P. and D.I. Kondarides, *Effect of morphological characteristics of TiO_2-supported noble metal catalysts on their activity for water gas shift reaction.* Journal of Catalysis, 2004. **225**: p. 327-336.

46. Basinska, A., T.P. Maniecki, and W.K. Jozwiak, *Catalytic activity in water gas shift reaction of platinum group metals supported on iron oxide.* Reaction Kinetics and Catalysis Letters, 2006. **89**: p. 319-324.

47. Wang, X., R.J. Gorte, and J.P. Wagner, *Deactivation mechanism for Pd-CeO_2 during the Water-Gas shift reaction.* Journal of Catalysis, 2002. **212**: p. 225-230.

48. Panagiotopoulou, P. and D.I. Kondarides, *Effect of the nature of the support on the catalytic performance of noble metal catalysts for the water–gas shift reaction.* Catalysis Today, 2006. **112**(1-4): p. 49-52.

49. Grenoble, D.C., M.M. Estadt, and D.F. Ollis, *The Chemistry and Catalysis of the Water Gas Shift Reaction, 1. The Kinetics over Supported Metal Catalysts.* Journal of Catalysis, 1981. **67**: p. 90-102.

50. Vecchietti, J., et al., *Understanding the Role of Oxygen Vacancies in the Water Gas Shift Reaction on Ceria-Supported Platinum Catalysts.* ACS Catalysis, 2014. **4**(6): p. 2088-2096.

51. Bunluesin, T., R.J. Gorte, and G.W. Graham, *Studies of the water-gas-shift reaction on ceria-supported Pt, Pd and Rh: Implication for oxygen storage properties.* Applied Catalysis B: Environmental, 1998. **15**: p. 107-114.

52. Hilaire, S., et al., *A comparative study of water-gas shift reaction over ceria-supported metallic catalysts.* Applied Catalysis A: General, 2004. **258**: p. 271-276.

53. Kalamaras, C.M., et al., *Effects of Reaction Temperature and Support Composition on the Mechanism of Water–Gas Shift Reaction over Supported-Pt Catalysts.* The Journal of Physical Chemistry C, 2011. **115**(23): p. 11595-11610.

54. Chenu, E., et al., *Water-gas shift: An examination of Pt promoted MgO and tetragonal and monoclinic ZrO_2 by in situ DRIFTS.* Applied Catalysis B: Environmental, 2005. **59**: p. 45-56.

55. Jacobs, G., et al., *Low-temperature water-gas shift: impact of Pt promoter loading on the partial reduction of ceria and consequences for catalyst design.* Journal of Catalysis, 2005. **229**: p. 499-512.

56. Shido, T. and Y. Iwasawa, *Reactant-Promoted Reaction Mechanism for Water-Gas Shift Reaction on Rh-Doped CeO_2.* Journal of Catalysis, 1993. **141**: p. 71-81.

57. Gokhale, A.A., J.A. Dumesic, and M. Mavrikakis, *On the mechanism of low temperature water gas shift reaction on copper.* Journal of the American Chemical Society, 2008. **130**: p. 1402-1414.

58. Saw, E.T., et al., *High-temperature water gas shift reaction on Ni–Cu/CeO2 catalysts: effect of ceria nanocrystal size on carboxylate formation.* Catalysis Science & Technology, 2016. **6**(14): p. 5336-5349.

59. Graciani, J. and J.F. Sanz, *Designing a new generation of catalysts: Water gas shift reaction example.* Catalysis Today, 2015. **240**: p. 214-219.

60. García-Moncada, N., et al., *A direct in situ observation of water-enhanced proton conductivity of Eu-doped ZrO 2 : Effect on WGS reaction.* Applied Catalysis B: Environmental, 2018. **231**: p. 343-356.

61. Mandapaka, R. and G. Madras, *Zinc and platinum co-doped ceria for WGS and CO oxidation.* Applied Catalysis B: Environmental, 2017. **211**: p. 137-147.

62. González, I.D., et al., *A comparative study of the water gas shift reaction over platinum catalysts supported on CeO2, TiO2 and Ce-modified TiO2.* Catalysis Today, 2010. **149**(3-4): p. 372-379.

63. Li, L., et al., *Black TiO2−x with stable surface oxygen vacancies as the support of efficient gold catalysts for water-gas shift reaction.* Catalysis Science & Technology, 2018. **8**(5): p. 1277-1287.

64. Rajesh, T. and N. Devi, *Role of oxygen vacancies in the water gas shift reaction: activity study on BaCe0.98-xYxPt0.02O3-delta perovskites.* Journal of Physical Chemistry C, 2014. **118**: p. 20867-20874.

65. Zhu, X., et al., *Significant Improvement in Activity and Stability of Pt/TiO2 Catalyst for Water Gas Shift Reaction Via Controlling the Amount of Na Addition.* Catalysis Letters, 2008. **129**(1-2): p. 135-141.

66. Beltrán, J.I., et al., *Oxygen vacancies at Ni/c-ZrO_2.* Journal of the European Ceramic Society, 2003. **23**: p. 2737-2740.

67. Navarro-Jaén, S., et al., *Pt/CePO4 catalysts for the WGS reaction: influence of the water-supplier role of the support on the catalytic performance.* Journal of Materials Chemistry A, 2018. **6**: p. 17001-17010.

68. Ro, H.-S., et al., *Single Stage Water-Gas Shift Reaction over Supported Pt catalysts.* Catalysis Letters, 2011. **141**: p. 95-99.

69. González-Castaño, M., et al., *Deep insight into Zr/Fe combination for successful Pt/CeO2/Al2O3WGS catalyst doping.* Catalysis Science & Technology, 2017. **7**(7): p. 1556-1564.

70. Tilley, R.D.J., *Defects in Solids*. 2008, New Jersey: Wiley.

71. Narayanan, B.K., S.A. Akbar, and P.K. Dutta, *A phosphate-based proton conducting solid electrolyte hydrocarbon gas sensor.* Sensors and Actuators B, 2002. **87**: p. 480-486.

72. Hooper, A., et al., *Ionic conductivity of pure and doped Na_3PO_4.* Journal of the Solid State Chemistry, 1978. **24**: p. 265-275.

73. Kvist, A. and A. Bengtzelius, *Fast Ion Transport in Solids*, ed. W. van Gool. 1973, Amsterdam: North Holland.

74. Hogarth, W.H.J., et al., *Proton conductivity of mesoporous sol-gel zirconium phosphates for fuel cell applications.* Journal of Materials Chemistry, 2004. **15**: p. 754-758.

75. Casciola, M. and D. Bianchi, *Frequency response of polycristalline samples of α-$Zr(HPO_4)_2 \cdot H_2O$ at different relative humidities.* Solid State Ionics, 1985. **17**: p. 287-293.

76. Alberti, G., et al., *On the mechanism of diffusion and ionic transport in crystalline insoluble acid salts of tetravalent metals- I Electrical conductance of zirconium bis (monohydrogen ortho-phosphate) monohydrate with a layered structure.* Journal of Inorganic and Nuclear Chemistry, 1978. **40**: p. 533-537.

77. Anfimova, T., et al., *Thermal Stability and Proton Conductivity of Rare Earth Ortophosphates Hydrates.* International Journal of Electrochemical Science, 2014. **9**: p. 2285-2300.

78. Mooney, R.C.L., *Crystal Structures of a Series of Rare Earth Phosphates.* The Journal of Chemical Physics, 1948. **16**(10): p. 1003-1003.

79. Mooney, R.C.L., *X-ray Diffraction Study of Cerous Phosphate and Related Crystals. I. Hexagonal modification.* Acta Crystallographica, 1950. **3**: p. 337-340.

Chapter II

Physicochemical Characterization Techniques and Catalytic Activity

Abstract

In this chapter, the experimental setups of the employed physicochemical characterization techniques are described, as well as the features of the equipment used for the study of the prepared solids. In addition, a description of the procedure as well as the operation variables during the catalytic test of the prepared materials is presented.

2.1. Physicochemical characterization techniques

2.1.1. Powder X-Ray Diffraction (XRD)

XRD is a non-destructive technique used for studying the structure of crystalline materials. This method may be applied for phase identification, semi-quantitative analysis and determination of structural defects.

XRD phenomena takes place due to the scattering of X-rays with the matter. If the scattered waves are deviated without loss of energy, there are coherent with the incident X-rays thus presenting the same wavelength. This radiation generates the diffraction phenomena. The scattered waves can also lose some of their energy and present longer wavelength than the incident X-rays, being incoherent with the latter. This radiation contributes to the background scattering in diffraction patterns. Therefore, when X-rays interact with the atoms constituting the crystallographic planes of a crystal, the scattered waves are the result of the constructive and destructive interferences of the scattered waves of each atom. Considering that either the position and properties of the atoms influence the scattering, the diffraction of every solid is related to its crystal structure.

The analysis of the diffraction phenomena in crystals is accomplished using the Bragg's law. Bragg hypothesis considers that the planes of atoms constituting a crystal act as semitransparent mirrors. Consequently, when a wave coming from an X-ray beam (1) collides with the crystal, the first plane of atoms reflects it partially (1') with a reflection angle equal to the incident angle (θ), whereas the non-reflected fraction is transmitted to the subsequent planes, where they are partially reflected again (2', 3'), as shown in Figure 2.1.

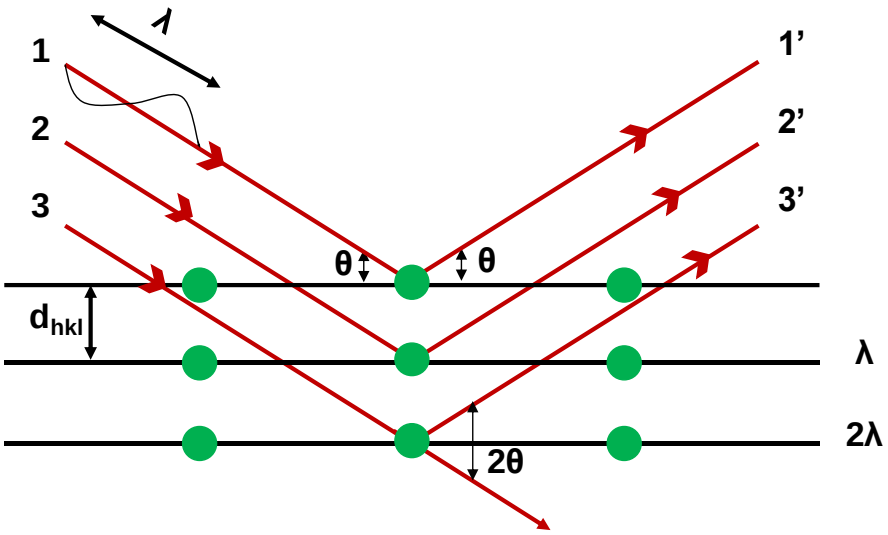

Figure 2.1. Diffraction phenomena described by Bragg's law

If the reflected waves are in-phase, their interference is constructive following the Bragg's law (Eq. 2.1).

$$n\lambda = 2d_{hkl}sen\theta \qquad Eq.\,2.1$$

Where **n** is the diffraction order, **λ** is the incident beam wavelength, **d** is the distance between two consecutive planes and **θ** is the diffraction angle.

Therefore, a family of planes diffracts uniquely if the difference of the traversed path of the scattered waves is a whole multiple of the wavelength. If this condition is not met, the interference is then destructive [1].

Additionally, when parallel monochromatic radiation falls on a randomly oriented group of crystals, a broadening of the diffracted beam takes place if the particle size is small. According to this principle, P. Scherrer obtained an expression that allowed the estimation of the crystalline domain of the solids studied by XRD, known as the Scherrer equation (Eq. 2.2).

$$t = \frac{K\lambda}{\beta cos\theta} \qquad Eq.\,2.2$$

Where **t** is the mean crystallite size, **K** is a numerical constant whose value is $2(\ln 2/\pi)^{1/2} = 0.93$, **λ** is the wavelength of the incident X-rays and **β** is the full-width at half-maximum of the 2θ reflection [2].

XRD patterns of the prepared samples were recorded on a Panalytical X'PERT PRO diffractometer using CuKα radiation (40 mA, 45 kV) over a 2θ range between 10 and 90°, using a step size of 0.05° and a step time of 300 s. The crystal refinements were performed by means of the Rietveld method [3] using FULLPROF software [4]. This method is essentially a multiparameter curve fitting procedure. The model function consists of a parameterized description of a curve that is fitted by least squares to the suite of experimental data points. The peak magnitudes are modeled from crystal structure parameter and their shapes from parameterized functions that are a convolution of instrumental and microcrystalline broadening effects. A Thompson-Cox- Hastings pseudo-Voigt function convoluted with an axial divergence asymmetry function was chosen to generate the peak shapes. The following parameters were refined: background points, zero point, scale factor, pseudo-Voigt parameters of the peak shape, atomic positions and cell parameters. The result of a Rietveld analysis includes crystal structure information (crystal size, crystalline phase fractions). Standard compounds used were $CePO_4 \cdot 0.5H_2O$ ($P6_222$, space group number 180, a = b = 7.0550 Å, c= 6.4390 Å, V= 277.5 $Å^3$), JCPDS-ICDD 01-075-1880 and $CePO_4$ ($P2_1/n$, space group number 14, a= 6.8004 Å, b= 7.0231 Å, c= 6.4717 Å, V= 300.60 $Å^3$), JCPDS-ICDD 00-032-0199.

In situ high-temperature XRD analysis was carried out using a high temperature chamber Anton Paar HTK 1200 coupled with a PHILIPS X'Pert Pro diffractometer equipped with a Cu anode. The diffractograms were recorded under atmospheric air, over a 2θ range between 10 and 90 °, while the temperature was increased from RT to 600 °C with a heating rate of 10 °C min^{-1}.

2.1.2. Inductively Coupled Plasma Atomic Emission Spectrometry (ICP-AES)

ICP-AES constitutes a suitable method for the determination of the chemical composition in solids, since it allows to determine most of the elements present in a sample and a wide range of trace elements.

This technique is based on the emission or absorption of photons occurring when an atom or ion is excited by electromagnetic radiation. In general, quantitative information is related to the amount of emitted or adsorbed radiation, while qualitative information is related to the wavelengths of such radiation [5].

During the analysis, a liquid sample is introduced into a nebulization chamber, where it is transformed into a fine mist, which is decomposed by the heat of plasma to form a cloud of hot gases containing excited free atoms and ions of the studied elements. The emitted radiation goes through a monochromator and finally reaches the detector.

ICP-AES measurements were performed on a Horiba Jobin Yvon spectrometer after acid digestion of the samples.

2.1.3. Thermogravimetric Analysis (TGA) and Differential Thermal Analysis (DTA)

TGA is an analytical technique used to measure the mass change of a sample occurring in response to programmed temperature changes. These mass changes can be produced due to several processes such as decomposition, degradation, sublimation, vaporization, adsorption, desorption, oxidation and reduction. To perform the measurements a thermobalance is used, that is a combination of a sensitive analytical balance with an electronically programmed furnace. The measurements are carried out in a controlled gaseous atmosphere that can be either static or dynamic [6]. Moreover, DTA allows to evaluate the thermal effects produced on a sample because of a temperature change, thus any event involving heat absorption or release can be detected. Therefore, this technique allows the characterization of phase transitions, the study of order-disorder transitions and chemical reactions [7].

The measurements were carried out using a TA Instruments SDT Q600 apparatus from 30 to 900 °C with a heating rate of 10 °C min^{-1} under nitrogen. Weight loss of the sample, derivative of weight and heat flow as a function of time and temperature were recorded.

2.1.4. N_2 physisorption

Specific surface area and porosity are parameters of great importance in heterogeneous catalysis since the catalytic activity is related to the available surface, whereas the reactants transportation and the reaction pathways are influenced by the pore size distribution [8].

Nitrogen adsorption at 77 K is widely used to determine these parameters. The obtained adsorption data are commonly analyzed through the application of the Brunauer-Emmett-Teller (BET) method, consisting on a multilayer extension of Langmuir's kinetic treatment of monolayer adsorption on an array of similar sites, that is, the ideal localized monolayer theory is extended in order to include the formation of either an infinite or finite number of adsorbed layers. The molecules in the first layer are assumed to act as sites for the second-layer molecules, and so on. For the characterization of a porous solid, physisorption measurements are accomplished at constant temperature thus involving the determination of an adsorption isotherm, where the adsorbed gas amount (n_a) is expressed as a function of the equilibrium relative pressure (p/p_0). The adsorption isotherms are represented graphically, and their shapes are associated to the gas-solids interactions and the surface area and porosity of the solid. The surface area value is then obtained from the monolayer capacity, i.e. the nitrogen uptake to form a monolayer on the solid surface. Concerning the analysis of the porosity, pores can be classified according to their sizes [9], as shown in Table 2.1.

Table 2.1. Classification of pores according to their size

Classification	Pore size (nm)
Ultramicropores	Ø < 0.7
Micropores	Ø < 2
Mesopores	2 < Ø< 50
Macropores	Ø > 50

For the analysis of mesoporous solids, the Barrett-Joyner-Halenda (BJH) method is widely used. This method is based on a cylindrical pore model, and it considers the emptying of the pores by a stepwise reduction of p/p_0, by taking into account the thinning of the multilayer in those pores already empty.

Textural properties of the synthesized solids were studied by N_2 adsorption-desorption experiments at 77 K. The measurements were performed in a Micromeritics TriStar II 3020 instrument. Prior to the measurements samples were degassed for 2 hours at 250 °C.

2.1.5. Electron microscopy

Electron microscopy employs a beam of electrons as lightning source, allowing to obtain higher magnification and resolving power than the conventional optical microscopy. Furthermore, electron microscopes allow to perform energy dispersive X-ray spectroscopy (EDX), that provides information about the chemical composition of the samples from the characteristic X-rays produced when the electron beam interacts with the sample.

2.1.5.1. Scanning Electron Microscopy (SEM)

SEM is one of the most versatile techniques to examine and analyze the microstructure morphology and chemical composition of a sample. The produced electron beam is shaped and focus using a series of electromagnetic lenses. The electrons first pass through one or two condenser lenses, which reduces the beam size. An aperture in the condenser lens limits the angular range of electrons that are allowed to travel up to the objective lens, where a final aperture may be positioned. Image formation in SEM depends on the acquisition of the signals produced as a consequence of the interaction between the electron beam and the sample, which are classified mainly in two categories: elastic and inelastic interactions. The deflection of the incident beam by the nucleus or outer shell electrons of the sample with similar energies leads to elastic scattering, characterized for a negligible loss of energy during the collision. Incident electrons scattered through an angle greater than 90°, that is backscattered electrons (BSE), produce an useful signal for imaging the sample. On the other hand, inelastic scattering occurs as a consequence of several interactions between the incident electrons and the electrons and atoms of the sample, giving rise to an energy loss whose value will depend on the binding energy of the electron to the atom and whether the electrons of the sample are excited singly or collectively. This interaction generates secondary electrons (SE) that possess values of energy lower than 50 eV and can be used to image or analyze the sample. In addition to these interactions, other signals are produced when an electron beam collides with a sample including the emission of characteristic X-rays, Auger electrons and cathodoluminescence [10].

SEM micrographs and EDX elemental analysis were performed in a Hitachi S-4800 SEM-FEG high resolution (5 nm) scanning electron

microscope provided with SE and BSE detectors and a Bruker X Flash Detector 4010 EDX analyzer with a resolution of 133 eV in the MnKα line. Operating conditions were varied for every experiment.

2.1.5.2. Transmission Electron Microscopy (TEM)

In TEM, a thin sample is irradiated with a parallel electron beam. An electromagnetic objective lens combines the transmitted electrons, producing a 2D diffraction pattern of the sample in its focal plane, and these diffracted beams are recombined to form the magnified image in the image plane. The variation of the excitation of a series of projection lenses allow to obtain magnified images or the diffraction pattern of the sample on the detector. In conventional TEM, image contrast is generated by insertion of an objective aperture in the diffraction plane, which has a size that allows the diffracted beams to be excluded [11].

TEM micrographs were obtained in a PHILIPS CM-200 transmission electron miscroscope equipped with microanalysis (EDX), with 15 nm of minimum spot size and 2.8 Å of maximum resolution between two points.

2.1.6. X-ray Photoelectron Spectroscopy (XPS)

XPS is a surface-sensitive technique, since the X-ray penetration in the sample is small, with an average depth of analysis of approximately 5 nm. XPS is based on the photoelectric effect. When a sample is irradiated with a light of sufficiently small wavelength, an atom absorbs a photon of energy hv, provoking that a core or valence electron with binding energy E_b is ejected with a given kinetic energy E_k (Eq. 2.3.). The number of emitted photoelectrons depends on the light intensity and the energy of these electrons on the light wavelength.

$$E_k = h\nu - E_b - \phi \qquad Eq.2.3$$

Where $\mathbf{E_k}$ is the kinetic energy of the photoelectron, **h** is the Planck constant, **v** is the frequency of the exciting radiation, $\mathbf{E_b}$ is the binding energy of the photoelectron with respect to the Fermi level of the sample and **ϕ** is the work function of the spectrometer.

The X-ray sources commonly used are Mg Kα (1253.6 eV) and Al Kα (1486.3 eV), and the intensity of photoelectrons N(E) is measured as a function of their kinetic energy. However, the XPS spectrum is usually a plot of N(E) versus the binding energy (E_b). Considering that a set of binding energies is characteristic for an element, XPS can be used to analyze the elemental composition of the samples, the oxidation state of the elements and the dispersion of one phase over another [12].

XPS measurements of the prepared samples were performed using a Phoibos HSA3500 150 R6 MCD-9 spectrometer with a radiation source using an Al Kα anode working at 250 W. The work pressure was $5x10^{-9}$ mbar. The obtained data were processed using the CasaXPS software. The spectra were referred to the C 1s signal at 284.6 eV, corresponding to the residual carbon. The decomposition into components was performed by fitting using a sum of Lorentz and Gauss functions with the Shirley subtraction of the background.

2.1.7. Isothermal adsorption of water

Measurements of water adsorption equilibrium are undertaken to characterize fundamental mechanisms of adsorption and transport of the water molecules in solid surfaces. The surface chemistry and the distribution of the primary adsorption sites play a fundamental role in the water adsorption mechanism. At very low relative pressures, the polar nature of the water molecule allows it to bond with individual oxygenated functional groups. In these conditions, the amount of adsorbed water is determined by the total number of primary adsorption sites. At higher relative pressures, the adsorbed water molecules interact by hydrogen bonding with the free water molecules, giving rise to the formation of clusters. At even higher relative pressures, water clusters grow up and hydrogen bonding between them occurs. Thus, the nature of the obtained equilibrium isotherm depends on the number of primary adsorption sites and also on their surface density [13].

Water adsorption isotherms of the studied samples were performed at 20 °C by thermogravimetric analysis using a SETARAM microbalance (TA Instruments). 20 mg of the sample were outgassed under secondary vacuum at room temperature for 24 hours prior to the sorption measurements. The sorbate pressure was then increased gradually in order to obtain the complete adsorption

isotherm. For each water uptake, the equilibrium was reached and the mass as a function of the time was recorded. These experiments were performed in the *Institut de Chimie des Milieux et des Matériaux de Poitiers,* University of Poitiers (France).

2.1.8. H_2 chemisorption

Hydrogen plays an important role in catalysis, being used not only as reducing agent and reactant, but also as probe molecule. Its selective chemisorption on noble metals allows its use as probe molecule in order to perform surface area measurements and catalysts characterization. Particularly, the number of surface metal atoms in a catalyst can be calculated as a function of the quantity of chemisorbed hydrogen.

Mechanisms of adsorption, surface reaction and desorption can be extremely complex, particularly over supported catalysts, where phenomena such as spillover, derived from the interaction between the active phase and the support, could interfere. There are certain systems where slow hydrogen spillover can become a problem for the quantitative determination of chemisorbed hydrogen. To avoid this problem, techniques as pulse flow methods, which limit the process kinetically, are preferred [14].

Hydrogen chemisorption analyses were performed in a pulse-flow apparatus. 200 mg of catalyst were placed in a U-shaped quartz reactor and reduced under H_2 flow at 350 °C for 1 hour, outgassed under Ar at the same temperature for 3 hours and finally cooled to 35 °C. At this temperature, two series of 6 H_2 pulses of 250 µl were dosed in the reactor. The H_2 not adsorbed during the pulses was quantified using a thermal conductivity detector (TCD). The dispersion values were calculated using the following equation:

$$\boldsymbol{D = N_s / N_T} \qquad \boldsymbol{Eq.2.4}$$

Where $\mathbf{N_s}$ is the total number of surface atoms and $\mathbf{N_T}$ the total number of metal atoms in the solid (bulk and surface).

2.1.9. Vibrational spectroscopy

Vibrations in molecules or in solid lattices are excited, among others, by the scattering of photons (Raman spectroscopy) or the absorption of photons (infrared spectroscopy). When the vibration is excited by the interaction of the bond with a wave field, this interaction is subject to certain selection rules.

2.1.9.1. Raman spectroscopy

Raman spectra are originated as a result of the electronic polarization caused by ultraviolet, visible and near-IR light. When a molecule is irradiated by a monochromatic light beam of frequency v, electronic polarization is induced in the molecule, giving rise to the scattering of the light of frequency v (Rayleigh scattering) and that of frequency $v \pm v_i$ (Raman scattering), where v_i corresponds to a vibrational frequency of the molecule. Thus, Raman spectra are presented as shifts from the incident frequency of the irradiated light [15].

Raman spectra of the synthesized samples were taken on a dispersive Horiba Jovin Yvon LabRam HR800 Confocal Raman Microscope with a green laser (λ = 532.14 nm: maximum power 20 mW) using a 600 groves/mm diffraction grating. Power was reduced to 5 mW with the use of optical density neutral filters. In these conditions, the laser spot diameter is 1.18 μm and the spatial resolution is 590 nm.

2.1.9.2. Infrared (IR) spectroscopy

The IR region provides information of rotation and vibration of molecules. When a molecule is subjected to IR radiation whose frequency is similar to that of one of its oscillators, the latter resonate and absorb part of the radiation. The absorption intensity depends on the probability of the transition between the ground and excited states. Only those transitions corresponding to vibrations with changes in the dipole moment are IR active, and the intensity of the obtained bands are proportional to the change in the dipole moment.

Additionally, *in situ* IR spectroscopy makes possible the observation of a catalyst and the adsorbed species on it at the reaction temperature in the presence of reactants, whereas *operando* IR spectroscopy allows to evaluate simultaneously the adsorbed species and the catalytic activity in reaction conditions.

a) In situ transmission IR spectroscopy

IR transmission spectra are obtained as a result of the direct transmission of an IR beam through a sample. The spectrometer records the transmission, which intensity can be calculated through the Lambert-Beer law (Eq. 2.5).

$$T = I/I_0 \qquad Eq.2.5$$

Where **T** is the transmittance, **I** is the intensity reaching the detector in the presence of the sample and $\mathbf{I_o}$ is the intensity measured by the detector in the absence of the sample.

Thus, the sensitivity of this method is determined by the characteristics of the radiation detector and by the absorption coefficient of the medium. By means of the Fourier transform (FT) technique the sensitivity is significantly improved. Typically, the sample is pressed into a thin self-supported wafer, decreasing the scattering that takes place during the transmission of the IR radiation through the sample [16].

The development of *in situ* experiments requires that the sample wafer is securely hold at a controlled temperature while the solid is exposed to reactant gases [17].

In situ IR measurements of the synthetized samples were performed in a home-made reactor-cell consisting on a stainless-steel cylinder which contains a toroidal sample holder in its center, where a sample wafer of 16 mm is placed. The cell is equipped with two CaF_2 terminal windows and two KBr windows which limit the dead volume to 0.12 cm^3 and the optical path below 3 mm. A heating system is incorporated in order to reach the desired temperature, as well as an air-cooling system to protect both ends of the cell. A scheme of the experimental setup is showed in Fig. 2.2. Spectra were collected by a Thermo Nicolet iS50 FT-IR spectrometer equipped with a liquid-nitrogen cooled mercury cadmium telluride (MCT) detector at a resolution of 4 cm^{-1} and an average of 64 scans.

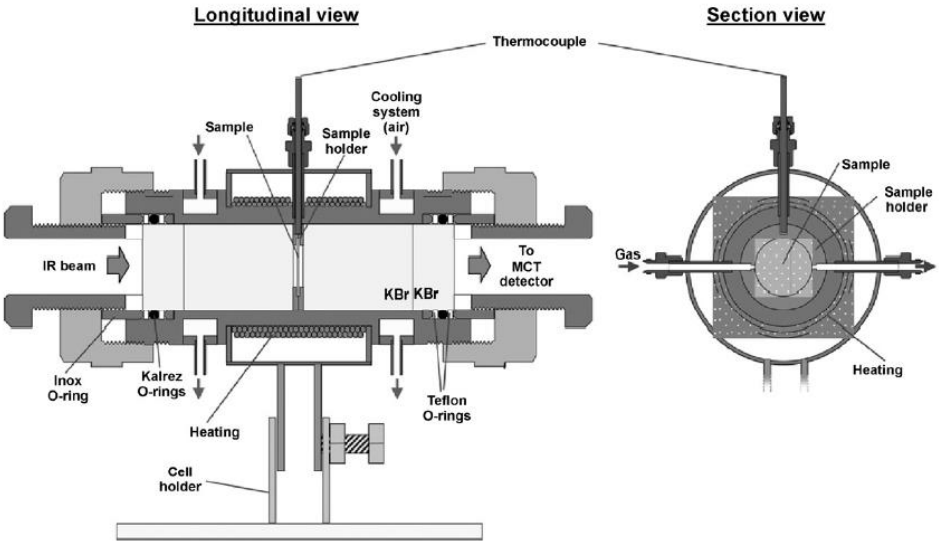

Figure 2.2. View of the transmission IR reactor cell. Reproduced from [18]

b) *In situ* and *Operando* Diffuse Reflectance Infrared Spectroscopy (DRIFTS)

Diffuse reflectance measures the radiation scattered by a powder sample, which is complementary to that measured in transmission. The scattering is the result of two processes: diffuse and specular reflectance. In this technique, the IR radiation passes into the sample and undergoes absorption, refraction and diffraction before re-emerging. Specular reflectance, which is a mirror-like reflection from the front surfaces of the analyzed sample, may distort the diffuse reflectance component of the spectrum. This problem can be minimized by a proper preparation of the sample [17, 19].

In situ and *operando* DRIFTS measurements were performed in a high-temperature reactor chamber supported on a Praying Mantis (Harricks) DRIFTS optical system using ZnSe windows. Spectra were collected by a Thermo Nicolet iS50 FT-IR spectrometer equipped with a liquid-nitrogen cooled MCT detector at a resolution of 4 cm^{-1} and an average of 64 scans. 40 mg of the finely ground solids were loaded in the catalytic cell and the reaction flow was introduced using a series of AALBORG mass-flow controllers and a KNAUER Smartline 1050 HPLC pump for the introduction of water in the system. In such case, the system was heated at 100 °C to avoid water condensation during the reaction.

For every FTIR experiment, the outlet gas composition was analyzed by mass spectrometry in a PFEIFFER mass spectrum Vacuum Prisma Plus controlled by the Quadera® software.

2.1.10. $^{18}O_2$ and $C^{18}O_2$ isotopic exchange experiments

Surface mobility of species have demonstrated to play a crucial role in heterogeneous catalysis. In this sense, isotopic exchange techniques provide effective answers to characterize the catalysts behavior concerning the mobility and reactivity of the atoms constituting a solid, as well as the elucidation of reaction mechanisms. Particularly, the isotopic exchange using $^{18}O_2/^{16}O_2$ and $C^{18}O_2/C^{16}O_2$ are useful to elucidate reaction mechanisms involving mobility steps of O-containing reactive species. The method is based on the measurement of the rates of exchange between gaseous $^{18}O_2$ (or $C^{18}O_2$) and ^{16}O species of the support via metal particles or small metallic clusters acting as porthole of O. This method can give useful information about reactions catalyzed by supported catalytic systems in which surface diffusion can play a decisive role in the mechanism. Differences between the oxygen exchange rate as a function of the labelled molecule employed are attributed to a difference in the exchange mechanism: for O_2 a dissociative mechanism takes place, in which the limiting step is the oxygen dissociation of the O_2 molecule, whereas for CO_2 an associative mechanism via formation and decomposition of intermediate species as formates, carbonyls or carbonates on the solid surface occurs [20].

For the X*/X ($X=O_2$, CO_2) isotopic exchange experiments of the evaluated samples, a quartz U reactor was placed in a closed recirculation system, connected to a mass spectrometer in order to follow continuously the evolution of the gaseous species as a function of the time, and to a vacuum pump. A recirculation pump eliminated the limitations due to the gas phase diffusion. A scheme of the isotopic exchange experimental setup is showed in Figure 2.3.

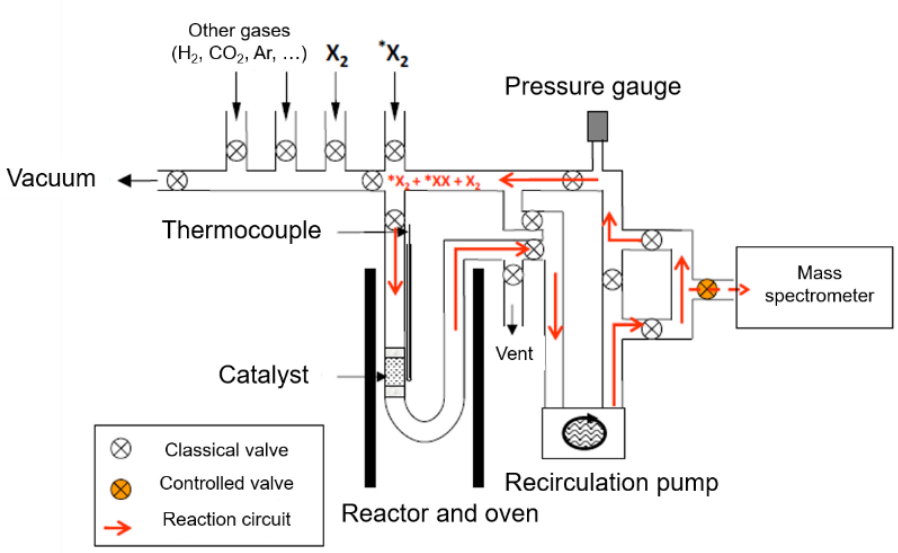

Figure 2.3. Scheme of the experimental setup employed for the X*/X isotopic exchange experiments

The studied supports were first activated under 50 ml min^{-1} of $^{16}O_2$ at the temperature of calcination and atmospheric pressure. Regarding the catalysts, the activation was carried out at 350 °C under 50 ml min^{-1} of H_2 in order to guarantee the reduction of the metallic species. After that, the temperature was decreased and the activation gas was evacuated to introduce the isotopic molecule in the reaction system. For the heteroexchange experiments, 65 mbar of $^{18}O_2$ or $C^{18}O_2$ were introduced in the system. Two different experiments were performed:

- **Temperature programmed isotopic exchange**, where the temperature was increased progressively along the experiment at a rate of 2 °C min^{-1}.
- **Isothermal isotopic exchange**, where the temperature was maintained constant along the experiment.

During the $^{18}O_2/^{16}O_2$ isotopic exchange experiments, the mass-to-charge ratio m/z 32 ($^{16}O_2$), 34 ($^{16}O^{18}O$) and 36 ($^{18}O_2$) were recorded, whereas for the $C^{18}O_2/C^{16}O_2$ the mass-to-charge ratio m/z 44 ($C^{18}O_2$), 46 ($C^{16}O^{18}O$) and 48 ($C^{18}O_2$) were evaluated, with the purpose of following the isotopomer distribution formed during the reaction. The absence of air and CO_2 at the beginning of the experiments were verified by mass spectrometry in both cases.

The atomic fractions of X*X in the gas phase (α_g), the rate of exchange (R_e) and the number of O exchanged atoms (N_e) were calculated according to the following equations.

$$\alpha_g = \frac{1/2\, P_{X^*X} + P_{X_2^*}}{P_{X_2^*} + P_{X^*X} + P_{X_2}} \qquad \boldsymbol{Eq.2.6}$$

Where **P** corresponds to the partial pressure of the gaseous species.

$$R_e = -N_g \frac{d\alpha_g}{dt} \qquad \boldsymbol{Eq.2.7}$$

Where $\mathbf{N_g}$ is the number of *X atoms in the gas phase at the beginning of the reaction.

$$N_e = N_g(1 - \alpha_g) \qquad \boldsymbol{Eq.2.8}$$

For the experiences using $C^{18}O_2$, the oxygen diffusion coefficient in the bulk was calculated according to the mathematic model developed by Kakioka et al. [21, 22] . For this calculation, the authors propose the equation 2.9 derived from the classic diffusion equations (Fick's Law).

$$-Log(\propto_g^t - 0.2) = \frac{\rho \cdot S}{N_g}\sqrt{\frac{4D}{\pi}}\sqrt{t} - \log(\alpha_g' - 0.2) \qquad \boldsymbol{Eq.2.9}$$

Where $\boldsymbol{\alpha_g^t}$ is the ^{18}O concentration (%) in the CO_2 gas at time = t; $\boldsymbol{\alpha_g'}$ is the ^{18}O concentration (%) in the CO_2 gas when the fast exchange with the oxygen surface atoms is reached; **0.2** is the intrinsic quantity (%) of ^{18}O in the solid at t = 0; **ρ** is the density of oxygen in the solid ($at \cdot m^{-3}$); **S** is the surface of the sample (m^2); $\mathbf{N_g}$ is the number of oxygen atoms in the gas phase and **D** is the oxygen diffusion coefficient in the bulk ($m^2 \cdot min^{-1}$).

Thus, by plotting $Log(\alpha_g^t - 0.2)$ as a function of $t^{1/2}$, the diffusion coefficient D can be calculated from the slope of the linear part of the curve. It should be noted that this equation supposes that the exchange between $C^{18}O_2$ and the totality of the surface is achieved very fast. Actually, some minutes are necessary to reach the equilibrium, thus not being possible the application of this equation during these minutes.

2.2. Catalytic activity measurements

For the catalytic evaluation of the prepared catalysts on the WGS reaction, the employed gases and their respective purity were: CO (Linde, ≥ 99.5), H_2O milli Q, CO_2 (Linde, > 99.9%), H_2 (Linde, ≥ 99.9%) and N_2 (Linde, ≥ 99.999%).

2.2.1. Experimental setup for the WGS reaction

Figure 2.4 shows a scheme of the reaction system used for the evaluation of the catalytic performance on the WGS reaction.

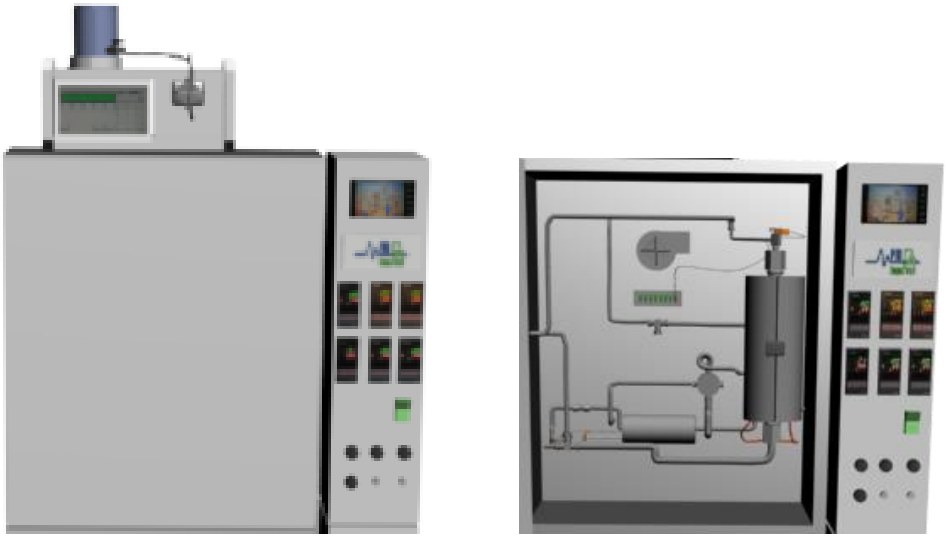

Figure 2.4. Scheme of the reaction system for the evaluation of the catalysts in the WGS reaction

The experiments were carried out in a Microactivity-Reference (PID Eng&Tech) equipment, using a tubular Hastelloy reactor with an inner diameter of 17 mm operating at atmospheric pressure and temperatures between 150 and 350 °C. 200 mg of the catalyst (particle size, 600-800 µm) were diluted with SiC (~ 686 µm) to obtain a catalytic bed volume of 6 cm^3. The catalysts were first activated at 350 °C for 1 hour under a 10% H_2/N_2 flow at a rate of 100 ml min^{-1}. The reactor was the cooled down to 150 °C and the catalysts were submitted to 100 ml min^{-1} of the reaction mixture. Two feed-streams (A and B) have been used: feed-stream A (4.5% CO, 30% H_2O, 65.5% N_2) and feed-stream B, a mixture simulating the feed conditions of a WGS unit coming from a reformer (7% CO, 9% CO_2, 50% H_2, 30% H_2O, 4% N_2).

Reaction products were analyzed by an on-line chromatography data system (VARIAN CP-4900 µGC) equipped with a ®Porapak Q column, a Mole-Sieve 5A, and two TCD detectors. The CO_2 concentration at the reactor exit was monitored using a VAISALA GMT220 series detector. CO conversion at each reaction temperature was calculated according to Equation 2.10.

$$X_{CO}(\%) = \frac{F_{CO\ in} - F_{CO\ out}}{F_{CO\ in}} x100 \qquad \boldsymbol{Eq.2.10}$$

Where $\mathbf{F_{CO\ in}}$ and $\mathbf{F_{CO\ out}}$ are the inlet and outlet volume of CO in the reactor respectively.

Weight hourly space velocity (WHSV) at which the experiments were carried out was calculated according to Equation 2.11.

$$WHSV\ (L \cdot g^{-1} \cdot h^{-1}) = \frac{Feed\ flow\ (L \cdot h^{-1})}{Catalyst\ mass\ (g)} \qquad \boldsymbol{Eq.2.11}$$

2.3. References

1. West, A.R., *Crystallography and Diffraction Techniques*, in *Solid State Chemistry and its Applications*, A.R. West, Editor. 2014, Wiley. p. 230-270.

2. Patterson, A.L., *The Scherrer Formula for X-Ray Particle Size Determination.* Physical Review, 1939. **56**(10): p. 978-982.

3. *The Rietveld Method*, ed. R.A. Young. 1995: Oxford University Press.

4. Rodríguez-Carvajal, J., *Recent advances in magnetic structure determination by neutron powder diffraction.* Physica B: Physics of Condensed Matter, 1993. **192**: p. 55-69.

5. Boss, C.B. and K.J. Fredeen, *Concepts, Instrumentation and Techniques in Inductively Coupled Plasma Optical Emission Spectrometry*. 2004: Perkin Elmer.

6. Vyazovkin, S., *Thermogravimetric Analysis*, in *Characterization of Materials*, E.N. Kaufmann, Editor. 2012, Wiley. p. 1-12.

7. Schick, C., D. Lexa, and L. Leibowitz, *Differential Scanning Calorimetry and Differential Thermal Analysis*, in *Characterization of Materials*, E.N. Kaufmann, Editor. 2012, Wiley. p. 483-495.

8. Neimark, A.V., K.S.W. Sing, and M. Thommes, *Surface Area and Porosity*, in *Handbook of Heterogeneous Catalysis*, G. Ertl, et al., Editors. 2008, Wiley. p. 721-737.

9. Sing, K.S.W., *Physisorption of Nitrogen by Porous Materials.* Journal of Porous Materials, 1995. **2**: p. 5-8.

10. Zhou, W., et al., *Fundamentals of Scanning Electron Microscopy (SEM)*, in *Scanning Microscopy for Nanotechnology*, W. Zhou and Z. Lin Wang, Editors. 2006, Springer.

11. Datye, A.K., P.L. Hansen, and S. Helveg, *Electron Microscopy Techniques*, in *Handbook of Heterogeneous Catalysis*, G. Ertl, et al., Editors., Wiley-VCH. p. 803-833.

12. Niemantsverdriet, J.W., *Photoemission and Auger Spectroscopy*, in *Spectroscopy in Catalysis: An Introduction*. 2007, Wiley-VCH. p. 39-84.

13. Rutherford, S.W. and J.E. Coons, *Equilibrium and Kinetics of Water Adsorption in Carbon Molecular Sieve: Theory and Experiment.* Langmuir, 2004. **20**: p. 8681-8687.

14. Ferreira-Aparicio, P., A. Guerrero-Ruiz, and I. Rodriguez-Ramos, *Hydrogen adsorbed species at the metal/support interface on a Pt/Al2O3 catalyst.* Journal of the Chemical Society, Faraday Transactions, 1997. **93**: p. 3563-3567.

15. Nakamoto, K., *Theory of Normal Vibrations*, in *Infrared and Raman Spectra of Inorganic and Coordination Compounds*. 2009, Wiley. p. 1-136.

16. Davydov, A., *Theoretical fundamentals and experimental considerations of the spectroscopic methods used in surface chemistry*, in *Molecular Spectroscopy of Oxide Catalyst Surfaces*, N.T. Sheppard, Editor. 2003, Wiley. p. 1-25.

17. Howe, R.F., *In Situ Infrared Methods*, in *In-Situ Spectroscopy in Heterogeneous Catalysis*, J.F. Haw, Editor. 2002, Wiley-VCH. p. 139-178.

18. Lesage, T., et al., *Studying the NO_x-trap mechanism over a Pt-Rh/Ba/Al_2O_3 catalyst by operando FT-IR spectroscopy.* Physical Chemistry Chemical Physics, 2003. **5**(20): p. 4435-4440.

19. Raymond, K.W. and J.A. Corkill, *Diffuse Reflectance Infrared Spectroscopy.* Journal of Chemical Education, 1994. **A204**.

20. Duprez, D., *Oxygen and Hydrogen Surface Mobility in Supported Metal Catalysts. Study by $^{18}O/^{16}O$ and $^{2}H/^{1}H$ Exchange*, in *Isotopes in Heterogeneous Catalysis*, J.S.J. Hargreaves, S.D. Jackson, and G. Webb, Editors. 2006, Imperial College Press. p. 133-182.

21. Kakioka, H., V. Ducarme, and S.J. Teichner, *I. Échange isotopique de 18O du gaz carbonique avec les ions oxygène de l'hémipentoxyde de vanadium.* Journal de Chimie Physique, 1971. **68**: p. 1715-1721.

22. Kakioka, H., V. Ducarme, and S.J. Teichner, *II. Échange isotopique de 18O du gaz carbonique avec les ion oxygène de l'hémipentoxyde de vanadium dopé par l'ion molybdène Mo6+.* Journal de Chimie Physique, 1971. **68**: p. 1722-1725.

Chapter III

Synthesis and characterization of $CePO_4$-based catalysts

Abstract

The present chapter describes the synthesis and physicochemical characterization of the two possible crystal structures of $CePO_4$: the hexagonal (rhabdophane-type), and the monoclinic (monazite-type) phases. Their textural, structural, morphological and chemical features are analyzed in order to determine the differences between both phases and their possible influence regarding the interaction with the water molecule, which plays a fundamental role during the Water-Gas Shift (WGS) reaction. Afterwards, the synthesis and characterization results of the corresponding supported Pt catalysts are analyzed. For the sake of comparison with the Pt system, the synthesis of Au and Cu-based catalysts supported on $CePO_4$ is also described, together with a brief description of their structural characteristics.

3.1. Introduction

The use of supported metal catalysts for the WGS reaction have motivated a deep study of these materials over the years, regarding both the metal phase and the support. A general conclusion derived from the numerous studies accomplished is the synergy existing between the active phase and the support [1, 2].

Regarding the active phase, several studies have emphasized the suitability of using noble metals for the WGS reaction in fuel cell applications [3-6] compared to the traditional low-temperature Cu-based catalysts [6, 7]. The latter present a series of drawbacks, as their pyrophoricity and the sintering and loss of Cu surface area in reducing atmospheres [8]. Furthermore, Cu catalysts need to be used in pellets to provide enough mass to avoid poisoning and increase the shelf life of these systems, which results in very low space velocities and makes necessary big reactor volumes, a non-desirable aspect for compact applications. In order to overcome this problems, noble metal catalysts have been employed due to their advantages such as high activity, fast response, long catalyst lifetime and non-pyrophoricity [5, 7-11]. Among them, Pt is particularly interesting due to its superior performance compared to other noble metals [5, 12].

On the other hand, the support is known to be involved in the activation of the water molecule, generally recognized as the rate-limiting step of the WGS reaction. Thus, both reducible and non-reducible supports have been extensively studied for the WGS reaction [13-16]. Among them, oxide supports containing oxygen vacancies have been highlighted, since they play a fundamental role with regard to the dissociation of the water molecule, which determines the WGS catalytic performance. In this context, supports such as TiO_2 or CeO_2 have been proposed as interest candidates since they greatly enhance the water activation rate through the influence of their electronic properties when they are partially reduced [17-19]. Particularly in the case of CeO_2, such properties rely on the presence of the Ce^{3+}/Ce^{4+} redox pair, which is directly related to the presence of oxygen vacancies in the solid [20, 21]. However, CeO_2 is known to be deactivated in cyclic operation conditions, that is due to shut-down and start-up processes [22, 23]. To overcome the deactivation problem and improve the electronic and structural properties of CeO_2, several studies have been performed [12, 24, 25]. Particularly, the addition of protonic conductors to CeO_2-based catalysts have demonstrated to enhance the WGS catalytic

performance through a proton conduction mechanism, promoting the water dissociation step [26] through the so-called “Grotthuss mechanism”, which implies hopping of a lone proton between oxide ions [27, 28]. According to the aforementioned considerations, the study of $CePO_4$ as support for the WGS reaction results interesting due to several reasons: first, the presence of cerium in its structure, which could influence the electronic properties of the material through the presence of the Ce^{3+}/Ce^{4+} redox pair, accompanied by the previous use of phosphate-type compounds as electrolytes for the production of electricity in hydrogen fuel cells [29-31], which points out the inherent conduction properties of these materials. Additionally, $CePO_4$ has shown an unusual water uptake capacity [32, 33], which could influence the proton transport mechanism, as well as the availability of water during the WGS reaction, thus influencing the WGS catalytic performance [34, 35].

This rare-earth phosphate could present two different structures depending on its hydration degree: the hexagonal rhabdophane-type $CePO_4 \cdot nH_2O$ ($0.5 < n < 1$) and the monoclinic monazite-type $CePO_4$ [32, 36, 37], shown in Figure 3.1.

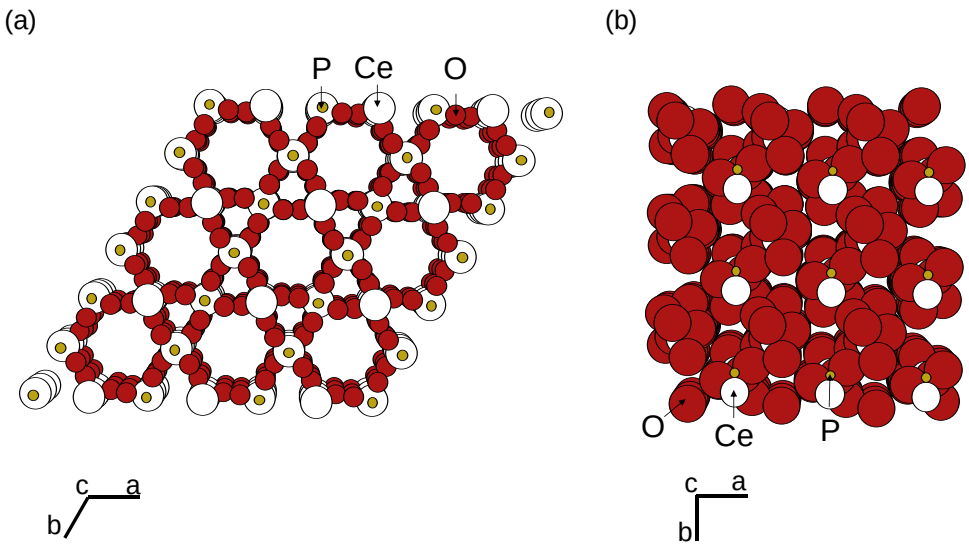

Figure 3.1. View along the *c* axis of (a) rhabdophane and (b) monazite-type phases

In both structures, cerium is coordinated to eight oxygen atoms, four located at 2.33 Å and four at 2.66 Å. In the hexagonal phase, these oxygen structural atoms form a series of open channels along the hexagonal axis, in which water molecules are located [33, 38, 39]. This structure is easily transformed into the anhydrous monoclinic one at moderately high temperatures [32, 39-

42]. Although Ce-O distances are similar in both structures, the monazite-type phase possesses a more packed structure in which the previously unoccupied spaces are substituted by atoms, consistently with its higher density value (5.26 $g \cdot cm^{-3}$) compared with its hexagonal homologue (4.22 $g \cdot cm^{-3}$). The structural differences between both crystallographic phases could give rise to morphological and/or textural changes influencing the catalytic performance of these materials on the WGS reaction.

Considering the aspects mentioned above, this chapter presents the synthesis and characterization results of the rhabdophane- and monazite-type phases of $CePO_4$ and the subsequent 2 wt.% Pt catalysts. For the sake of comparison, the synthesis and basic characterization results of two more catalysts containing Au and Cu as active phase are also presented.

3.2. Supports synthesis

Phosphoric acid 85% (Panreac), cerium (III) nitrate hexahydrate (Fluka), ammonia 30% (Panreac) and sodium citrate dihydrate (Sigma) were used as raw materials for the synthesis of the supports.

The syntheses of $CePO_4$ were carried out adapting a hydrothermal method previously described [43]. 50 ml of equimolar aqueous solutions (0.6 M) of phosphoric acid and cerium (III) nitrate hexahydrate were mixed and maintained at 40 °C under stirring. Then, 50 ml of a 0.019 M aqueous solution of sodium citrate dihydrate was added, and the pH was raised to 10 by the addition of ammonia 30%. The resultant solution was kept at 40 °C for 8 hours under stirring and then transferred to a Teflon-lined autoclave where it was aged at 100 °C for 8 hours. The obtained solid was filtered, thoroughly washed with distilled water and dried overnight at 100 °C. The obtained material, named CeP, was divided in two fractions and calcined at 400 and 600 °C, labelled as supports CeP400 and CeP600, respectively.

3.3. Physicochemical characterization of the supports

3.3.1. X-ray diffraction (XRD) analyses

In order to assess the calcination temperature required for obtaining the rhabdophane and monazite-type phases of $CePO_4$, in situ high-temperature XRD experiments were performed. Figure 3.2 presents the XRD pattern of the fresh support from RT to 650 °C in air.

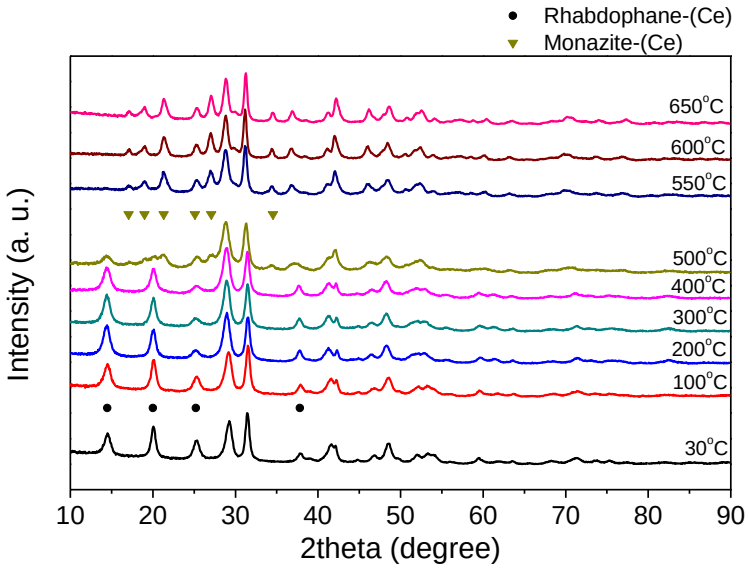

Figure 3.2. XRD patterns of the fresh support (CeP) during the temperature treatment

The diffraction pattern of the fresh solid corresponds to the rhabdophane-type phase of $CePO_4$ (JCPDS-ICDD 01-075-1880) which presents hexagonal structure and crystallizes in the space group $P6_222$. This crystal phase is preserved until 500 °C, temperature at which the diffraction lines of the monazite-type phase (JCPDS-ICDD 00-032-0199) appear. This phase of the $CePO_4$ presents monoclinic structure and space group $P2_1/n$. At 600 °C, the absence of diffraction peaks corresponding to the rhabdophane-type phase indicates the complete formation of the monoclinic phase. This thermostructural evolution from rhabdophane to the monazite-type phase has been previously reported [35, 44] and it has been found to be an irreversible transformation due to the compaction of the atom arrangement [41].

Thus, the calcination temperatures selected for the fresh solid CeP were 400 and 600 °C, with the purpose of obtaining the rhabdophane (CeP400) and monazite-type (CeP600) phases, respectively. The observed and calculated XRD patterns of the calcined supports after Rietveld refinement are shown in Figure 3.3. These results confirm that after calcination at 400 °C, the

$CePO_4$ exists as the rhabdophane-type phase, whereas the calcination treatment at 600 °C induces the phase transition to the monazite-type phase. For this solid, the fitting between the observed and calculated data was also performed considering the possible presence of the rhabdophane-type phase, being the adjust unsatisfactory and consequently, confirming the complete disappearance of the rhabdophane-type phase after calcination at 600 °C. The crystallite size of CeP400 was calculated using the X-ray line broadening of the (102) plane, being 20 nm, whereas the crystallite size of CeP600 calculated from the (012) diffraction line was 24.6 nm, exposing the structural change derived from the total dehydration of the support. Cell parameters and cell volume of both supports were calculated from the refinement results. As shown in Table 3.1, the obtained values are greatly close to the theoretical values displayed on the selected JCPDS patterns.

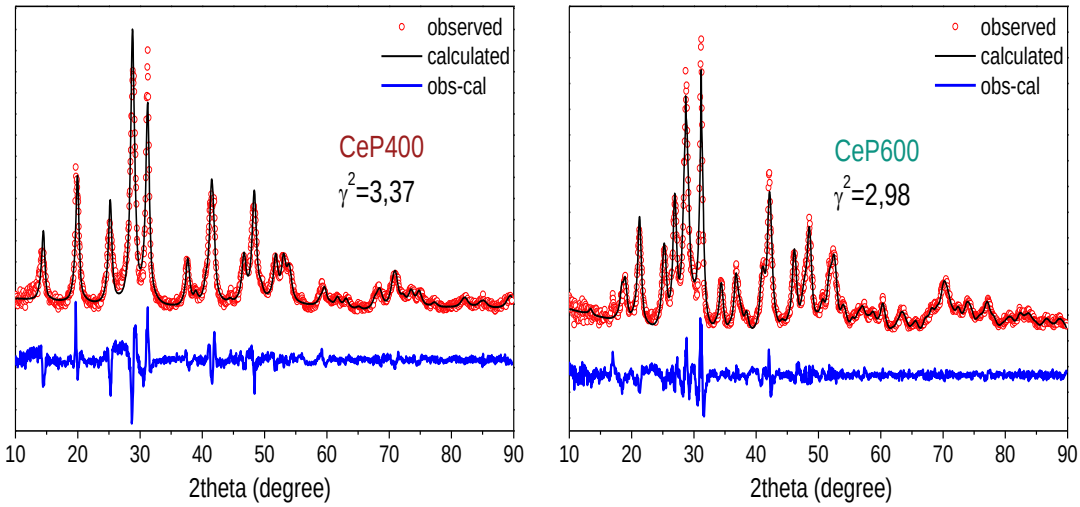

Figure 3.3. Observed and calculated XRD patterns of CeP400 and CeP600 considering hexagonal and monoclinic solutions respectively

Table 3.1. Calculated and theoretical cell parameters of the rhabdophane-type (CeP400) and monazite-type (CeP600) supports

Sample/JCPDS	a (Å)	b (Å)	c (Å)	V (Å³)
CeP400	7.0647	7.0647	6.4833	280.23
01-075-1880	7.055	7.055	6.4390	277.55
CeP600	6.8185	7.0315	6.4693	301.63
00-032-0199	6.8004	7.0231	6.4717	300.60

3.3.2. Thermogravimetric Analysis (TGA) and Differential Thermal Analysis (DTA)

Figure 3.4 shows the DTA plots of the fresh solid CeP. A 6 wt.% loss takes place below 200 °C, associated with the desorption of physisorbed water. A second process associated with a 4 wt.% loss occurs from 200 to 300 °C, attributed to the dehydration of the rhabdophane-type phase [35]. The observed weight loss allows the determination of the water stoichiometry of the fresh rhabdophane-type support, which is found to be $CePO_4 \cdot 0.53H_2O$, within the typical values described in the literature ($0.5 < n < 1$). A thermal process is observed at around 650 °C whereas no significant weight loss is detected. This fact seems related to the phase transformation of the hydrated rhabdophane-type phase of $CePO_4$ into the completely dehydrated monazite-type phase, due to the loss of the water molecules bound in the structural channels of the hydrated form [33, 38, 45], and coincides with the results obtained by XRD.

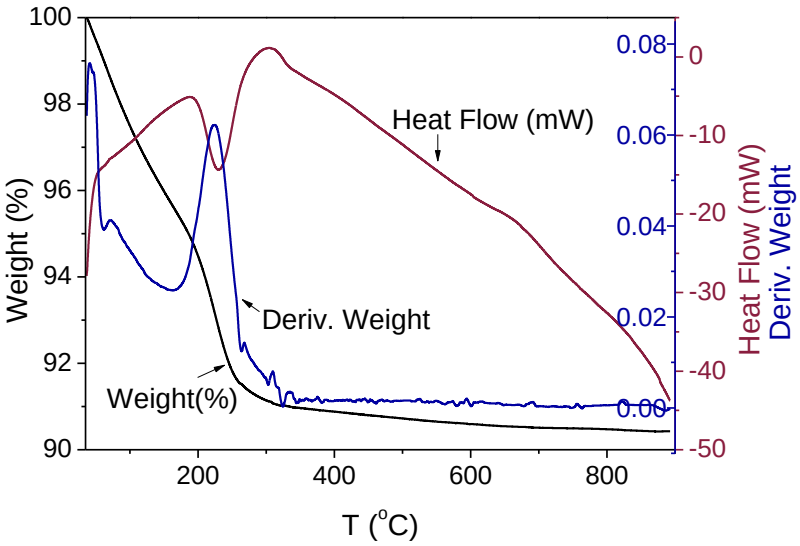

Figure 3.4. DTA curves of the as-prepared CeP support

3.3.3. Chemical composition and textural properties

Table 3.2 shows the chemical composition of the prepared supports obtained by ICP. Both supports present a composition close to the nominal one, pointing out the suitability of the hydrothermal method employed during the synthesis for the accurate control of the composition.

Table 3.2. Chemical composition of the supports after calcination at 400 and 600 °C

Sample	Ce (wt. %)	P (wt. %)
CeP400	59.2	13.1
CeP600	59.4	13.5

Figure 3.5 presents the N_2 adsorption/desorption isotherms of the prepared supports. Both solids present a weak N_2 adsorption at low relative pressure, indicating the presence of microporosity in both materials. A pronounced volume adsorption at $P/P_0 \approx 0.8$ indicates that multilayer adsorption starts at high relative pressure in these solids, thus indicating a considerable amount of mesopores in their structure. Both isotherms reveal pore condensation accompanied by hysteresis at high relative pressure, which could include interparticle voids. The hysteresis loop is H1-type according to the IUPAC classification [46], typical of solids containing uniform channels, as in the support CeP400 or constituted by aggregates of particles, as in CeP600.

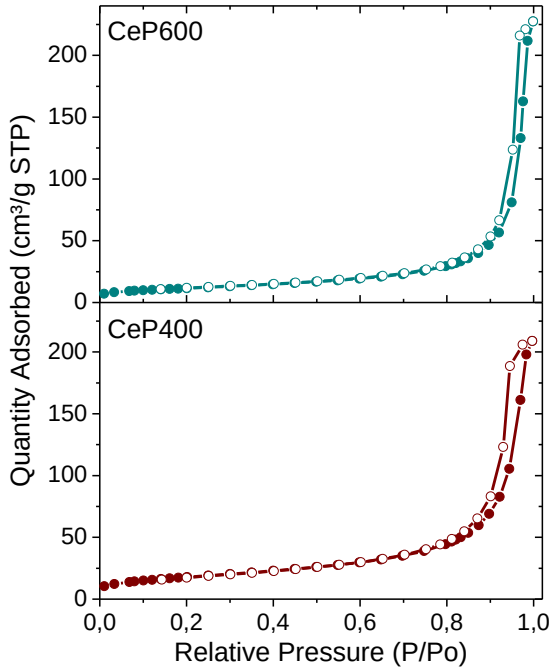

Figure 3.5. Nitrogen adsorption/desorption isotherms of the prepared supports (adsorption: full circles, desorption: empty circles)

Textural properties of the support are summarized in Table 3.3. After calcination at 400 °C, the BET surface area is 65 $m^2 \cdot g^{-1}$, while calcination at 600 °C produces a decrease of the surface area up to 41 $m^2 \cdot g^{-1}$. Concerning the porosity, both supports present a multimodal distribution of

mesopores, according to the BJH pore size distribution derived from the isotherms (Figure 3.6). The solid CeP400 presents a broadened distribution of mesopores compared to CeP600, and a maximum at approximately 110 Å, not observed in CeP600. This fact denotes the greater concentration of mesopores in the rhabdophane-type phase of $CePO_4$, which concurs with the presence of structural uniform channels in the solid CeP400 and the vanishing of them in the solid CeP600. A great concentration of macropores is also observed, being attributed to the interparticle voids.

Table 3.3. Textural properties of the supports

Sample	S_{BET} ($m^2 \cdot g^{-1}$)	V_p ($cm^3 \cdot g^{-1}$)	D_p (Å)
CeP400	65	0.32	172
CeP600	41	0.35	282

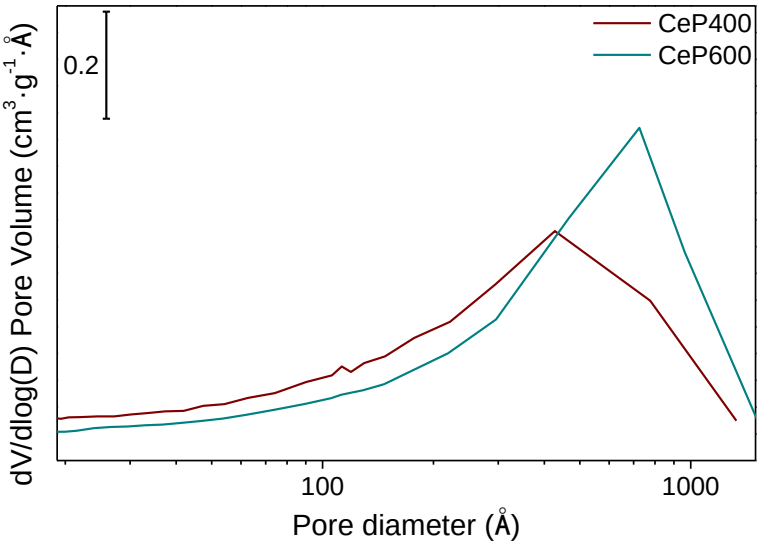

Figure 3.6. BJH pore size distribution of the supports

3.3.4. Scanning and Transmission Electron Microscopy (SEM and TEM)

Representative SEM micrographs of the supports are shown in Figure 3.7. Both samples consist of needle-like shape agglomerates, according to the structural characteristics previously reported for the rhabdophane and monazite-type phases [40, 47].

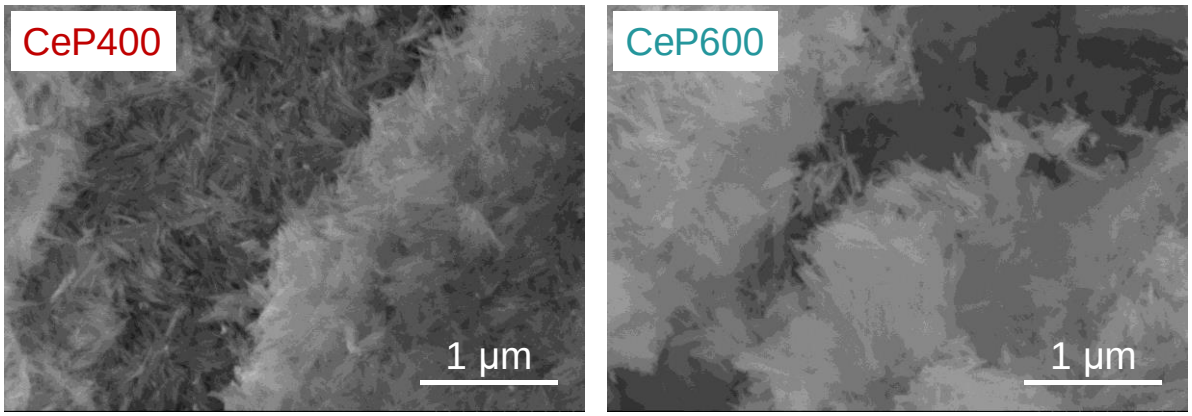

Figure 3. 7. SEM micrographs of the supports after calcination at 400 °C and 600 °C

The morphology and structure of the supports were further characterized by TEM, and the obtained micrographs are displayed in Figure 3.8. The aggregates of CeP400 are bar-shaped and present parallel channels along the (100) plane, that is parallel to the *c* axis, and being their diameter 0.62 ± 0.1 nm, in good agreement with the reported structural characteristics of the rhabdophane-type phase [38, 48]. Although $CePO_4$ particles in CeP600 are bar-shaped similar to CeP400, channels are not present in its structure. Calcination at 600 °C causes the elimination of the stabilization water located inside the structural channels and consequently, gives rise to the disappearance of the latter.

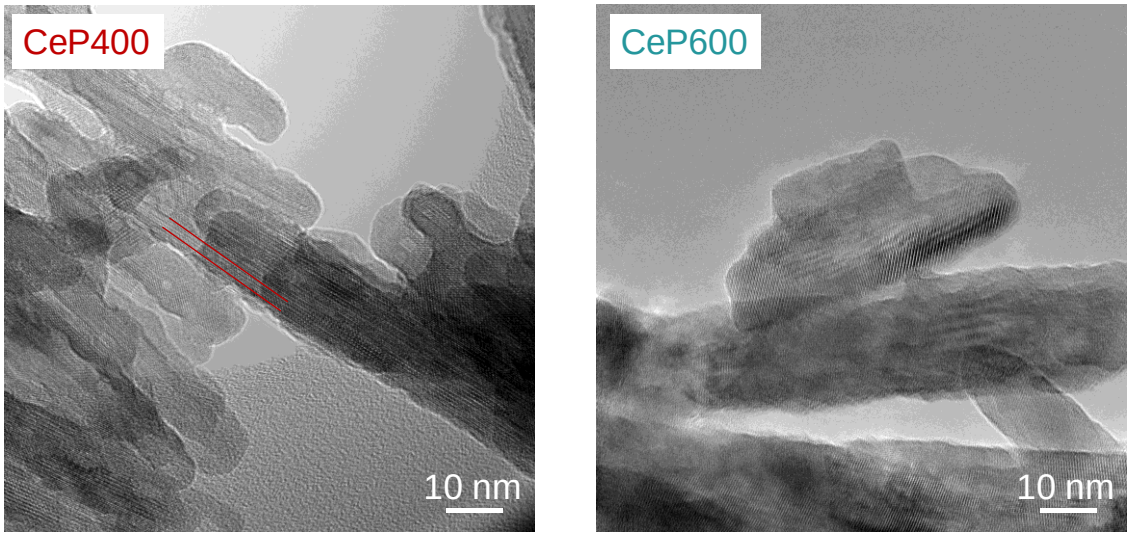

Figure 3.8. TEM micrographs of the supports after calcination at 400 and 600 °C

3.3.5. X-ray Photoelectron Spectroscopy (XPS)

Ce 3d, P 2p and O 1s regions of the XPS spectra of the supports before and after a reduction treatment are presented in Figure 3.9.

Ce 3d region (Fig. 3.9 (a)) could present 10 peaks associated with different Ce oxidation states (Ce^{3+} and Ce^{4+}) and their 4f configurations [49]. The XPS spectra of both supports show two peaks, corresponding to the spin-orbit split $3d_{3/2}$ (u': 903.0 eV) and $3d_{5/2}$ (v': 884.5 eV) levels and their corresponding satellites appearing at lower energy than the principal lines (u_0: 899.1 eV, v_0: 880.7 eV). The existence of these satellites has been reported previously by several authors [50, 51] in cerium compounds and has been attributed mainly to the existence of different final states. The spacing between the main peaks and their satellites is 3.8 eV, similar to the values reported by other authors [49, 52]. A peak at about 915 eV, assigned to the Ce^{4+} ion is not observed in any case, indicating that the redox pair Ce^{3+}/Ce^{4+} typically described in CeO_2 or CeO_2-ZrO_2 [53] is present neither in CeP400 nor in CeP600. This fact could have mechanistic implications on the WGS reaction, where the role of oxygen vacancies associated with the Ce redox pair has been highlighted [11, 20, 54].

P 2p region (Fig. 3.9 (b)) shows only one contribution centered at ca. 133 eV in both supports, which indicates that all the phosphorus atoms are in an equivalent environment. The shifts of the $2p_{1/2}$ (CeP400: 133.8, CeP600: 133.9 eV) and $2p_{3/2}$ (CeP400: 133, CeP600: 132.9 eV) core levels of both samples are too small (0.1 eV) to be associated to structural differences between CeP400 and CeP600.

O 1s region presents a peak centered at 530.2 and 530.4 eV for CeP400 and CeP600 respectively. Thus, the shift of this peak between both samples is negligible as in the case of the P 2p region. Nevertheless, due to the presence of water in the CeP400 structure, an O 1s peak at higher binding energy (533 eV) could be expected [55]. Since this contribution is not present in the CeP400 spectra, it is possible to confirm that the structural water contained in the rhabdophane-type phase is not located on the surface, which is in agreement with the presence of them inside the structural channels of the support.

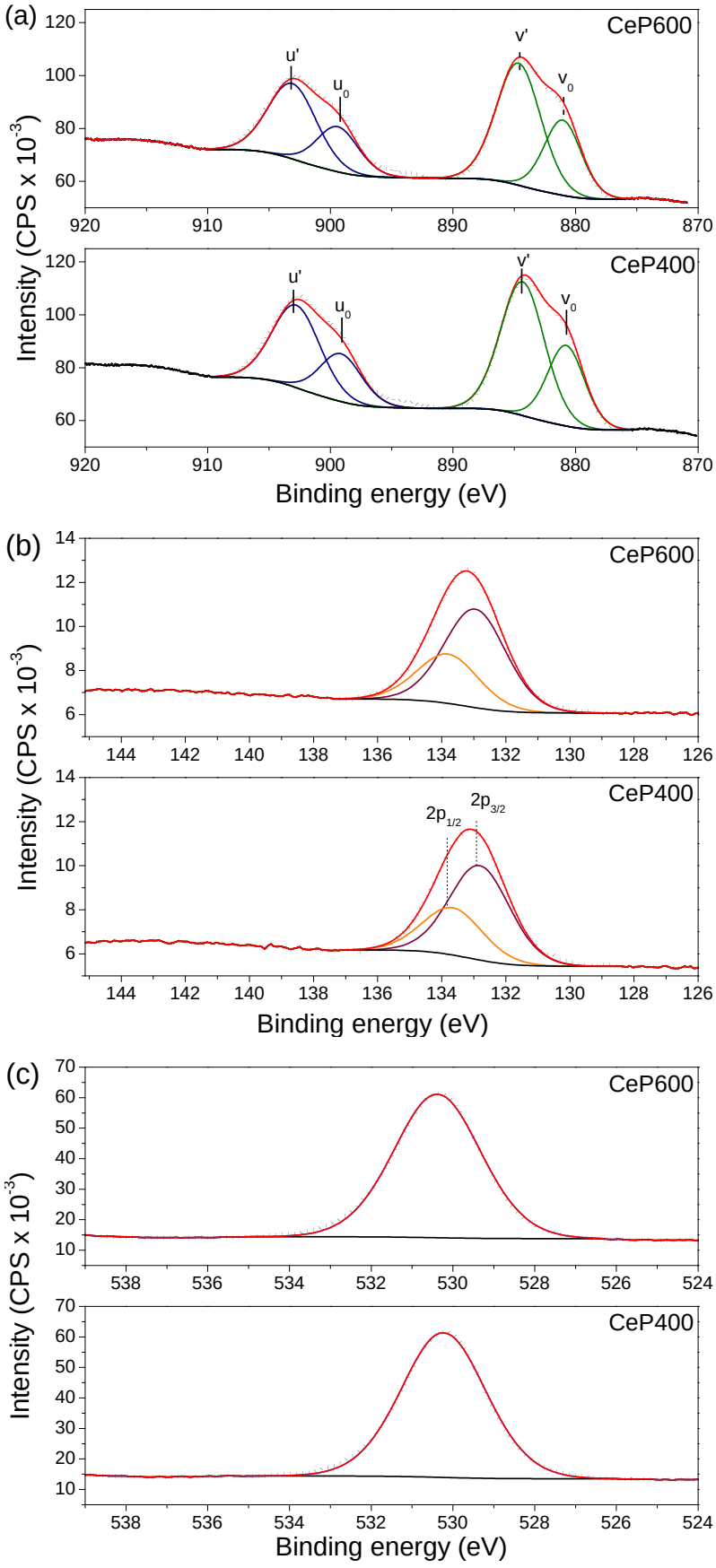

Figure 3.9. XPS spectra of the prepared supports, (a) Ce 3d, (b) P 2p and (c) O 1s regions

3.3.6. Raman spectroscopy

Raman spectra of the fresh and calcined supports are shown in Figure 3.10 (a). P-O stretching modes appear in the 1114-963 cm^{-1} range. The most intense Raman band at 980 cm^{-1} corresponds to the symmetric A mode. It is clearly observed the splitting of the symmetric band in two vibrations at 974 and 997 cm^{-1} after calcination at 600 °C (Fig. 3.10 (b)), while the band corresponding to the asymmetric mode is shifted from 1089 cm^{-1} in CeP and CeP400, to 1062 cm^{-1} in CeP600, indicating the changes in the geometry of the phosphate groups owing to the rhabdophane-type structure dehydration [35]. PO_4^{3-} bending modes are found between 642-400 cm^{-1}, being those over 500 cm^{-1} (623, 572 and 537 cm^{-1}) the asymmetric modes. These results fit with those reported in the literature [35, 36]. A band at 3470 cm^{-1}, attributed to structural O-H groups is present in CeP and remains after calcination at 400 °C, although a decrease in intensity takes place. After calcination at 600 °C this band completely disappears. Therefore, the band at 3470 cm^{-1} in CeP and CeP400 could be attributed to the presence of structural water in the rhabdophane-type phase, whereas calcination at 600 °C would provoke the complete dehydration of the structure, thus giving rise to the formation of the monazite-type phase. These results are consistent with those obtained by XRD.

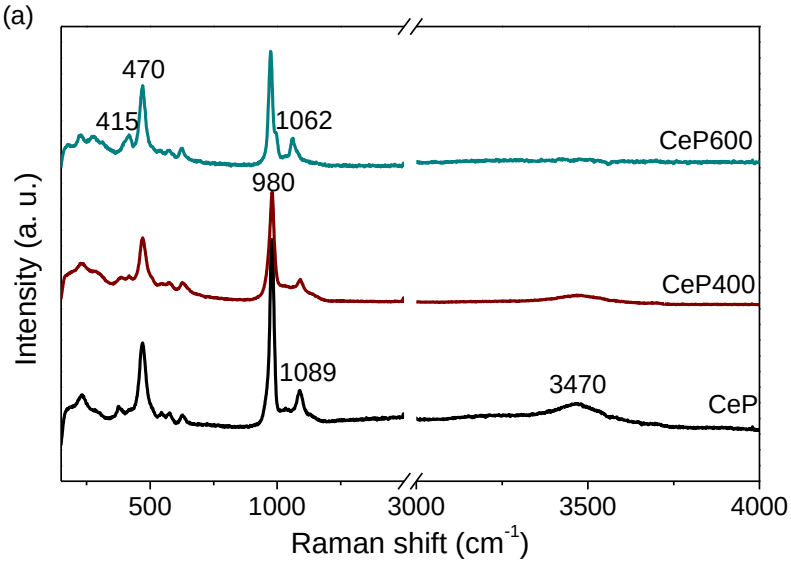

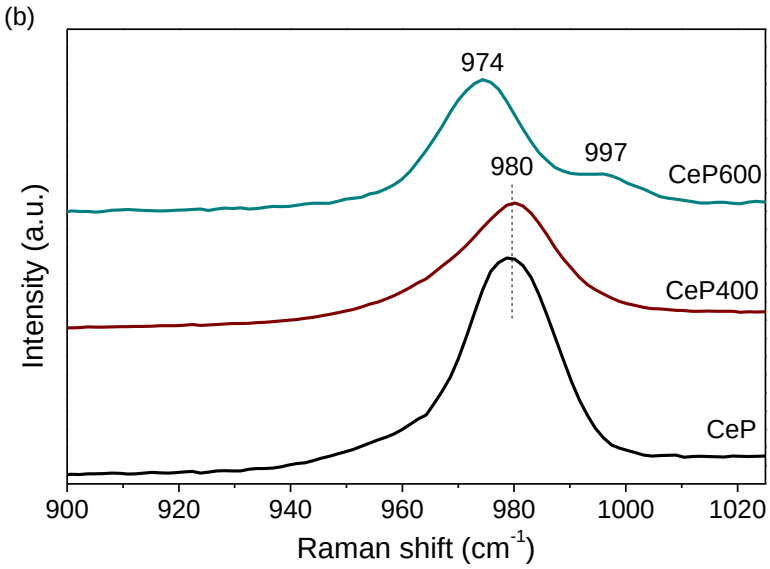

Figure 3.10. Raman spectra of (a) fresh and calcined supports, (b) enlargement of the P-O stretching region

3.3.7. Isothermal adsorption of water

Since water availability is a crucial factor for the successful catalytic performance on the WGS reaction, the study of the water retention capacity of the supports results of great interest. In addition, this technique provides additional information to that obtained by N_2 physisorption concerning the porosity of the materials [56]. Figure 3.11 presents the water adsorption isotherms of the supports at 20 °C. Two steps are observed in both supports, one at low relative pressure, related with the filling of the micropores, and a second one attributed to the filling of the mesopores. It can be concluded that both the volume of micro- and mesopores is greater in the support CeP400. The steep uptake observed at low relative pressure is the consequence of an enhanced adsorbent-adsorbate interaction in ultramicropores, which is particularly pronounced in the solid CeP400. Additionally, the adsorption capacity of CeP400 is 1.6 times superior to that of CeP600, what is in accordance with the presence of channels able to hold water molecules in its structure. Although these cavities are not present in the support CeP600, its capacity to adsorb water has been explained by other authors through the formation of a continuous layer or even multilayers of water in the monazite-type structure [32].

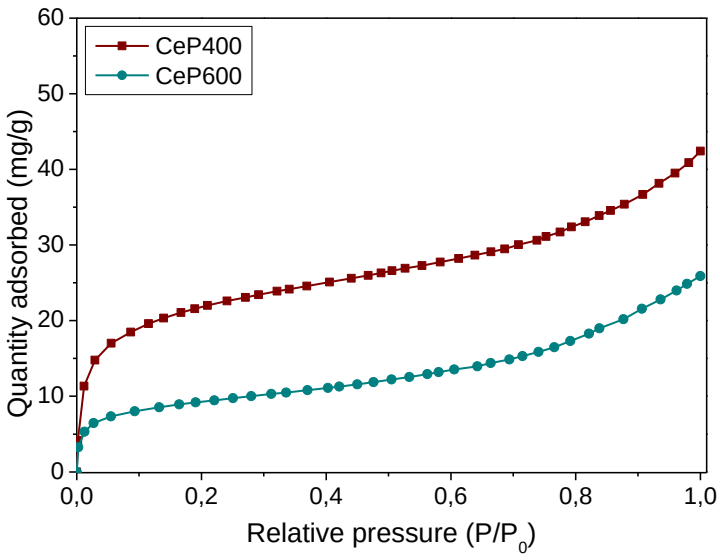

Figure 3.11. Water adsorption isotherms of the supports at 20°C

3.4. Synthesis of 2 wt.% Pt catalysts

2 wt.% Pt/CeP400 and Pt/CeP600 catalysts were prepared by the wet impregnation method, as described in the section 3.4 of the present chapter. Both catalysts were calcined at 350 °C for 2 hours.

3.5. Physicochemical characterization of the Pt catalysts

3.5.1. X-Ray Diffraction analyses

XRD patterns of the prepared catalysts are shown in Figure 3.15. After Pt deposition and subsequent calcination at 350 °C, the structure of both supports is preserved and no peaks associated to Pt or PtO_2 were observed, indicating the small crystallite size of the Pt species.

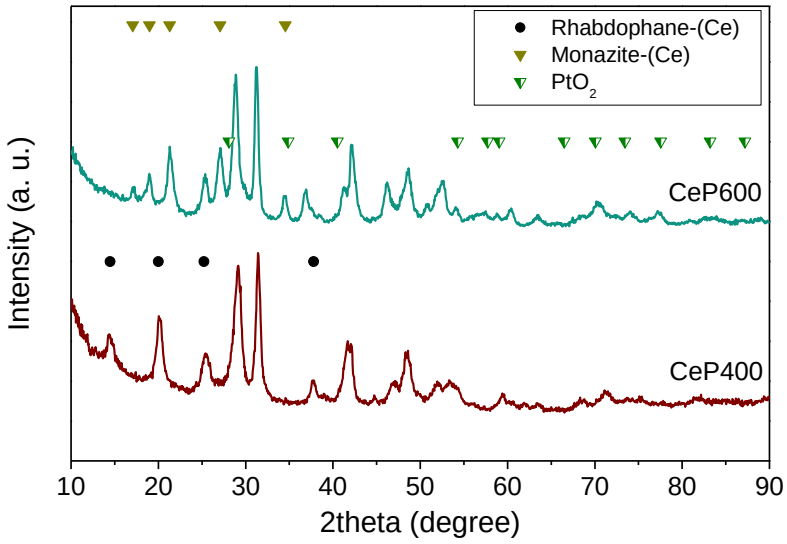

Figure 3.15. XRD patterns of the Pt catalysts after calcination at 350 °C

3.5.2. Chemical composition and textural properties

Metal content of the samples determined by ICP are shown in Table 3.6. Both samples present a Pt content almost identical and close to the nominal one.

Table 3.6. Pt content of the prepared catalysts after calcination at 350 °C

Sample	Pt (wt. %)
2% Pt/CeP400	1.5
2% Pt/CeP600	1.4

Figure 3.16 displays the N_2 adsorption/desorption isotherms of the Pt catalysts. The shape of the isotherms is similar to that observed for the supports, suggesting that Pt deposition does not influence substantial changes in the textural properties of the materials. However, the N_2 adsorption capacity of Pt/CeP600 is slightly smaller than that of the corresponding support, which could be related to little changes in the pore structure of the material after Pt incorporation.

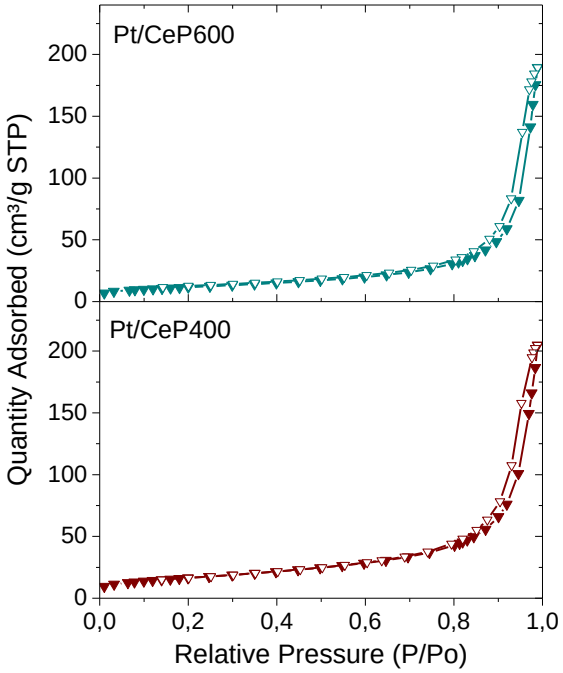

Figure 3.16. Nitrogen adsorption/desorption isotherms of the Pt catalysts (adsorption: full triangles, desorption: empty triangles)

Textural properties derived from the N_2 isotherms are presented in Table 3.7. The pore volume and pore diameter of Pt/CeP400 are practically the same than those of the support, indicating no significant changes in the porosity of the material after metal deposition. Conversely, a decrease of the pore volume and pore diameter of Pt/CeP600 is observed, which points out the support pore blocking as a consequence of the Pt deposition [57]. According to the BJH pore size distribution (Figure 3.17), both supports present a multimodal pore structure, containing both the mesopores and the interparticle voids.

Table 3.7. Textural properties of the Pt catalysts

Sample	S_{BET} ($m^2 \cdot g^{-1}$)	V_p ($cm^3 \cdot g^{-1}$)	D_p (Å)
Pt/CeP400	71	0.32	166
Pt/CeP600	44	0.30	232

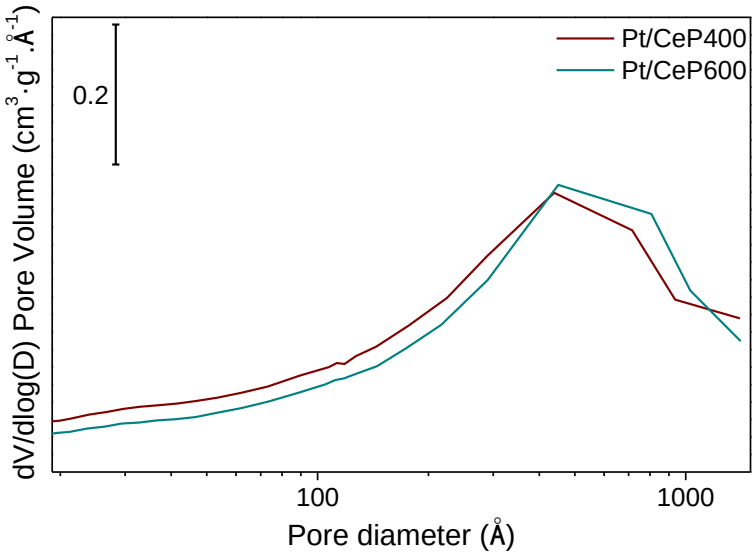

Figure 3.17. BJH pore size distribution of the Pt catalysts

3.5.3. Transmission Electron Microscopy (TEM)

Figure 3.18 shows TEM micrographs and Pt particle size distributions of the prepared catalysts. The support CeP400 maintains the structural channels, which are missed in the support CeP600. Pt species are highly dispersed and present a narrow particle size distribution in both catalysts, in good agreement with XRD results. The mean metal particle sizes are 1 and 1.2 nm in Pt/CeP400 and Pt/CeP600 respectively, with a higher population of Pt particles below and equal to 1 nm in the Pt/CeP400 catalyst. Additionally, Pt particles in Pt/CeP400 seem to be organized following the direction of the support channels, suggesting that a preferential arrangement of the metallic particles could be occurring due to the structural characteristics of the support and laying out the possibility of the Pt particles with sizes below 0.6 nm to occupy the structural support channels.

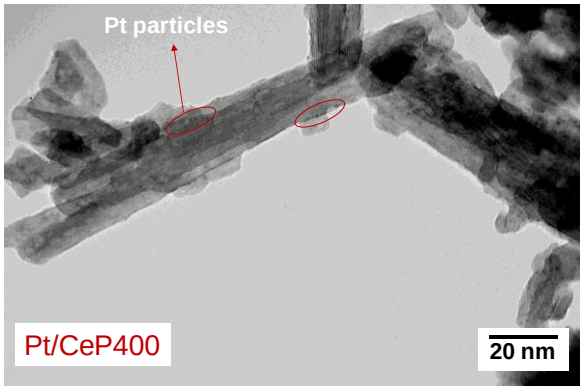

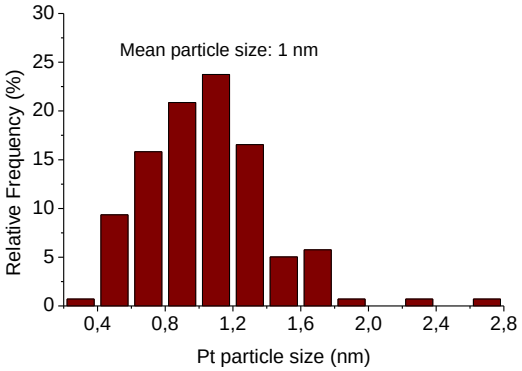

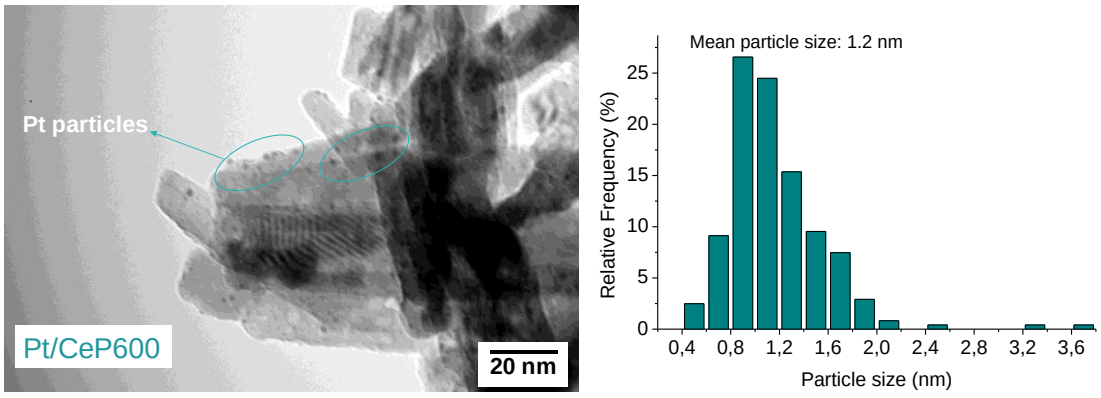

Figure 3.18. TEM micrographs and Pt particle size distribution of the prepared catalysts

The Pt dispersion values of the reduced catalysts were calculated by H_2 chemisorption, being 66% for Pt/CeP400 and 54% for Pt/CeP600. These dispersion values correspond to a Pt mean particle size of 1.5 and 1.8 nm, respectively, in good agreement with the results obtained by TEM.

3.5.4. X-Ray Photoelectron Spectroscopy (XPS)

Ce 3d, P 2p and O 1s regions of the XPS spectra of the corresponding catalysts did not present differences with respect to the bare supports. Pt 4f region before and after the reduction treatment is presented in Figure 3.19. The XPS spectra of both catalysts show two peaks, corresponding to the spin-orbit split $4f_{5/2}$ and $4f_{7/2}$ levels. After the reduction treatment, both peaks are shifted towards lower binding energies, indicating the reduction of the Pt particles in both samples.

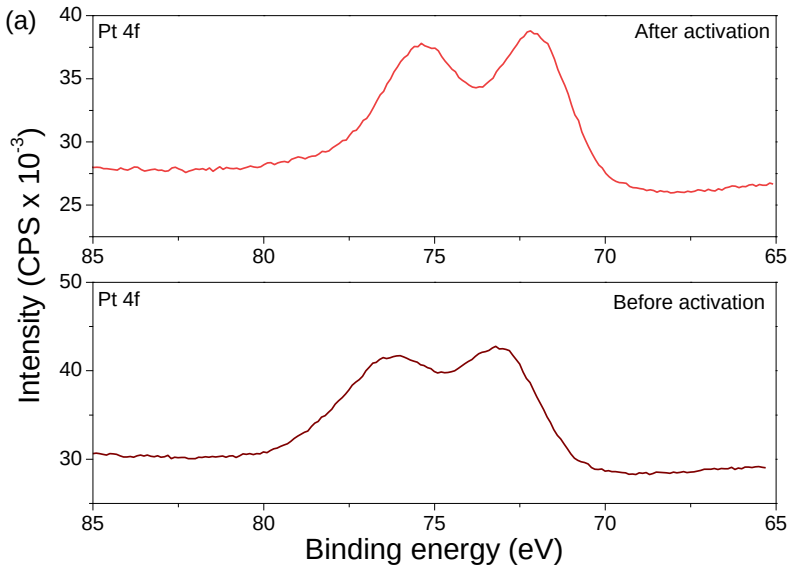

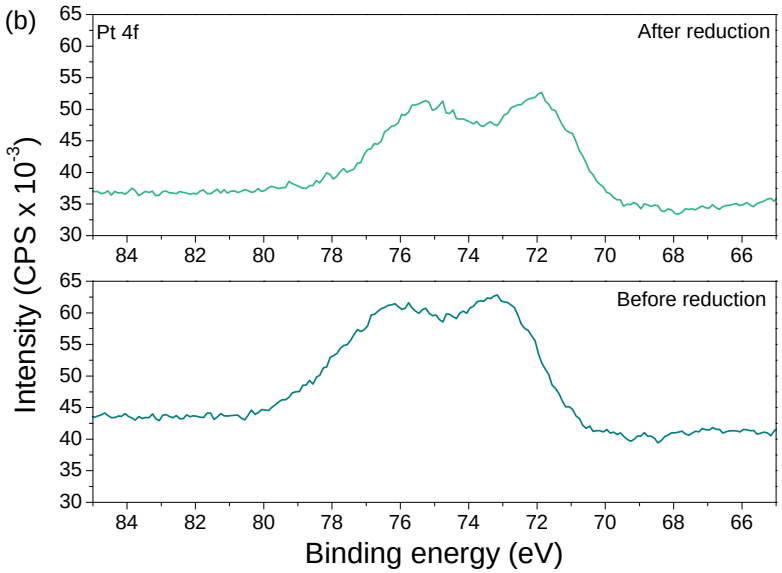

Figure 3.19. Pt 4f XPS spectra of the catalysts before and after the reduction treatment, (a) Pt/CeP400, (b) Pt/CeP600

3.5.5. Raman spectroscopy

Raman spectra of the catalysts are presented in Figure 3.20. The results are similar to those obtained for the corresponding supports, but an additional band at ca. 600 cm^{-1}, attributed to PtO_x species [58, 59], is observed.

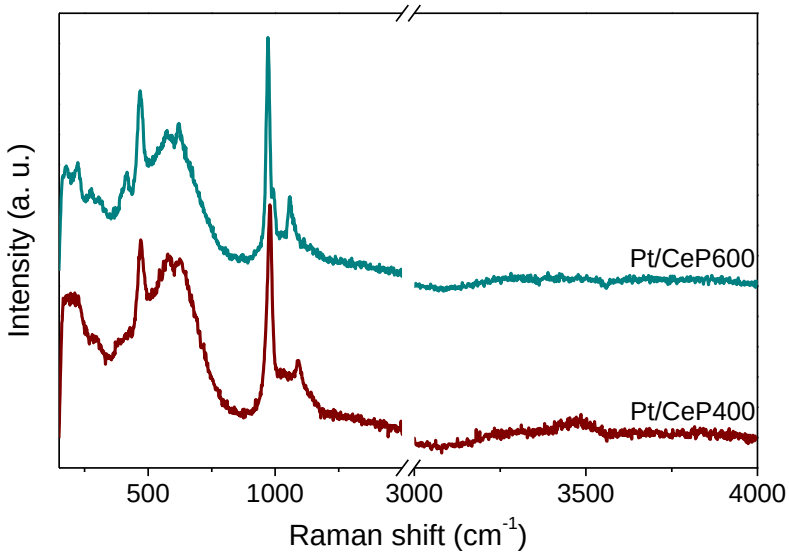

Figure 3.20. Raman spectra of the Pt catalysts

3.5.6. Isothermal adsorption of water

Figure 3.21 shows the water adsorption isotherms of both Pt catalysts at 20 °C. The shape of the isotherms does not change with respect to those of the supports. Whereas the adsorption capacity of the solid Pt/CeP600 remains almost unchanged with respect to the corresponding support, the system Pt/CeP400 presents an adsorption capacity 1.3 times superior to that of the support CeP400 (at $P/P_0 = 1$) , pointing out the capacity of Pt to adsorb water in this solid, that has been extensively reported [60, 61].

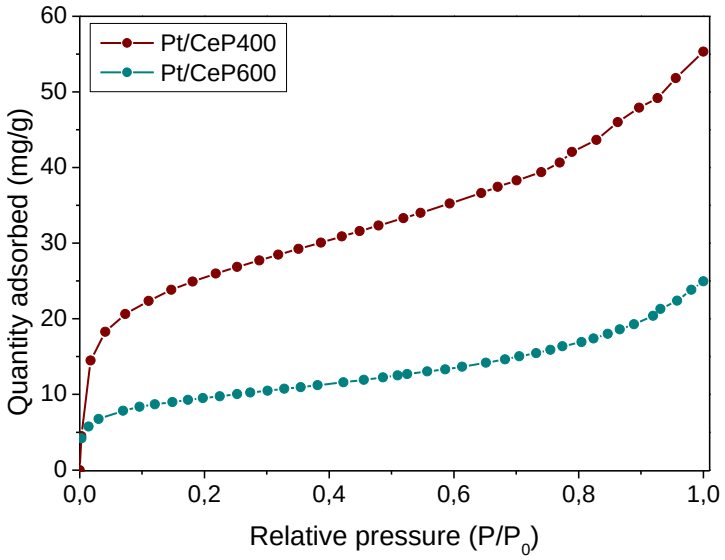

Figure 3.21. Water adsorption isotherms of the catalysts at 20 °C

3.6. Synthesis of Au and Cu-based catalysts

Since the support CeP400 seems to present a superior water adsorption capacity according to the results obtained during the isothermal adsorption of water experiments, this solid was selected for the preparation and preliminary study of the catalysts. Concerning the active phases, Cu and Au were selected, considering their previous successful application in the WGS reaction [3, 8, 9].

The 10 wt.% Cu/CeP400 catalyst was prepared by the wet impregnation method, similarly to the Pt one. The required amount of $C_2H_3CuO_2$ (> 93%, Tokyo Chemical Industry) was diluted in distilled water and the corresponding support was added. The mixture was kept under stirring for 24 hours and the solid was then dried at 60 °C and finally calcined at 350 °C for 2 hours.

The 2 wt.% Au/CeP400 catalyst was prepared through a deposition-precipitation process previously reported [43]. The required amount of $HAuCl_4 \cdot 3H_2O$ (49.81% w/w metal content, Johnson Matthey) was dissolved in distilled water and the pH was adjusted to 9 using NaOH 0.1 M. The solution was heated at 65 °C and the support was added. The mixture was kept under vigorous stirring at 65 °C for 1 hour. The obtained solid was filtered, thoroughly washed with water and dried overnight at 100 °C. Finally, the resulting catalyst was calcined at 350 °C for 2 hours.

3.7. Physicochemical characterization of Cu and Au catalysts

3.7.1. XRD analyses

The diffraction patterns of the prepared catalysts are shown in Figure 3.12. After metal deposition and calcination at 350 °C, the structure of the support is preserved in every case. No diffraction peaks associated to metal species were observed for the 2 wt.% Au catalyst, indicating the small crystallite size of them in these solids. Regarding the 10 wt.% Cu catalyst, peaks associated to the presence of CuO (JCPDS-ICDD 00-041-0254) were observed. The crystallite size of the metal species was calculated using the X-ray line broadening of the (-111) plane (35.539 °2θ), being 29.9 nm, which is consistent with the greater metal loading in this catalyst.

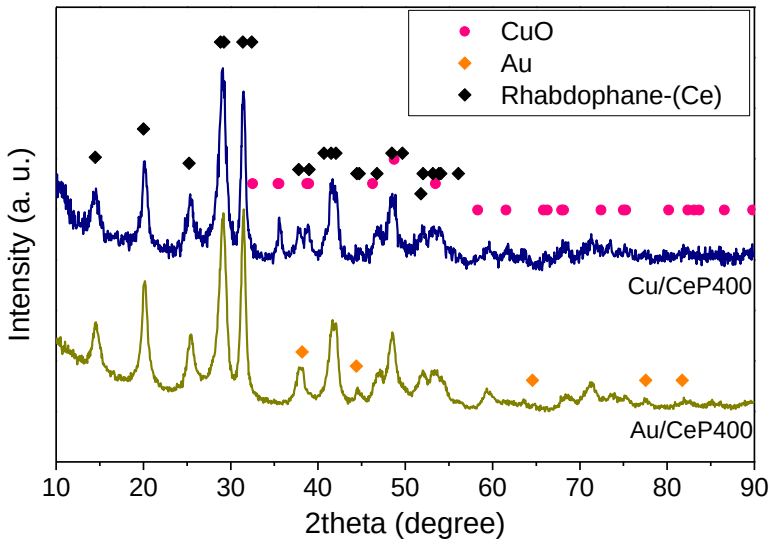

Figure 3.12. XRD patterns of the prepared catalysts after calcination at 350 °C

3.7.2. Chemical composition and textural properties

Table 3.4 shows the metal content of the catalysts obtained by ICP. In every case, the metal content is similar to the nominal value.

Table 3.4. Metal content of the prepared catalysts after calcination at 350 °C

Sample	Au (wt. %)	Pt (wt. %)	Cu (wt. %)
2% Au/CeP400	1.8	-	-
2% Pt/CeP400	-	1.5	-
10% Cu/CeP400	-	-	11.8

The textural properties of the catalysts are summarized in Table 3.5. The properties of the catalysts with a 2 wt.% metal loading are almost identical to those observed for the supports due to the low metal content. However, a decreasing in the surface area and pore volume of the 10 wt.% Cu catalyst is remarkable, in agreement with the superior metal content of this solid and the growing of the metal particles into the support porosity.

Table 3.5. Textural properties of the catalysts

Sample	S_{BET} ($m^2 \cdot g^{-1}$)	V_p ($cm^3 \cdot g^{-1}$)	D_p (nm)
2% Au/CeP400	64	0.31	17.3
10% Cu/CeP400	51	0.29	19.3

3.7.3. Transmission Electron Microscopy (TEM)

TEM micrographs and metal particle size distributions of the catalysts are shown in Figure 3.13. The Au sample presents a narrow metal particle size distribution, centered at 0.4 nm. This could be attributed to the structural characteristics of the support. Well-ordered channel structures have demonstrated to favor good dispersion of the metal particles, as well as prevent them of sintering [62]. Nevertheless, although the Cu catalyst presents small metal particles with a mean size of 2.5 nm, some particles larger than 20 nm are observed, whose presence can be attributed to the greater metal content in this solid. This result is in concordance with the Cu crystallite size calculated by XRD.

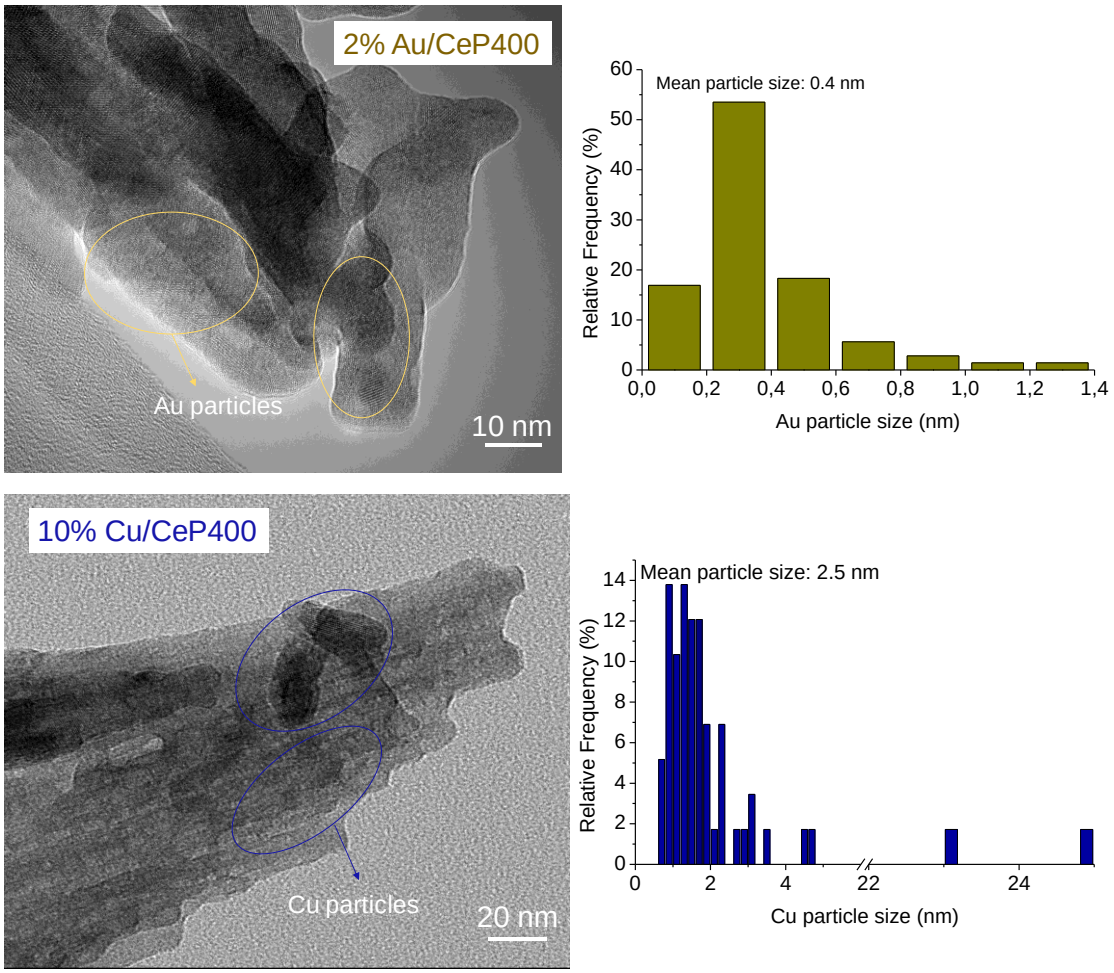

Figure 3.13. TEM micrographs of the Au and Cu catalysts after calcination at 350 °C

3.3. Partial conclusions

$CePO_4$ has been prepared successfully through a hydrothermal synthesis method. The calcination of the obtained material at 400 °C and 600 °C has allowed to obtain the hexagonal (rhabdophane-type) and monoclinic (monazite-type) structures of $CePO_4$, respectively. Characterization results expose important differences between both structures. Whereas the rhabdophane-type phase presents a series of parallel structural channels stabilized by the presence of molecular water, the calcination at higher temperature provokes a compaction of the crystal structure as a consequence of the total dehydration of the solid. The structural characteristics of the solids influence their interaction with the water molecule. The presence of channels in the rhabdophane-type phase structure seems to enhance the water adsorption capacity to a greater extent, whereas the monazite-type phase interacts with the water molecule

via formation of a water continuous layer or multilayer, which supposes that a weaker interaction takes place.

Characterization results of the $Pt/CePO_4$ catalysts show that the structure of the supports is not altered by the Pt deposition. Additionally, both catalysts present narrow particle size distribution and small mean particle size of the Pt species. Particularly, the rhabdophane-type phase of the support seems to control the growth of the metal particles in the direction of the channels, which suggests a possible arrangement of some Pt particles inside the structural channels of the support.

According to the enhanced interaction with water, the rhabdophane-type phase has been selected for its use as support for 10% Cu and 2% Au catalysts, which will be compared in terms of catalytic activity with the Pt system in the following chapter.

2.4. References

1. Kalamaras, C.M., et al., *Effects of Reaction Temperature and Support Composition on the Mechanism of Water–Gas Shift Reaction over Supported-Pt Catalysts.* The Journal of Physical Chemistry C, 2011. **115**(23): p. 11595-11610.

2. Cargnello, M., et al., *Control of Metal Nanocrystal Size Reveals Metal-Support Interface Role for Ceria Catalysts.* Science, 2013. **341**: p. 771-773.

3. Gonzalez Castaño, M., et al., *Pt vs. Au in water–gas shift reaction.* Journal of Catalysis, 2014. **314**: p. 1-9.

4. Boaro, M., et al., *A comparative study of water gas shift reaction over gold and platinum supported on ZrO2 and CeO2–ZrO2.* Applied Catalysis B: Environmental, 2009. **88**(3-4): p. 272-282.

5. Vignatti, C., et al., *Catalytic and DRIFTS study of the WGS reaction on Pt-based catalysts.* International Journal of Hydrogen Energy, 2010. **35**(14): p. 7302-7312.

6. Byron, S.R.J., M. Loganathan, and M.S. Shanthaz, *A Review of the Water Gas Shift Reaction Kinetics.* International Journal of Chemical Reactor Engineering, 2010. **8**.

7. Pal, D.B., et al., *Performance of water gas shift reaction catalysts: A review.* Renewable and Sustainable Energy Reviews, 2018. **93**: p. 549-565.

8. Ratnasamy, C. and J.P. Wagner, *Water Gas Shift Catalysis.* Catalysis Reviews, 2009. **51**(3): p. 325-440.

9. Price, C., et al., *Highly active Cu-ZnO catalysts for the WGS reaction at medium–high space velocities: Effect of the support composition.* International Journal of Hydrogen Energy, 2017. **42**(16): p. 10747-10751.

10. Mendes, D., et al., *The water-gas shift reaction: from conventional catalytic systems to Pd-based membrane reactors-a review.* Asia-Pacific Journal of Chemical Engineering, 2010. **5**(1): p. 111-137.

11. González-Castaño, M., et al., *O 2 -assisted Water Gas Shift reaction over structured Au and Pt catalysts.* Applied Catalysis B: Environmental, 2016. **185**: p. 337-343.

12. González-Castaño, M., et al., *Deep insight into Zr/Fe combination for successful Pt/CeO2/Al2O3WGS catalyst doping.* Catalysis Science & Technology, 2017. **7**(7): p. 1556-1564.

13. Reina, T.R., et al., *Boosting the activity of a Au/CeO 2 /Al 2 O 3 catalyst for the WGS reaction.* Catalysis Today, 2015. **253**: p. 149-154.

14. Phatak, A.A., et al., *Kinetics of the water–gas shift reaction on Pt catalysts supported on alumina and ceria.* Catalysis Today, 2007. **123**(1-4): p. 224-234.

15. Panagiotopoulou, P. and D.I. Kondarides, *Effect of the nature of the support on the catalytic performance of noble metal catalysts for the water–gas shift reaction.* Catalysis Today, 2006. **112**(1-4): p. 49-52.

16. Pazmiño, J.H., et al., *Metallic Pt as active sites for the water–gas shift reaction on alkali-promoted supported catalysts.* Journal of Catalysis, 2012. **286**: p. 279-286.

17. Ammal, S.C. and A. Heyden, *Water–Gas Shift Catalysis at Corner Atoms of Pt Clusters in Contact with a TiO2 (110) Support Surface.* ACS Catalysis, 2014. **4**(10): p. 3654-3662.

18. Li, L., et al., *Black TiO2−x with stable surface oxygen vacancies as the support of efficient gold catalysts for water-gas shift reaction.* Catalysis Science & Technology, 2018. **8**(5): p. 1277-1287.

19. Graciani, J. and J.F. Sanz, *Designing a new generation of catalysts: Water gas shift reaction example.* Catalysis Today, 2015. **240**: p. 214-219.

20. Vecchietti, J., et al., *Understanding the Role of Oxygen Vacancies in the Water Gas Shift Reaction on Ceria-Supported Platinum Catalysts.* ACS Catalysis, 2014. **4**(6): p. 2088-2096.

21. Jain, R., et al., *Comparative study for low temperature water-gas shift reaction on Pt/ceria catalysts: Role of different ceria supports.* Applied Catalysis A: General, 2015. **507**: p. 1-13.

22. Deng, W. and M. Flytzani-Stephanopoulos, *On the Issue of the Deactivation of Au–Ceria and Pt–Ceria Water–Gas Shift Catalysts in Practical Fuel-Cell Applications.* Angewandte Chemie International Edition, 2006. **45**(14): p. 2285-2289.

23. González, I.D., et al., *A comparative study of the water gas shift reaction over platinum catalysts supported on CeO2, TiO2 and Ce-modified TiO2.* Catalysis Today, 2010. **149**(3-4): p. 372-379.

24. Petallidou, K.C., C.M. Kalamaras, and A.M. Efstathiou, *The effect of La3+, Ti4+ and Zr4+ dopants on the mechanism of WGS on ceria-doped supported Pt catalysts.* Catalysis Today, 2014. **228**: p. 183-193.

25. Zhai, Y., et al., *Alkali-stabilized Pt-OHx species catalyze low-temperature water-gas shift reactions.* Science, 2010. **329**(5999): p. 1633-6.

26. García-Moncada, N., et al., *A direct in situ observation of water-enhanced proton conductivity of Eu-doped ZrO 2 : Effect on WGS reaction.* Applied Catalysis B: Environmental, 2018. **231**: p. 343-356.

27. Peighambardoust, S.J., S. Rowshanzamir, and M. Amjadi, *Review of the proton exchange membranes for fuel cell applications.* International Journal of Hydrogen Energy, 2010. **35**(17): p. 9349-9384.

28. Kreuer, K.-D., et al., *Transport in Proton Conductors for Fuel-Cell Applications: Simulations, Elementary Reactions, and Phenomenology.* Chemical Reviews, 2004. **104**: p. 4637-4678.

29. Kreller, C.R., et al., *Intragranular Phase Proton Conduction in Crystalline Sn1–xInxP2O7 (x = 0 and 0.1).* The Journal of Physical Chemistry C, 2017. **121**(43): p. 23896-23905.

30. Baies, R., et al., *New Layered Hydrogenophosphate, Protonic Conductor: Mn(H2PO4)2.* Inorganic Chemistry, 2008. **47**: p. 6072-6076.

31. Parangi, T., B. Wani, and U. Chudasama, *A Comparative Study of Proton Transport Properties of Cerium (IV) and Thorium (IV) Phosphates.* Electrochimica Acta, 2014. **148**: p. 79-84.

32. Pusztai, P., et al., *Structure-Independent Proton Transport in Cerium(III) Phosphate Nanowires.* ACS Appl Mater Interfaces, 2015. **7**(18): p. 9947-56.

33. Horváth, I., A. Bondar, and L.P. Mezentseva, *Termochemistry of Hydrated Rare Earth Ortophosphates.* Journal of Thermal Analysis, 1988. **33**: p. 755-760.

34. Anfimova, T., et al., *Thermal Stability and Proton Conductivity of Rare Earth Ortophosphates Hydrates.* International Journal of Electrochemical Science, 2014. **9**: p. 2285-2300.

35. Lucas, S., et al., *Rare earth phosphate powders RePO4·nH2O (Re=La, Ce or Y) II. Thermal behavior.* Journal of Solid State Chemistry, 2004. **177**(4-5): p. 1312-1320.

36. Assaaoudi, H., A. Ennaciri, and A. Rulmont, *Vibrational spectra of hydrated rare earth ortophosphates.* Vibrational Spectroscopy, 2001. **25**: p. 81-90.

37. Ochiai, A. and S. Utsunomiya, *Crystal Chemistry and Stability of Hydrated Rare-Earth Phosphates Formed at Room Temperature.* Minerals, 2017. **7**(6): p. 84.

38. Mooney, R.C.L., *X-ray Diffraction Study of Cerous Phosphate and Related Crystals. I. Hexagonal modification.* Acta Crystallographica, 1950. **3**: p. 337-340.

39. Mooney, R.C.L., *Crystal Structures of a Series of Rare Earth Phosphates.* The Journal of Chemical Physics, 1948. **16**(10): p. 1003-1003.

40. Fang, Y.P., et al., *Systematic Synthesis and Characterization of Single-Crystal Lanthanide Ortophosphate Nanowires.* Journal of the American Chemical Society, 2003. **125**: p. 16025-16034.

41. Macalik, L., et al., *Optical and structural characterisation of pure and Pr3+ doped LaPO4 and CePO4 nanocrystals.* Journal of Alloys and Compounds, 2011. **509**(27): p. 7458-7465.

42. Diaz-Guillén, J.A., et al., *A rapid method to obtain nanometric particles of rhabdophane LaPO4·nH2O by mechanical milling.* Journal of Alloys and Compounds, 2007. **427**(1-2): p. 87-93.

43. Romero-Sarria, F., et al., *CO oxidation at low temperature on Au/CePO4: Mechanistic aspects.* Applied Catalysis B: Environmental, 2011. **107**(3-4): p. 268-273.

44. Pusztai, P., et al., *Structural stability test of hexagonal CePO4 nanowires synthesized at ambient temperature.* Journal of Molecular Structure, 2013. **1044**: p. 94-98.

45. Mesbah, A., et al., *Monoclinic Form of the Rhabdophane Compounds: REEPO4·0.667H2O.* Crystal Growth & Design, 2014. **14**(10): p. 5090-5098.

46. Leofanti, G., et al., *Surface area and pore texture of catalysts.* Catalysis Today, 1998. **41**: p. 207-219.

47. Lucas, S., et al., *Rare earth phosphate powders RePO4·nH2O (Re=La, Ce or Y)—Part I. Synthesis and characterization.* Journal of Solid State Chemistry, 2004. **177**(4-5): p. 1302-1311.

48. Ho, L.-N., et al., *Preparation of mesoporous nanocrystalline cerium phosphate with controllable pore size by using chelating agent.* Materials Chemistry and Physics, 2006. **97**(2-3): p. 494-500.

49. Pemba-Mabiala, J.M., et al., *XPS Study of Mixed Cerium-Terbium Ortophosphate Catalysts.* Surface and Interface Analysis, 1990. **15**.

50. Le Normand, F., et al., *Oxidation State of Cerium in Cerium-Based Catalysts Investigated by Spectroscopic Probes.* Journal of Physical Chemistry, 1988. **92**: p. 663-667.

51. Praline, G., et al., *X-Ray Photoelectron Study of the Reaction of Oxygen with Cerium.* Journal of Electron Spectroscopy and Related Phenomena, 1980. **21**.

52. Herbst, J.F., J.M. Burkstrand, and J.W. Wilkins, *Low-binding-energy satellites in rare-earth-metal 3d spectra: An exception at Eu.* Physical Review B, 1980. **22**(2): p. 531-533.

53. Orera, V.M., R.I. Merino, and F. Peña, *Ce3+/Ce4+ conversion in ceria-doped zirconia single crystals induced by oxido-reduction treatments.* Solid State Ionics, 1994. **72**.

54. García-Moncada, N., et al., *New concept for old reaction: Novel WGS catalyst design.* Applied Catalysis B: Environmental, 2018. **238**: p. 1-5.

55. Chusuei, C.C. and D.W. Goodman, *Calcium Phosphate Phase Identification Using XPS and Time-of-Flight Cluster SIMS.* Analytical Chemistry, 1999. **71**: p. 149-153.

56. Thommes, M., et al., *Combining nitrogen, argon, and water adsorption for advanced characterization of ordered mesoporous carbons (CMKs) and periodic mesoporous organosilicas (PMOs).* Langmuir, 2013. **29**(48): p. 14893-902.

57. Kónya, Z., et al., *Synthetic Insertion of Gold Nanoparticles into Mesoporous Silica.* Chemistry of Materials, 2003. **15**: p. 1242-1248.

58. Huang, Y.F., P.J. Kooyman, and M.T. Koper, *Intermediate stages of electrochemical oxidation of single-crystalline platinum revealed by in situ Raman spectroscopy.* Nat Commun, 2016. **7**: p. 12440.

59. Zhang, Y., X. Gao, and M.J. Weaver, *Nature of Surface Bonding on Voltammetrically Oxidized Noble Metals in Aqueous Media As Probed by Real-Time Surface-Enhanced Raman Spectroscopy.* Journal of Physical Chemistry, 1993. **97**: p. 8656-8663.

60. Motobayashi, K., et al., *Adsorption of Water Dimer on Platinum (111): Identification of the -OH···Pt Hydrogen Bond.* ACS Nano, 2014. **8**(11): p. 11583-11590.

61. Árnadóttir, L., E.M. Stuve, and H. Jónsson, *Adsorption of water monomer and clusters on platinum(111) terrace and related steps and kinks.* Surface Science, 2010. **604**(21-22): p. 1978-1986.

62. Parapat, R.Y., et al., *Support effect in the preparation of supported metal catalysts via microemulsion.* RSC Adv., 2014. **4**(92): p. 50955-50963.

Chapter IV

Catalytic activity and *in situ/operando* spectroscopic studies

Abstract

Considering the importance of water availability during the WGS reaction and the intrinsic hydrophilicity of the $CePO_4$ supports displayed in Chapter III, the objective of this chapter is the evaluation of the catalytic performance of the corresponding catalysts under WGS reaction mixtures with different compositions. Additionally, *in situ* water adsorption experiments followed by DRIFTS were performed in order to stablish new insights about the role of the water molecule on the WGS catalytic performance. Finally, the WGS reaction mechanism is evaluated and correlated to the catalytic activity results.

4.1. Introduction

As mentioned in Chapter III, the use of noble metal catalysts as suitable materials for their application in the WGS reaction for fuel cell mobile applications has been widely reported [1-6]. However, some aspects of their practical application need to be considered. Added to the requirements of high activity, selectivity and stability in the operation conditions, an additional requisite for these systems is their operation under the WGS fuel processing environment, which is a reducing atmosphere at temperatures ranging from 180 to 450 °C, containing both H_2 and CO_2 in the reactive mixture [7-9]. Consequently, the achievement of a good WGS catalytic performance makes mandatory an appropriate design of the catalyst in terms of the selection of the active phase and the support [10, 11]. Therefore, the understanding of the WGS reaction mechanism at the molecular level is fundamental [12].

Although the WGS reaction mechanism has been thoroughly studied [12-16], there is still controversy about the reaction path. However, two mechanisms have been generally proposed: the redox and the associative mechanism [7, 17, 18].

In the redox mechanism, the oxidation-reduction cycles occurring in the support are responsible for the WGS reaction. CO adsorbs on metal sites and reacts with the oxygen of the support to yield CO_2, whereas the oxygen vacancy generated in the support is reoxidized by H_2O. The interaction of water with the vacancies of the solid generates OH groups and, eventually, H. This mechanism has been typically observed on partially reduced oxides containing oxygen vacancies, such as TiO_2, CeO_2 or CeO_2-ZrO_2 [7].

On the contrary, the associative mechanism is an adsorption-desorption model where the adsorbed species interact to form an adsorbed intermediate which decomposes in the reaction products. Thus, it implies the adsorption of CO and H_2O on the catalyst surface to form a surface intermediate such as formate, carbonate or carbonyl species, that decompose to the reaction products, CO_2 and H_2 [7, 12, 19].

Nevertheless, a combination of both reaction mechanisms is also possible. Regardless of the mechanism, a generally accepted conclusion is that OH/H diffusion processes derived from water dissociation and/or hydrogen spillover are crucial steps of the WGS reaction; thus, availability of

water is a key step for the successful development of this process, being water activation described as the WGS rate-limiting step [20-22].

Considering the previously mentioned aspects, this chapter covers the catalytic activity studies of the phosphate-type supports and metal catalysts described in Chapter III. In order to explain the catalytic behavior of the solids, a series of *in situ* and *operando* spectroscopic studies were performed both in the presence of water and the reaction mixture, showing a clear correlation between the type of interaction with the reactants and the observed catalytic trends.

4.2. Catalytic activity of $CePO_4$-based systems on the WGS reaction

Catalytic activity tests of the prepared solids were carried out using two different feed-streams, A and B, as indicated in Chapter II. The volume percent composition of both feed-streams is shown in Table 4.1. Every experience was performed at WHSV = 30 $L \cdot g^{-1} \cdot h^{-1}$, according to equation 2.9 (Chapter II).

Table 4.1. Composition of the WGS reaction mixtures

Reactant	Feed A (Vol %)	Feed B (Vol %)
CO	4.5	7.0
H_2O	30.0	30.0
N_2	65.5	4.0
CO_2	-	9.0
H_2	-	50.0

WGS catalytic activity results of the supports and the Pt catalysts under feed-streams A and B are shown in Figure 1.4. Both CeP supports in the absence of metal phase present no activity towards the WGS reaction. Nevertheless, the corresponding Pt catalysts achieve high conversions under both feed-streams A and B, although the catalyst Pt/CeP400 presents higher catalytic activity than Pt/CeP600. Under feed A, Fig. 1.4 (a), Pt/CeP400 leads Pt/CeP600 until 270 °C, temperature at which the performance of both catalysts becomes similar, reaching equilibrium conversion at 290 °C. Under feed B, Fig. 1.4 (b), both catalysts follow the same trend compared to the case in the absence of reaction products, with the solid Pt/CeP400 being more active than Pt/CeP600. When the feed contains CO_2 and H_2, differences in catalytic activity are

more pronounced, and both catalysts reach equilibrium conversion at 350 °C. Under no conditions does methanation take place.

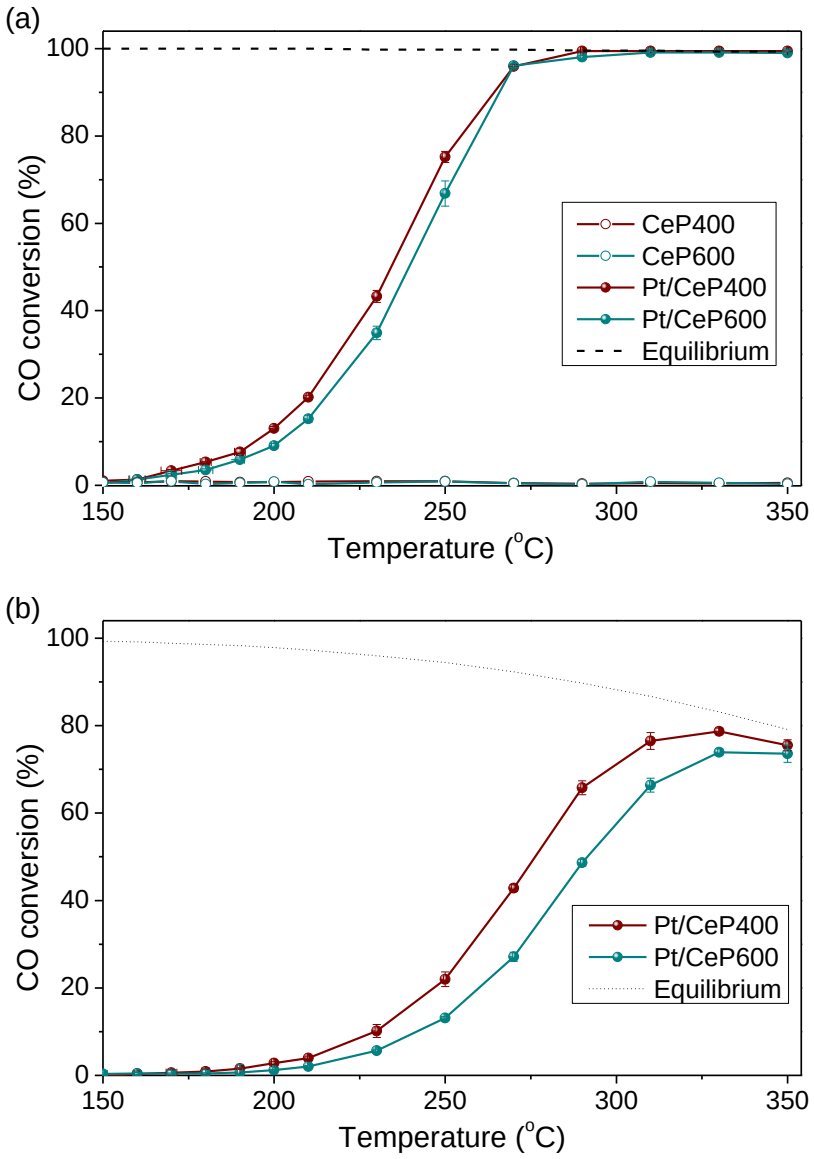

Figure 4.1. CO conversion as a function of the reaction temperature under (a) feed A (4.5% CO, 30% H_2O and 65.5% N_2), (b) feed B (7% CO, 9% CO_2, 30% H_2O, 50% H_2 and 4% N_2). The equilibrium conversion curve is also presented

Figure 4.2 shows the Arrhenius-type plot of the studied catalysts. Rates and apparent activation energies (E_a) were calculated at low conversions under both feed-streams. Under reaction feed A, the reaction rates are similar and E_a has a value of 86 kJ·mol^{-1} for both catalysts. However, in the presence of CO_2 and H_2, the CO consumption rate decreases for both catalysts, although it is higher for the Pt/CeP400 catalyst. The values of E_a increase with respect to those in the absence of products, being 91 kJ·mol^{-1} for Pt/CeP400 and 109 kJ·mol^{-1} for Pt/CeP600. In order

to compare the obtained E_a values with those previously obtained by other authors, Table 4.2 presents a summary of reported activation energies for Pt catalysts. E_a values for both $CePO_4$-based catalysts are similar to those previously calculated for Pt catalysts in different supports.

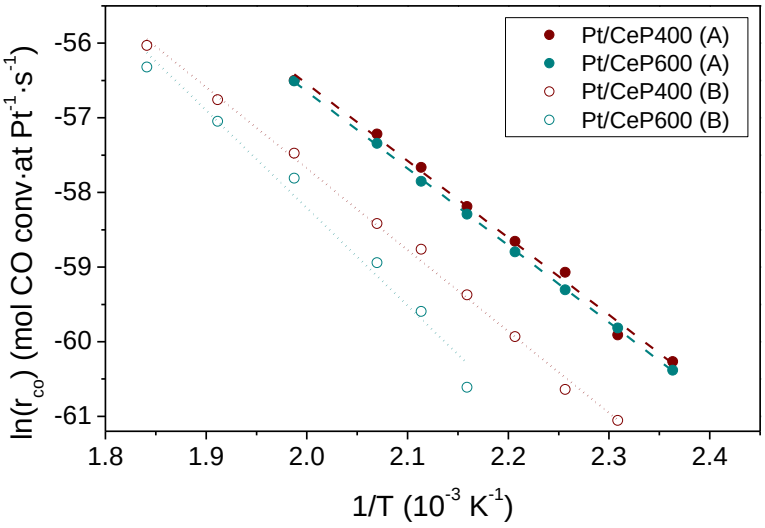

Figure 4.2. Arrhenius-type plot of the $Pt/CePO_4$ catalysts in the absence (A) and in the presence (B) of the reaction products

Table 4.2. Summary of reported activation energy values for Pt catalysts

Catalyst	E_a (kJ·mol^{-1})	Feed stream	Ref.
1.66% Pt/Al_2O_3	81	6.8% CO, 8.5% CO_2, 22% H_2O, 37.3% H_2, balance Ar	[23]
1% Pt/CeO_2	75		
0.82% Pt/Al_2O_3	74	6.8% CO, 8.5% CO_2, 21.9% H_2O, 37.4% H_2, balance Ar	[24]
1.7% $Pt/CeO_2/Al_2O_3$	86	7% CO, 9% CO_2, 30% H_2O, 50% H_2, balance N_2	[5]
0.82% Pt/HAp	89	15% CO, 5% CO_2, 30% H_2O, 40% H_2, balance N_2	[25]
1% Pt/SrHAp	72		[26]
1.5% Pt/CeP400	91	7% CO, 9% CO_2, 30% H_2O, 50% H_2, balance N_2	This work
1.4% Pt/CeP600	109		

The superior reaction rate and lower E_a of Pt/CeP400 could be related to the presence of the structural water and the hydrophilic character of the support, which could act as H_2O supplier and simultaneously accommodate H_2O molecules in its structural cavities, thus enhancing the availability of water during the WGS reaction. Considering that the noble metal is responsible for the CO activation and the support interacts with the H_2O molecules [25, 27], the greater affinity of the CeP400 support for H_2O and/or the influence of its surface -OH groups could enhance the Pt

catalytic performance, as previously reported for other phosphate-type compounds [25, 26]. Furthermore, according to the characterization results showed in Chapter III, the structure of the CeP400 support seems to control the growth and location of the Pt particles, which could have an influence on the diffusion processes of the reactive species towards the active phase during the WGS reaction.

4.3. Catalytic screening (Cu, Au and Pt)

The catalytic activity of the 2 wt.% Pt/CeP400 catalyst was compared to that of the 10% Cu and 2 wt.% Au/CeP400 ones. Figure 4.3 shows the catalytic activity results of the prepared catalysts during the WGS reaction under a feed-stream B. These experiments were performed at WHSV= 6 $L \cdot g^{-1} \cdot h^{-1}$, that is, placing 1 g of catalyst in the reactor which was subjected to 100 $ml \cdot min^{-1}$ of the reactive flow. The catalyst mass was increased in this experiment because both the Cu and Au catalysts presented no activity using 200 mg of the sample.

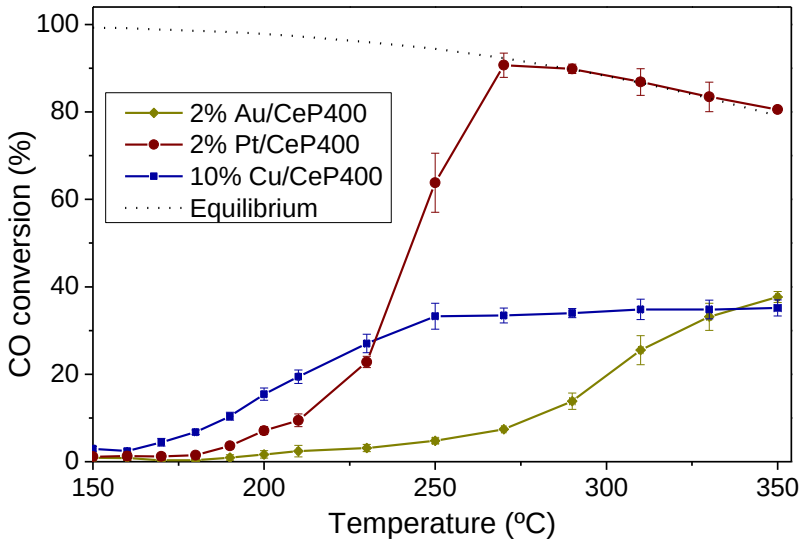

Figure 4.3. CO conversion over CeP400-supported Cu, Au and Pt as a function of the reaction temperature. The equilibrium curve is also presented

According to the results, the 10% Cu/CeP400 catalyst presents the highest catalytic activity at low temperature, reaching a CO conversion value of 33% at 250 °C, virtually constant up to 350 °C. Similarly, the Au catalyst only reaches a 38% CO conversion at 350 °C. However, the Pt catalyst reaches the equilibrium conversion at 270 °C. These results are in concordance with the

reported data, which point out the Cu catalysts activity only at low temperature and their deactivation in reductive environments as a consequence of the sintering and loss of Cu surface area [7]. In the same way, previous works have demonstrated a superior WGS catalytic performance of Au catalysts at low temperatures, whereas Pt catalysts exceed their catalytic performance from 200 °C due to its superior turnover rate [28, 29]. Consequently, this result highlights the convenient use of Pt for WGS catalysts beyond other metals typically used for the WGS reaction, as well as its selection as active phase for the catalysts studied in this work.

4.4. *In situ* water adsorption experiments followed by DRIFTS

4.4.1. $CePO_4$ supports

In order to understand the interaction of water with the surface of the supports as a function of the temperature, water adsorption experiments (10% H_2O/Ar) at different temperatures were monitored by DRIFTS. Prior to the experiments, the supports were reduced at 350 °C for 1 hour. Figure 4.4 shows the DRIFT spectra of the supports before and after the activation treatment under 10% H_2/Ar.

Bands at *ca.* 1630, 3100-3500 and 5100-5300 cm^{-1} are observed prior to the activation. In the region above 1600 cm^{-1}, bands corresponding to the H-O-H bending modes, δ(H-O-H) due to the presence of hydrogen-bonded water are expected [30]; therefore, the bands at *ca.* 1625 cm^{-1} in both supports are attributed to bound molecular water [31-33]. Bands in the 3100-3500 cm^{-1} range corresponds to the OH stretching (vOH) vibrations of bounded water. The presence of molecular water is confirmed, additionally, by the presence of bands at *ca.* 5200 cm^{-1}, corresponding to the overtones of the H_2O stretching vibrations, typically found in the 4600-5600 cm^{-1} region [34]. These water-related contributions are much more intense for the CeP400 support than for the CeP600 one. After the activation treatment, the band at 3670 cm^{-1} is attributed to surface OH groups, which are present in both supports even after activation, thus being OH belonging to the phosphate structure.

Regarding the bands corresponding to the phosphate groups, the strong absorption bands in crystalline phosphate materials are expected in the 900-1100 cm^{-1} region. Thus, the band at 960

cm^{-1} in both solids corresponds to the symmetric P-O stretching mode (v_1). Although this band is not expected to be IR active, it appears as a result of solid-state effects. The bands at 1028 cm^{-1} (CeP400) and 1090 cm^{-1} (CeP600) correspond to the asymmetric P-O stretching modes (v_3). This mode is triply degenerate, and its frequency depends on the chemical environment of the phosphate. The different frequencies of this contribution in every solid indicate the different environments of the PO_4^{3-} groups depending on the crystalline phase of $CePO_4$, in good agreement with the results obtained by Raman spectroscopy presented in Chapter III. Additionally, both solids present a band at 1185 cm^{-1}, corresponding to the P=O stretching mode [35, 36]. The bands appearing in the 2100-2400 cm^{-1} range (Figure 4.5) in the spectra of both supports are due to overtones or combination modes of the PO_4^{3-} tetrahedra. The vibration modes that give rise to these bands in every solid are summarized in Table 4.3. Finally, the band at 2884 cm^{-1} present only in the CeP400 spectra corresponds to the P-OH stretching mode characteristic of acid orthophosphates (PO_4^{3-} + H_2O) [35], revealing the presence of structural water uniquely in the rhabdophane-type phase of $CePO_4$. These data are in good agreement with those reported in the literature for $CePO_4$ [37].

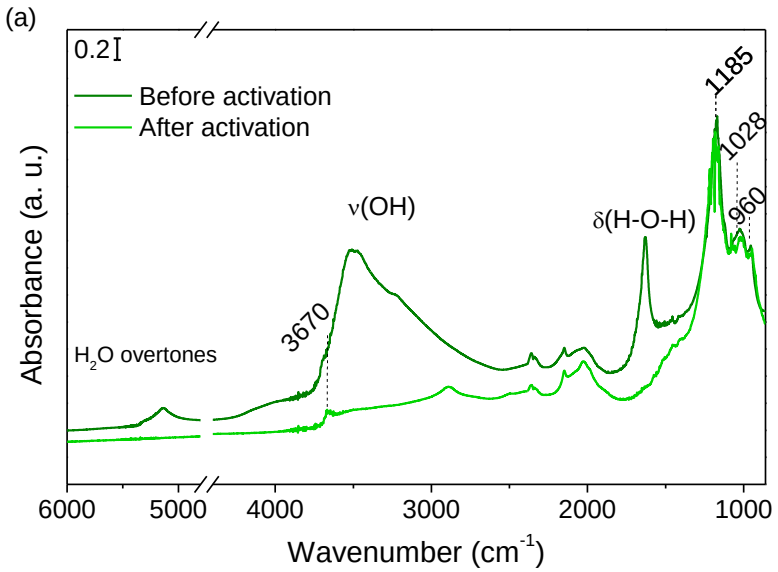

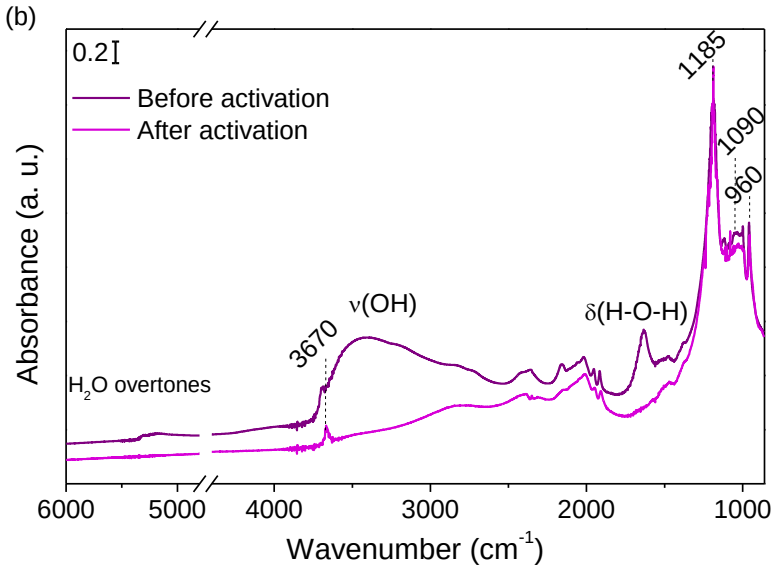

Figure 4.4. DRIFT spectra of (a) CeP400 and (b) CeP600 before and after the activation treatment under 10% H_2/Ar

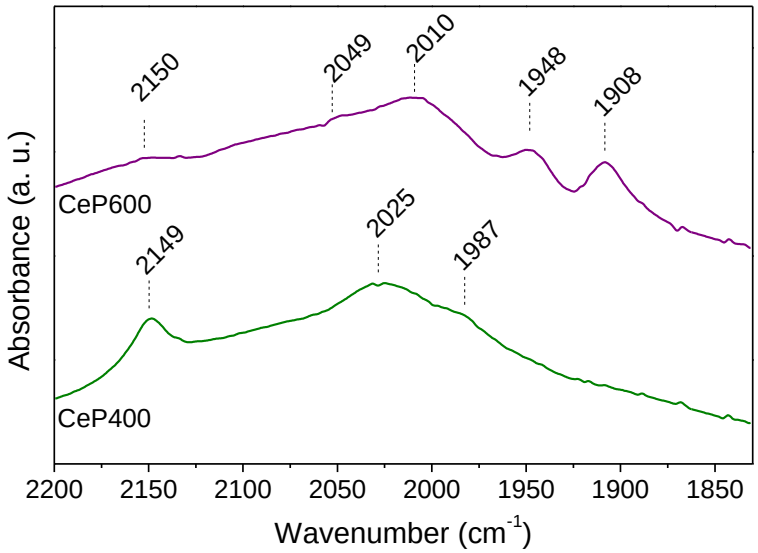

Figure 4.5. Overtones and combination bands of the phosphate groups in both supports

Table 4.3. Overtones and combination bands of the PO_4^{3-} groups in the supports

Support	Vibration frequency (cm^{-1})	Assignement
CeP400	2149	$\nu_{1(P-O)} + \nu_{(P=O)}$
	2025	$2\nu_{3(P-O)}$
	1987	$\nu_{3(P-O)} + \nu_{(P=O)}$
CeP600	2150	$\nu_{1(P-O)} + \nu_{(P=O)}$
	2049	$\nu_{3(P-O)} + \nu_{(P=O)}$
	2010	Not assigned
	1949	Not assigned
	1908	Not assigned

Figure 4.6 shows the difference spectra of the supports when water adsorption experiments were performed in the WGS temperature range, being the reference spectra that obtained after the activation treatment. The addition of water gives rise rapidly to an increase on intensity of the water-related bands in both supports. The bands at 1625 cm^{-1}, 3100-3500 cm^{-1} and 5100-5300 cm^{-1} reach their maximum intensity at 150 °C in both solids, although the greater interaction of the H_2O molecule with CeP400 is clearly observed.

For the solid CeP400, Figure 4.6 (a), the band initially at 1625 cm^{-1} (δ(H-O-H)) is gradually shifted to 1616 cm^{-1}, a value close to that of the free water (1610 cm^{-1}), indicating the gradual release of water with the temperature, whereas an additional band at relatively low frequency (1583 cm^{-1}) is visible from 250 °C and remains until 350 °C. Falk [38] found a relationship between the δ(H-O-H) frequency shift and the formal charge of the cation with which the water molecules were interacting. For the cation Ce^{3+} this value would be found at *ca*. 1532 cm^{-1}, a value much lower than that found in CeP400, thus this vibration mode has been assigned to the water present in the structural channels of the rhabdophane-type phase of $CePO_4$ and thus, not interacting with the Ce^{3+} ion but with the oxygen atoms constituting the channels, that is, with the phosphate groups. This fact could denote the presence of two types of water interactions in the solid CeP400, corresponding to the bound water and the water located on the channels. Broad bands at 3219 cm^{-1} and 3500 cm^{-1} correspond to the symmetric and asymmetric stretching modes of the OH groups (v_sOH and $v_{as}OH$) belonging to the H_2O molecule. The intensity of these contributions decreases as temperature increases, according to the loss of water in the solid, but remaining even at 350 °C. The band at 5138 cm^{-1} confirms the presence of molecular water in the solid CeP400. Nevertheless, as the temperature increases, a contribution at 5262 cm^{-1} is visible, remaining until 350 °C as occurring with the band at 1583 cm^{-1}. Consequently, this band is attributed to the molecular water located on the rhabdophane-type phase channels. Simultaneously, the addition of water provokes changes in the overtones and combination bands of PO_4^{3-} groups, which suggests that the H_2O molecules interacts with the phosphate groups of the structure, in line with the conclusion derived from the evaluation of the δ(H-O-H) frequency value.

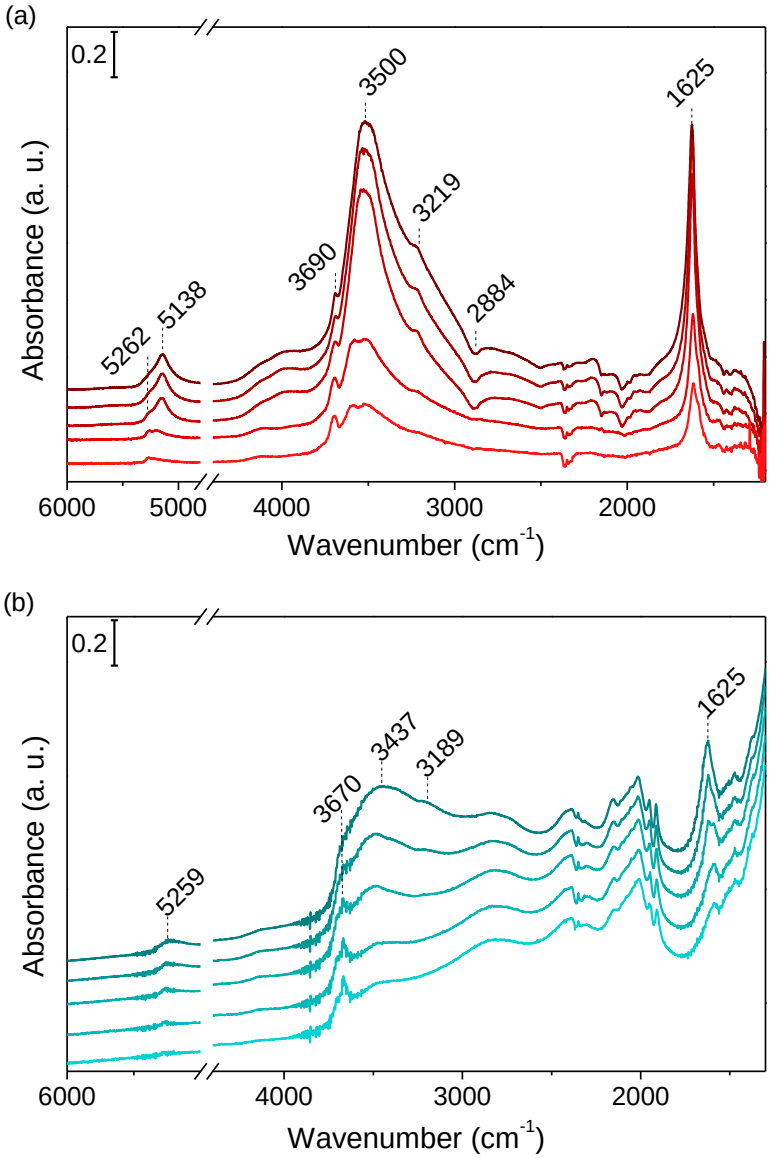

Figure 4.6. Difference spectra of (a) CeP400 and (b) CeP600 during water adsorption under 10% H_2O/Ar flow from 150 °C (top) to 350 °C (bottom)

Regarding the CeP600 spectrum, Figure 4.6 (b), the band at 1625 cm^{-1} is also observed, but not that at low frequency observed in CeP400, which confirms the absence of channels in this structure and consequently, the existence of only one type of interaction with water. Bands at 3189 and 3437 cm^{-1} correspond to the symmetric and asymmetric stretching modes of the OH groups (v_sOH and v_{as}OH) of bounded molecular water, and a band at 5259 cm^{-1} corresponding to the water overtones is observed, pointing out the presence of molecular water, as in the case of the CeP400 support. As the temperature increases, the intensity of such bands decreases, particularly from 250 °C. At this temperature, the CeP400 support is able to retain a significant amount of water in its structure, contrary to what is observed for CeP600. The differences

between CeP400 and CeP600 spectra expose the differences regarding water interaction between the two supports. Although the intensity of these water-related bands is significantly greater in the CeP400 spectrum, CeP600 allows also the inclusion of water in its structure. This fact has been explained by other authors, as previously described in Chapter III, through the formation of a continuous layer or even multilayers of adsorbed water on the monazite-type structure [39]. According to these results, $CePO_4$ supports are not responsible for the activation of water molecules in the WGS reaction, since the species observed by DRIFT spectroscopy corresponds to molecular water. Therefore, supports act as water suppliers, increasing the number of available species to be dissociated on the Pt particles. These results are consistent with the presence of only Ce^{3+} in the supports as confirmed by XPS in Chapter III. The absence of the Ce^{3+}/Ce^{4+} redox pair could inhibit the formation of oxygen vacancies and, consequently, their interaction with the water molecules, ruling out the WGS redox mechanism [12] in these solids. This conclusion results of great importance, since it allows to separate the contributions of the supports and the active phase to the behavior of water. Thus, the role of the $CePO_4$ supports is not the activation of the water molecule but the continuous supplying of water during the reaction.

In order to compare the hydrophilicity of both CeP400 and CeP600 supports, the relative intensities of the bands at 1625 cm^{-1} and 5100-5200 cm^{-1} were plotted as a function of the adsorption temperature. The results are displayed in Figure 4.7. The values of the relative intensity of the water-related bands indicate that the CeP400 support with the rhabdophane-type structure presents a superior water storage capacity to the monazite-type CeP600 in the whole temperature range studied. The intensity of both bands decreases linearly until 250 °C for CeP400. Above this temperature, the band intensity undergoes a significant drop, pointing out the influence of the operation temperature on water availability in the rhabdophane-type structure. However, the CeP600 support presents lower adsorption capacity, which decreases linearly when temperature increases. This fact is related to the different crystallographic structures of both supports, confirming that the presence of structural channels on the rhabdophane-type phase favors the availability of water in the temperature range evaluated. This result is in agreement with the catalytic activity trend followed by the Pt catalysts in the WGS reaction, where the catalytic performance of the Pt/CeP400 catalyst exceeds that of the solid Pt/CeP600 under both reaction

feeds. However, in the absence of reaction products (feed A) the catalytic activity of both solids becomes equal at 270 °C, as a consequence of the lower degree of water interaction with the CeP400 support above 250 °C.

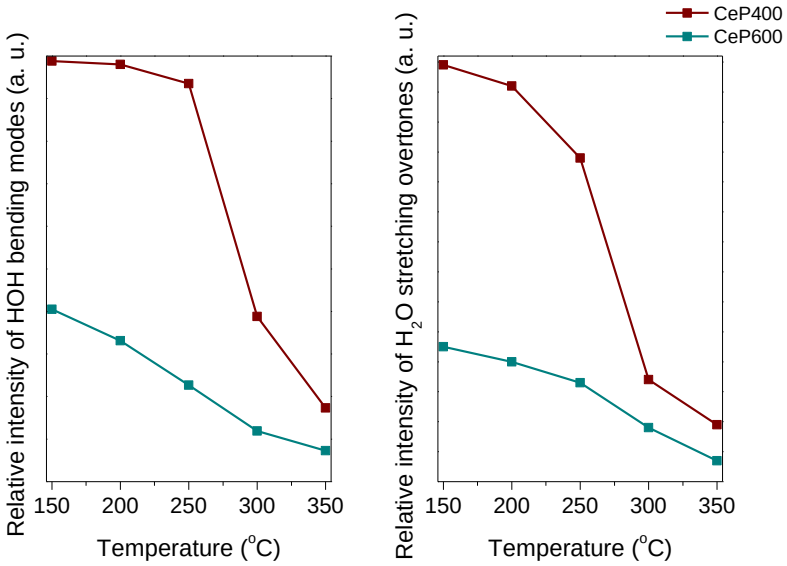

Figure 4.7. Relative intensity of the bands corresponding to the HOH bending modes (1625 cm^{-1}) and H_2O stretching overtones (5138 and 5259 cm^{-1}) in the CeP400 and CeP600 DRIFT spectra as a function of temperature during water adsorption experiments (10% H_2O/Ar)

4.4.2. Pt catalysts

The adsorption of 10% H_2O/Ar in the corresponding Pt catalysts produces no changes as for the water-related bands, as shown in Figure 4.8. However, a broad contribution at *ca.* 2000 cm^{-1} appears in the spectra of both catalysts (highlighted in the figures).

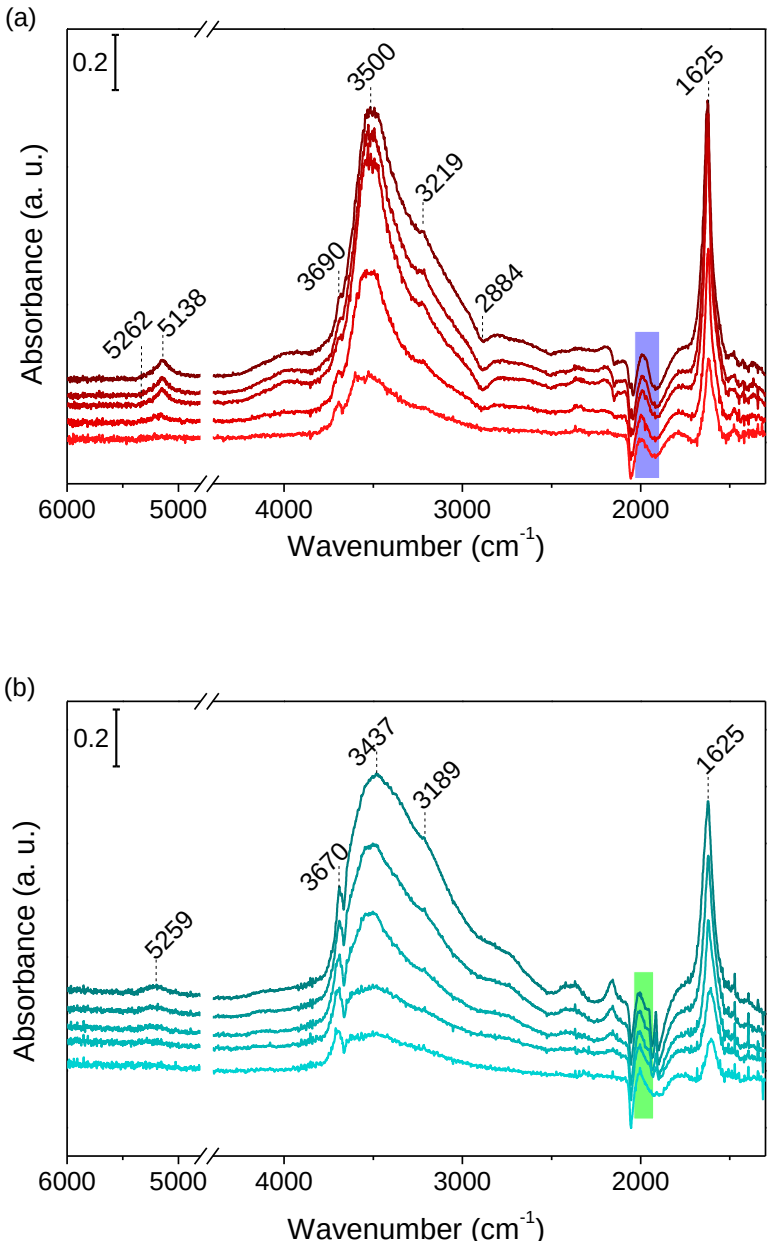

Figure 4.8. Difference spectra of (a) Pt/CeP400 and (b) Pt/CeP600 during water adsorption under 10% H_2O/Ar flow from 150 °C (top) to 350 °C (bottom)

In order to elucidate the changes in this region with respect to the corresponding supports, the catalysts spectra were subtracted to the supports spectra at each reaction temperature. The results are displayed in Figure 4.9.

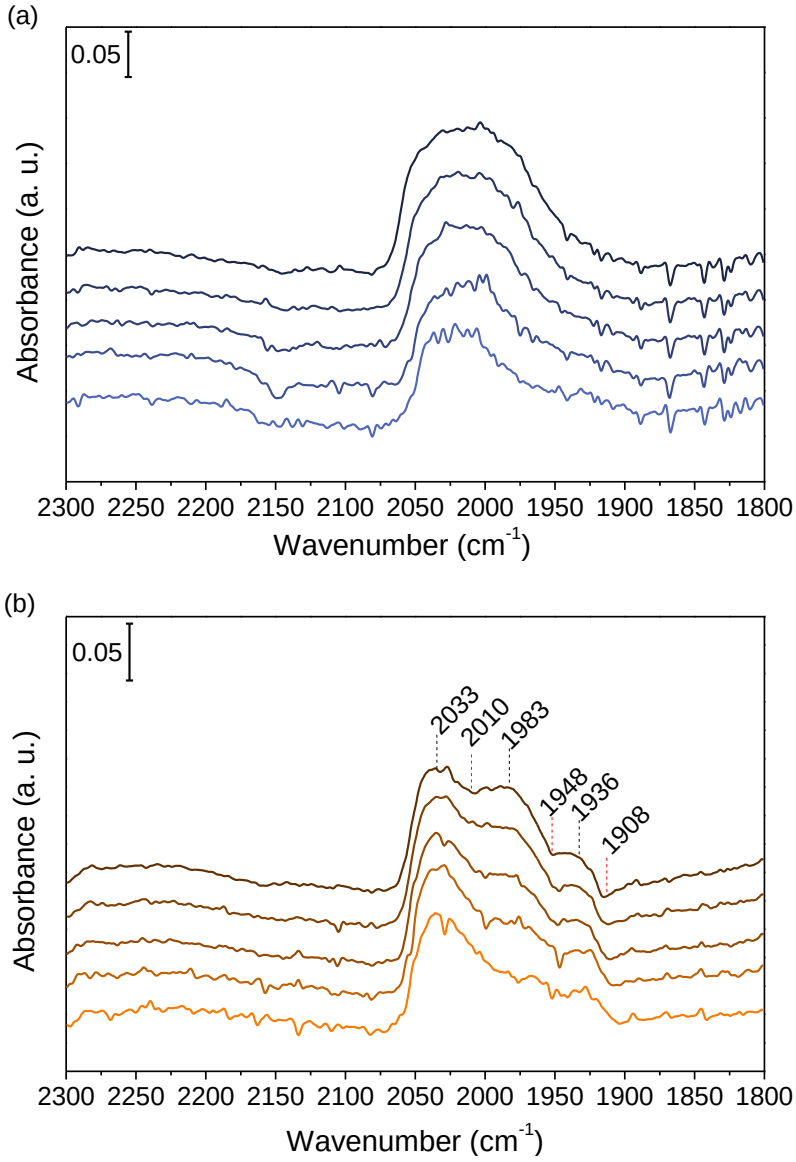

Figure 4.9. Difference spectra of (a) Pt/CeP400 and (b) Pt/CeP600 during water adsorption from 150 °C (top) to 350 °C (bottom), taking the spectra of the corresponding supports as reference

For both catalysts, differences are observed in the phosphate overtones and combination bands compared to the supports, suggesting changes in the interaction of the phosphate groups with the water molecule. Although no conclusions can be drawn from the differences between Pt/CeP400 and CeP400, since only a broad contribution is observed, the difference spectra of Pt/CeP600 taking CeP600 spectra as reference shows that the overtones and combination bands of the phosphate groups are shifted in every case towards higher wavenumbers, indicating a weakening of the bond compared to the CeP600 support in the presence of water. This is probably due to the presence of Pt, which is known to present the capacity of adsorbing water [40-43];

consequently, if Pt is interacting with water, the coordination of water to the phosphate groups could be influenced. Since bands corresponding to water adsorbed on Pt occurs in the same region than that of water adsorbed on the support, which presents broad features, it is not possible to differentiate both the contributions due to the metal phase and the support. By the same token, no OH groups derived from the dissociation of the water molecule on the Pt particles were observed. Some authors [42] have reported that the stretching vibration of OH groups bonded to Pt saturates at high water coverages, which could explain the absence of this band during the performed water adsorption experiments. Since the supports have demonstrated to retain water in its molecular form, the possible water dissociation would take place on the Pt particles, as suggested previously.

4.5. *Operando* DRIFTS study of the WGS reaction

4.5.1. $CePO_4$ supports

Difference spectra in the presence of the reaction mixture (4% CO + 10% H_2O /Ar) of both supports are shown in Figure 4.10. Both spectra present the same contributions than those observed under 10% H_2O/Ar flow. No bands corresponding to the CO possible intermediates (carbonates, bicarbonates and/or formates) appear, indicating that the supports are not able to interact with the CO molecule in the WGS temperature range. Accordingly, no CO_2 was detected at the cell oulet, which confirms the impossibility of both CeP400 and CeP600 supports to perform the WGS reaction in the absence of the metal phase. These results are in good agreement with those obtained during the WGS catalytic tests, where no CO conversion was observed for the supports in the absence of Pt.

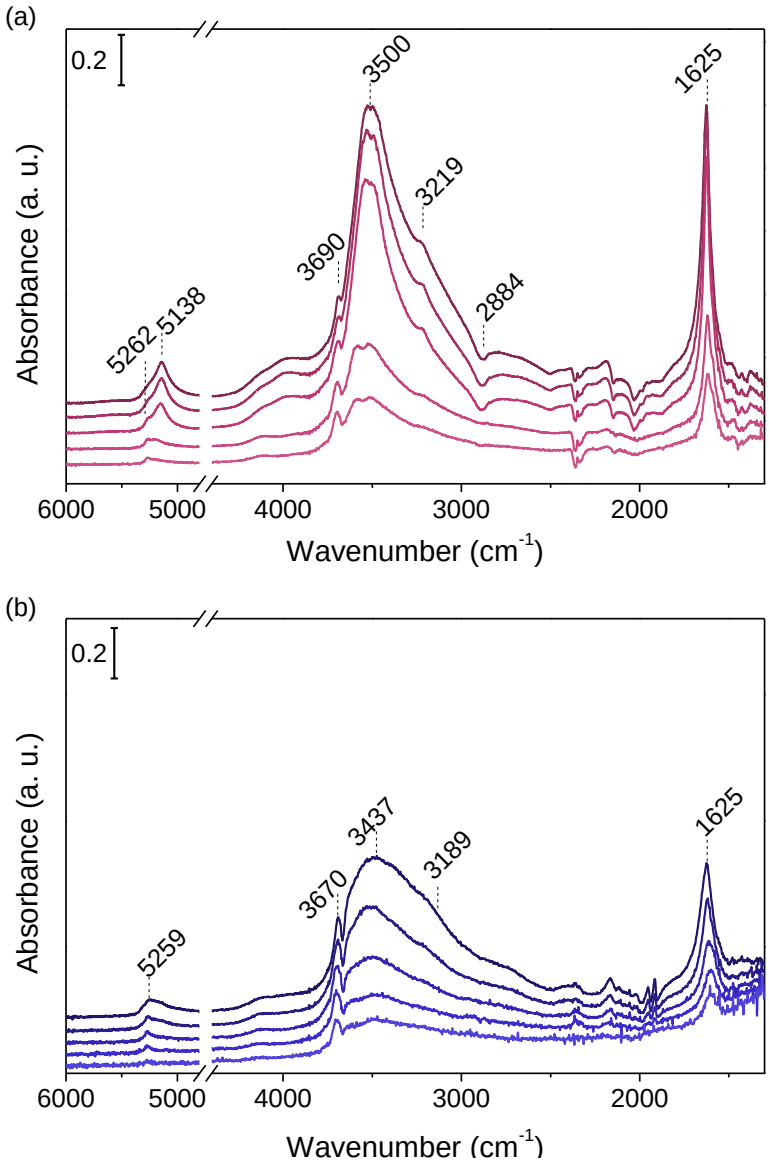

Figure 4.10. Difference spectra of (a) CeP400 and (b) CeP600 under WGS reaction flow, from 150 (top) to 350 °C (bottom)

4.5.2. Pt catalysts

Difference spectra of the Pt/CeP400 catalyst when subjected to the reaction mixture (4% CO/10% H_2O/Ar) are shown in Figure 4.11. Results reveal the presence of adsorbed water as observed in the previous experiments, in agreement with the appearance of bands at 1625 cm^{-1} and those in the 3100-3500 and 5100-5300 cm^{-1} range.

Additionally, bands corresponding to linear-bonded CO, generally found between 2000-2100 cm^{-1}, appear at 2055, 2073 and 2080 cm^{-1}, as shown in Figure 4.11 (b). The presence of these contributions exposes different environments of the Pt particles in the Pt/CeP400 solid. The shifts

of the CO stretching frequency could be explained by several reasons, as dipole-dipole interactions, changes in the Pt exposed faces or changes in the electron density of the metal particles induced by the support, which affects the number of available electrons for back-bonding to the CO π* orbitals [44, 45]. When CO is linearly adsorbed to Pt^0, a π-bond is predominantly formed, and the absorption band appears at *ca*. 2080 cm^{-1}. However, the co-adsorption of H_2O has demonstrated to shift the Pt^0-CO band to lower frequencies, being this shift associated to an increase of the back π-donation of electrons [46], which could explain the appearance of the bands at 2073 and 2055 cm^{-1}. Nevertheless, this assignment should be assumed carefully, since PO_4^{3-} overtones and combination bands appear also in this spectral range and could obscure the Pt-CO contributions. An additional band at very low frequency (1965 cm^{-1}) is also observed, which have been tentatively attributed to CO linearly adsorbed to the Pt species occluded in the channels of the rhabdophane-type phase. The CeP400 channels are constituted by oxygen atoms which present local negative charge, being able to donate electron density to the adjacent Pt atoms. Thus, the increased Pt electron density could provoke an increased bonding to the CO π* orbitals, decreasing the CO stretching frequency. This result is in accordance with previous works, where a contribution at *ca.* 1970 cm^{-1} has been observed in the spectra of Pt catalysts supported on zeolites, being attributed to CO linearly adsorbed on Pt located on the zeolite cages [44, 45]. In addition, a broad band centered at about 1800 cm^{-1} could correspond to bridge-bonded CO species, although it is too broad to be firmly assigned.

As a consequence of the interaction between the reactants, intermediate species are formed, according to the contributions emerging at 1370, 1381, 1589 and 2850 cm^{-1} (Figure 4.11 (c)). These features seem to indicate the formation of formate ($HCOO^-$) species. The bands at 1589 and 1370 cm^{-1} have been assigned to the asymmetric and symmetric OCO stretching vibrations (ν_{as} OCO and ν_s OCO), respectively, whereas the bands at 2850 and 1370 cm^{-1} have been attributed to the CH stretching (νCH) and CH bending (δCH) vibrations, respectively. In the presence of CO, formate species are known to be formed by interaction of the CO molecule with OH groups. Considering that the band corresponding to the structural OH groups of the support structure do not suffer any modification with respect to the water adsorption experiments spectra, it could be concluded that the OH participating in the formate generation are those produced by the dissociation of the water molecule on the Pt particles. Nevertheless, the observation of Pt-OH

groups results difficult in the presence of H_2O, since they appear in the 3600-3400 cm^{-1} range, where the broad contributions ascribed to OH groups of bonded water are also present, thus obscuring this region [47]. In order to identify the type of coordination of the formate species, a general procedure consists on the evaluation of the splitting between the OCO asymmetric and symmetric stretching modes, $\Delta\nu_{as\text{-}s}$ [48-50]. In this case, the splitting is not representative of the typical coordination structures described for surface formate species. This could be explained by the formation of hydrogen bonds, since fields due to water molecules can affect the splitting value [50, 51], or to an unknown type of coordination of this specie. Nevertheless, the explanation of the emerging bands could be also associated to the formation of carboxyl (COOH) intermediates. The band at 1589 cm^{-1} could be attributed to the C=O stretch, ν(C=O), whereas the doublet constituted by the 1381 and 1370 cm^{-1} features could correspond to the C-O stretching mode ν(C-O) and the OH in-plane bending vibration δ(OH), which are known to appear usually strongly coupled, as previously observed for carboxylic acids [52, 53]. Additionally, the sharp band at 2850 cm^{-1} could be ascribed to the OH stretching frequency, ν(OH). Although the observed frequencies are similar to those of carboxylic acids in water, the considerable shift of the contribution at 1589 cm^{-1} (ν(C=O)), could be explained by the generation of hydrogen bonds in the presence of water. Previous studies demonstrated that the frequency of ν(C=O), generally found in the 1690-1750 cm^{-1} range, decreases as a consequence of the H-bond formation [54]. In a similar way, the frequency of the free ν(OH) mode, found at about 3500 cm^{-1} in carboxylic acids, decrease even until 1400 cm^{-1}, depending on the strength of the hydrogen-bonding, which additionally induces changes in the intensity, breadth and structure of the OH stretching absorption band [52]. This could be the origin of the band at 2850 cm^{-1} in the Pt/CeP400 spectra. Finally, the shift of the δ(OH) mode is expected at around 1100 cm^{-1}. However, the interaction of OH groups with bases like CO, provokes the shift of this contribution towards higher wavenumbers, being observed at 1350 ± 50 cm^{-1} in the presence of water [52, 55]. This carboxyl-mediated mechanism has been previously proposed in Ni-Cu/CeO_2 catalysts [56] and Cu catalysts based on density functional theory (DFT) calculations [14, 19]. First principle calculations point out the predominance of the carboxyl beyond the formate-mediated path, since formation of the carboxyl intermediate proceeds in one step, being more favorable energetically compared to the formate generation, which requires two steps. However, the carboxyl intermediate is so reactive that its identification

by IR spectroscopy becomes a challenge [14]. Thus, it seems more reasonable to accept the associative formate-mediated mechanism in the Pt/CeP400 solid. Nevertheless, a reliable assignment of the observed bands could be developed through the use of isotopically labelled molecules.

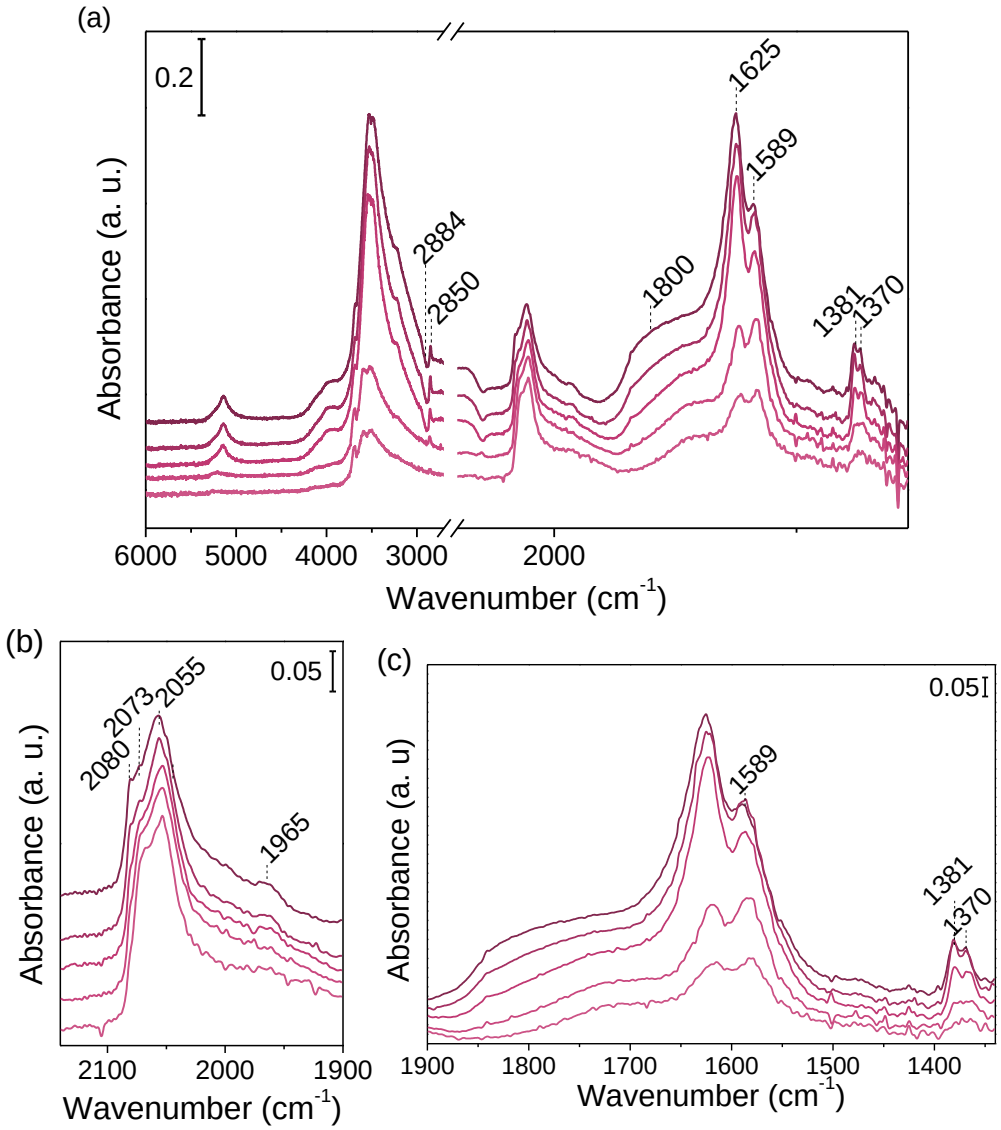

Figure 4.11. (a) Difference spectra (general) of the Pt/CeP400 catalyst under WGS reaction flow, and enlargement of (b) 2200-1900 cm^{-1} and (c) 1900-1340 cm^{-1} range, from 150 (top) to 350 °C (bottom)

Difference spectra of the Pt/CeP600 catalyst is shown in Figure 4.12. As for the Pt/CeP400 catalyst, bands ascribed to adsorbed water at 1622 cm^{-1} and in the 3100-3500 cm^{-1} and 5100-5300 cm^{-1} regions appear (Figure 4.12 (a)), although their intensity are lower than those of the

Pt/CeP400 catalysts, in accordance with the lowest water adsorption capacity of the support CeP600.

Bands attributed to linear Pt^0-CO are observed in the 2000-2100 cm^{-1} range (Figure 4.12 (b)). Differently from the Pt/CeP400 solid, only two bands are observed, pointing out the lower number of coordination environments of the Pt particles in Pt/CeP600, which seems reasonable due to the absence of structural channels in the CeP600 support. Furthermore, the band at 1965 cm^{-1} present in the Pt/CeP400 spectra is not observed in this catalyst, reinforcing the assignment of this contribution to Pt particles located in the rhabdophane-type phase structural channels. However, a band at 1916 cm^{-1} appears whereas another one disappears at 1949 cm^{-1}, thus it is attributed to a shift of the band corresponding to the overtone or combination mode of the phosphate group.

As in Pt/CeP400, bands corresponding to formate groups appear at 1339, 1379, 1588 and 2843 cm^{-1}, Figure 4.12 (c). The contributions at 1588 and 1339 cm^{-1} have been attributed to the asymmetric and symmetric stretching vibrations of the OCO group (ν_{as} OCO) and ν_s OCO), whereas the bands at 2843 and 1379 cm^{-1} have been ascribed to the CH stretching (νCH) and CH bending (δCH) vibrations. Considering the asymmetry of the band at 1588 cm^{-1}, it could be possible to consider that another contribution is present. In addition, several weak bands could be contained in the 1300-1400 cm^{-1} region. Both facts could indicate the formation of a second type of formate species, but the spectral resolution in the 1300-1400 cm^{-1} range does not allow to confirm it. Finally, the weak band observed at 1477 cm^{-1} could indicate the simultaneous formation of carbonate species, although they are produced in a smaller quantity, suggesting that they act as spectator species, being formate species the reaction intermediate in the Pt/CeP600 solid. Nevertheless, the availability of water seems to be related to the intermediate formed. Since formate generation implies the reaction of CO with OH groups coming from the dissociation of the water molecule, the lower water availability of the Pt/CeP600 catalyst could explain the lower formation of OH groups in this catalyst and, consequently, the additional formation of carbonate species coming from the reaction of CO with the oxygen atoms of the support.

According to the reported results, the WGS reaction in both catalysts seem to proceed *via* an associative mechanism through the generation of formate species.

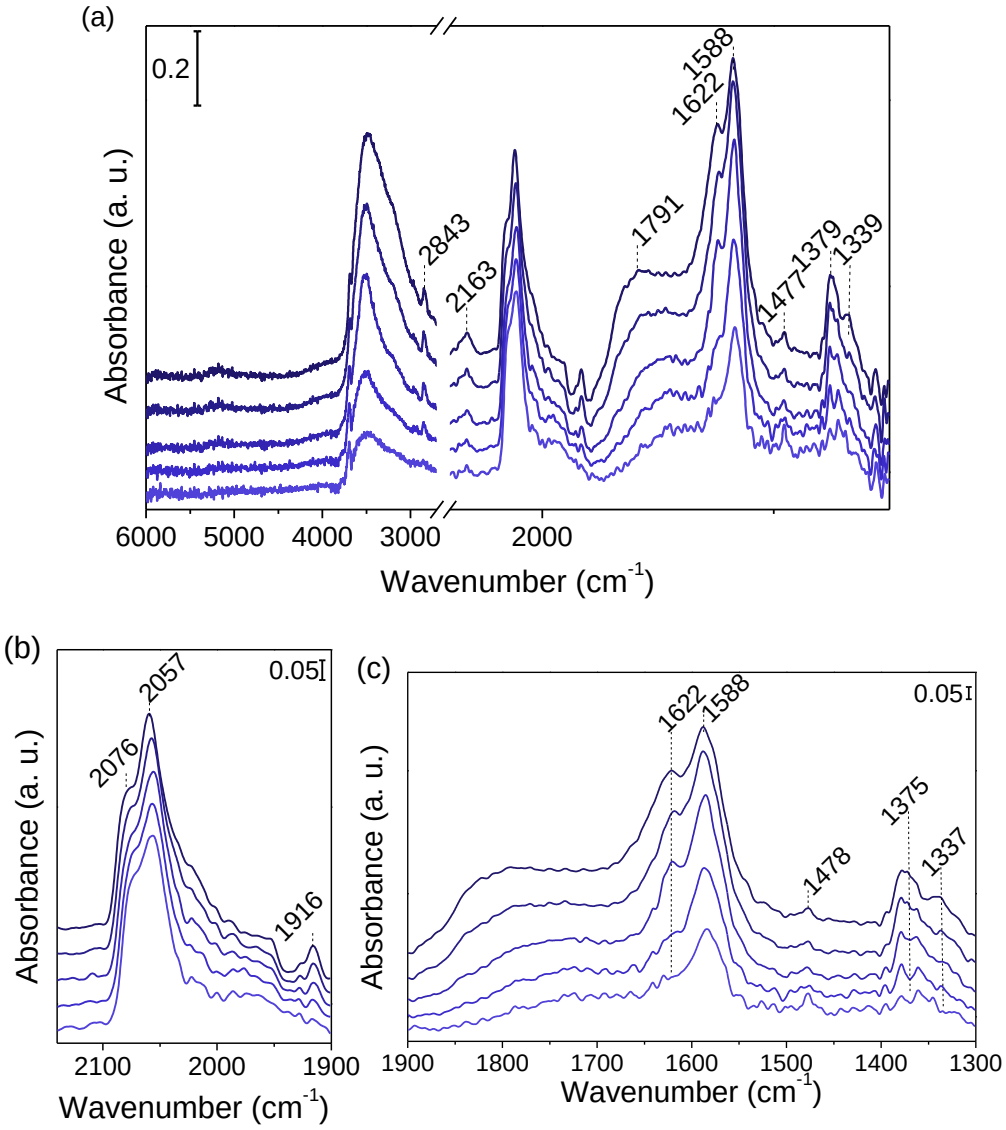

Figure 4.12. (a) Difference spectra (general) of the Pt/CeP600 catalyst under WGS reaction flow, and enlargement of (b) 2200-1900 cm^{-1} and (c) 1900-1300 cm^{-1} range, from 150 (top) to 350 °C (bottom)

DRIFTS experiments were performed in both catalysts during 3 WGS cycles, and no formation of new bands was observed. The volumetric percent of produced CO_2 was monitored using a CO_2 detector, and the results are shown in Figure 4.13. Despite the differences between the operating conditions during the catalytic activity tests and the DRIFTS experiments, the catalytic performance of the Pt/CeP400 catalyst exceed that of the Pt/CeP600 during all the temperature range evaluated. These results are in agreement with the catalytic tests previously shown.

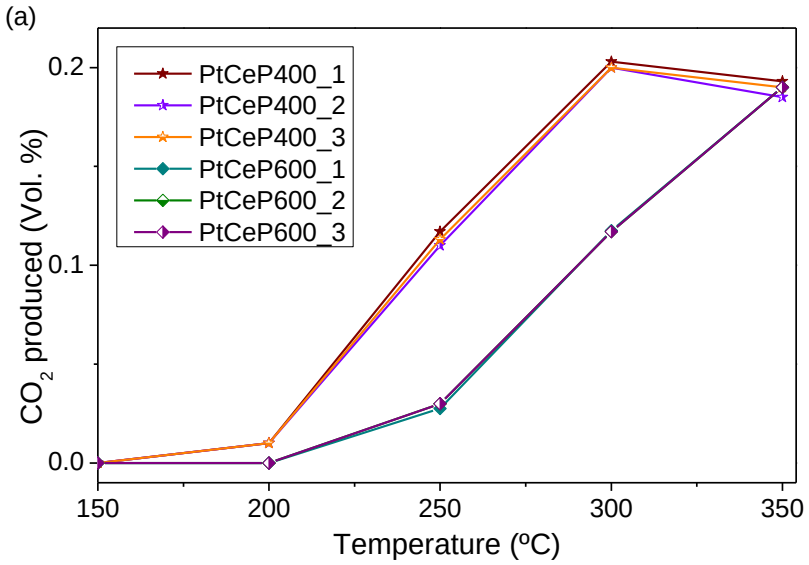

Figure 4.13. Volumetric percentage of CO_2 at the exit of the DRIFTS cell as a function of the reaction temperature

4.6. Partial conclusions

The catalytic performance of the prepared $CePO_4$-based catalytic systems has been evaluated both in the absence and in the presence of CO_2 and H_2. $CePO_4$ supports present no activity towards the WGS reaction, whereas both Pt catalysts have demonstrated to be highly active and selective, not being detected CH_4 in all the temperature range evaluated. Nevertheless, the Pt/CeP400 catalyst exceeds the catalytic activity of the Pt/CeP600 system in any reaction conditions. The apparent activation energies ($E_{a\ app}$) values are similar to those reported for the dissociation of water on Pt, suggesting that the Pt particles could be responsible for the activation of the water molecule, and not the $CePO_4$ supports.

In order to elucidate the influence of the water interaction with supports and catalysts, water adsorption experiments (10% H_2O/Ar) followed by DRIFTS have been performed. Results obtained for the supports have pointed out that both supports adsorb molecular water, not presenting the ability of dissociating it, according to the absence of new OH groups. Furthermore, the greater water affinity of the support CeP400 with respect to CeP600 is highlighted. When water adsorption experiments are performed on the catalysts, the overtones and combinational bands of the supports phosphate groups suffer modifications, suggesting that the presence of Pt

influences the water adsorption, which seems reasonable taking into account the ability of adsorbing water of Pt.

Finally, supports and Pt catalysts have been subjected to DRIFTS experiments in the presence of the WGS reaction mixture (3% CO/ 10% H_2O/ Ar). Supports spectra present no significant differences compared to those during water adsorption experiments. Furthermore, no CO_2 was detected at the cell exit, confirming that the WGS reaction does not take place on the supports in the absence of Pt. This result confirms that obtained during the WGS catalytic tests. Differently, when the Pt catalysts are subjected to the reaction mixture, formate-intermediate species are formed. Since no creation of new OH groups is observed, these species are formed through the reaction of CO with those OH groups coming from the dissociation of the water molecule. Thus, only formate species are observed in the Pt/CeP400 spectra, due to the great capacity of this catalytic system to retain water. Considering that the CeP600 support presents lower water adsorption capacity than the CeP400 one, less Pt-OH groups are generated in the Pt/CeP600 surface and a small quantity of carbonate species are also observed, suggesting that they act as spectator species. These results demonstrate that the WGS reaction in these solids take place through an associative formate-mediated mechanism.

4.7. References

1. Zugic, B., et al., *Probing the low-temperature water-gas shift activity of alkali-promoted platinum catalysts stabilized on carbon supports.* Journal of the American Chemical Society, 2014. **136**(8): p. 3238-45.

2. Pal, D.B. and R. Prasad, *Study of Water Gas Shift Reaction: Water Gas Shift Reaction in Medium Temperature Range*. 2014: LAP LAMBERT Academic Publishing.

3. Kim, Y.H., et al., *Selective CO removal in a H2-rich stream over supported Ru catalysts for the polymer electrolyte membrane fuel cell (PEMFC).* Applied Catalysis A: General, 2009. **366**(2): p. 363-369.

4. Grenoble, D.C., M.M. Estadt, and D.F. Ollis, *The Chemistry and Catalysis of the Water Gas Shift Reaction.* Journal of Catalysis, 1981. **67**: p. 90-102.

5. González-Castaño, M., et al., *Structuring Pt/CeO2/Al2O3 WGS catalyst: Introduction of buffer layer.* Applied Catalysis B: Environmental, 2017. **200**: p. 420-427.

6. García-Moncada, N., et al., *New concept for old reaction: Novel WGS catalyst design.* Applied Catalysis B: Environmental, 2018. **238**: p. 1-5.

7. Ratnasamy, C. and J.P. Wagner, *Water Gas Shift Catalysis.* Catalysis Reviews, 2009. **51**(3): p. 325-440.

8. Pal, D.B., et al., *Performance of water gas shift reaction catalysts: A review.* Renewable and Sustainable Energy Reviews, 2018. **93**: p. 549-565.

9. Trimm, D.L. and Z.I. Önsan, *Onboard Fuel Conversion for Hydrogen-Fuel-Cell-Driven Vehicles.* Catalysis Reviews, 2001. **43**(1-2): p. 31-84.

10. Jain, R., et al., *Comparative study for low temperature water-gas shift reaction on Pt/ceria catalysts: Role of different ceria supports.* Applied Catalysis A: General, 2015. **507**: p. 1-13.

11. Thinon, O., et al., *Kinetics and Mechanism of the Water–Gas Shift Reaction Over Platinum Supported Catalysts.* Topics in Catalysis, 2009. **52**(13-20): p. 1940-1945.

12. Vecchietti, J., et al., *Understanding the Role of Oxygen Vacancies in the Water Gas Shift Reaction on Ceria-Supported Platinum Catalysts.* ACS Catalysis, 2014. **4**(6): p. 2088-2096.

13. Kalamaras, C.M., D.D. Dionysiou, and A.M. Efstathiou, *Mechanistic Studies of the Water–Gas Shift Reaction over Pt/CexZr1–xO2 Catalysts: The Effect of Pt Particle Size and Zr Dopant.* ACS Catalysis, 2012. **2**(12): p. 2729-2742.

14. Gokhale, A.A., J.A. Dumesic, and M. Mavrikakis, *On the mechanism of low temperature water gas shift reaction on copper.* Journal of the American Chemical Society, 2008. **130**: p. 1402-1414.

15. Choi, S., et al., *Catalytic behavior of metal catalysts in high-temperature RWGS reaction: In-situ FT-IR experiments and first-principles calculations.* Scientific Reports, 2017. **7**: p. 41207.

16. Fu, Q., H. Saltsburg, and M. Flytzani-Stephanopoulos, *Active Nonmetallic Au and Pt Species on Ceria-Based Water-Gas Shift Catalysts.* Science Reports, 2003. **301**: p. 935.

17. Olympiou, G.C., et al., *Mechanistic aspects of the water-gas shift reaction on alumina-supported noble metal catalysts: in situ DRIFTS and SSITKA-mass spectrometry studies.* Catalysis Today, 2007. **127**: p. 304-318.

18. Byron, S.R.J., M. Loganathan, and M.S. Shanthaz, *A Review of the Water Gas Shift Reaction Kinetics.* International Journal of Chemical Reactor Engineering, 2010. **8**.

19. Reddy, G.K. and P.G. Smirniotis, *Water Gas Shift Reaction: Research Developments and Applications*. 2015: Elsevier.

20. González-Castaño, M., et al., *Deep insight into Zr/Fe combination for successful Pt/CeO2/Al2O3WGS catalyst doping.* Catalysis Science & Technology, 2017. **7**(7): p. 1556-1564.

21. Rodríguez, J.A., et al., *Activity of CeOx and TiOx Nanoparticles Grown on Au(111) in the Water-Gas Shift Reaction.* Science, 2007. **318**: p. 1757-1760.

22. García-Moncada, N., et al., *A direct in situ observation of water-enhanced proton conductivity of Eu-doped ZrO2 : Effect on WGS reaction.* Applied Catalysis B: Environmental, 2018. **231**: p. 343-356.

23. Phatak, A.A., et al., *Kinetics of the water–gas shift reaction on Pt catalysts supported on alumina and ceria.* Catalysis Today, 2007. **123**(1-4): p. 224-234.

24. Pazmiño, J.H., et al., *Metallic Pt as active sites for the water–gas shift reaction on alkali-promoted supported catalysts.* Journal of Catalysis, 2012. **286**: p. 279-286.

25. Miao, D., A. Goldbach, and H. Xu, *Platinum/Apatite Water-Gas Shift Catalysts.* ACS Catalysis, 2016. **6**(2): p. 775-783.

26. Miao, D., et al., *Water-gas shift reaction over platinum/strontium apatite catalysts.* Applied Catalysis B: Environmental, 2017. **202**: p. 587-596.

27. Zhang, S., et al., *WGS catalysis and in situ studies of CoO(1-x), PtCo(n)/Co3O4, and Pt(m)Co(m')/CoO(1-x) nanorod catalysts.* Journal of the American Chemical Society, 2013. **135**(22): p. 8283-8293.

28. Gonzalez-Castaño, M., et al., *Pt vs. Au in water–gas shift reaction.* Journal of Catalysis, 2014. **314**: p. 1-9.

29. Smirniotis, P. and K. Gunugunuri, *Water Gas Shift Reaction: Research Developments and Applications*. 1st ed. 2015: Elsevier.

30. Soptrajanov, B., G. Jovanovski, and L. Pejov, *Very low H-O-H bending frequencies. III. Fourier transform infrared study of cobalt potassium phosphate monohydrate and manganese potassium phosphate monohydrate.* Journal of Molecular Structure, 2002. **613**: p. 47-54.

31. Romero-Sarria, F., et al., *CO oxidation at low temperature on Au/CePO4: Mechanistic aspects.* Applied Catalysis B: Environmental, 2011. **107**(3-4): p. 268-273.

32. Lucas, S., et al., *Rare earth phosphate powders RePO4·nH2O (Re=La, Ce or Y) II. Thermal behavior.* Journal of Solid State Chemistry, 2004. **177**(4-5): p. 1312-1320.

33. Clearfield, A. and D.S. Thakur, *Zirconium and Titanium Phosphates as Catalysts: A Review.* Applied Catalysis, 1986. **26**: p. 1-26.

34. Frost, R.L. and K.L. Erickson, *Near-infrared spectroscopic study of selected hydrated hydroxylated phosphates.* Spectrochimica Acta Part A, 2005. **61**(1-2): p. 45-50.

35. Dayanand, C., et al., *Structural investigations of phosphate glasses: a detailed infrared study of the x(PbO)-(1-x)P2O5 vitreous system.* Journal of Materials Science, 1996. **31**: p. 1945-1967.

36. Nazaraly, M., et al., *Synthesis and characterization of CeIV(PO4)(HPO4)0.5(H2O)0.5.* Journal of Physics and Chemistry of Solids, 2006. **67**(5-6): p. 1075-1078.

37. Assaaoudi, H., A. Ennaciri, and A. Rulmont, *Vibrational spectra of hydrated rare earth ortophosphates.* Vibrational Spectroscopy, 2001. **25**: p. 81-90.

38. Falk, M., *The frequency of the H-O-H bending fundamental in solids and liquids.* Spectrochimica Acta, 1984. **40A**: p. 43-48.

39. Pusztai, P., et al., *Structure-Independent Proton Transport in Cerium(III) Phosphate Nanowires.* ACS Appl Mater Interfaces, 2015. **7**(18): p. 9947-56.

40. Le, J., et al., *Theoretical insight into the vibrational spectra of metal-water interfaces from density functional theory based molecular dynamics.* Phys Chem Chem Phys, 2018. **20**(17): p. 11554-11558.

41. Hodgson, A. and S. Haq, *Water adsorption and the wetting of metal surfaces.* Surface Science Reports, 2009. **64**(9): p. 381-451.

42. Ibach, H. and S. Lehwald, *The bonding of water molecules to Platinum surfaces.* Surface Science, 1980. **91**: p. 187-197.

43. Sexton, B.A., *Vibrational spectra of water chemisorbed on Platinum (111).* Surface Science, 1980. **94**: p. 435-445.

44. Kappers, M.J. and J.H. van der Maas, *Correlation between CO frequency and Pt coordination number. A DRIFT study on supported Pt catalysts.* Catalysis Letters, 1991. **10**: p. 365-374.

45. Lane, G.S., et al., *Infrared Spectroscopy of Adsorbed Carbon Monoxide on Platinum/Nonacidic Zeolite Catalysts.* Journal of Catalysis, 1993. **141**: p. 465-477.

46. Hadjiivanov, K., *IR study of CO and H2O coadsorption on Pt^{n+}/TiO2 and Pt/TiO2 samples.* Journal of the Chemical Society, Faraday Transactions, 1998. **94**: p. 1901-1904.

47. Morrow, B.A. and P. Ramamurthy, *Infrared Spectra of Hydroxyl Groups on the Surface of Platinum.* Canadian Journal of Chemistry, 1971. **49**: p. 3409-3410.

48. Nakamoto, K., *Infrared and Raman Spectra of Inorganic and Coordination Compounds*. 2009: Wiley.

49. Oomens, J. and J.D. Steill, *Free Carboxylate Stretching Modes.* The Journal of Physical Chemistry A, 2008. **112**: p. 3281-3283.

50. Busca, G. and V. Lorenzelli, *Infrared spectroscopic identification of species arising from reactive adsorption of carbon oxides on metal oxide surfaces.* Materials Chemistry, 1982. **7**: p. 89-126.

51. Ramis, G., G. Busca, and V. Lorenzelli, *Low-temperature CO2 adsorption on metal oxides: spectroscopic characterization of some weakly adsorbed species.* Materials Chemistry and Physics, 1991. **29**: p. 425-435.

52. Novak, A., *Large Molecules. Structure and Bonding*. Vol. 18. 1974: Springer.

53. Hay, M.B. and S.C.B. Myneni, *Structural environments of carboxyl groups in natural organic molecules from terrestrial systems. Part 1: Infrared spectroscopy.* Geochimica et Cosmochimica Acta, 2007. **71**(14): p. 3518-3532.

54. Maréchal, Y., *The Hydrogen Bond and the Water Molecule: The Physics and Chemistry of Water, Aqueous and Bio Media*. 2007: Elsevier.

55. Chakarova, K. and K. Hadjiivanov, *Problems in the IR measuring the acidity of zeolite bridging hydroxyls by low-temperature CO adsorption.* Chemical Communications, 2011. **47**(6): p. 1878-1880.

56. Saw, E.T., et al., *High-temperature water gas shift reaction on Ni–Cu/CeO2 catalysts: effect of ceria nanocrystal size on carboxylate formation.* Catalysis Science & Technology, 2016. **6**(14): p. 5336-5349.

Chapter V

$^{18}O_2$ and $C^{18}O_2$ isotopic exchange experiments over $CePO_4$-based catalysts: Mechanistic implications

Abstract

Considering the importance of the presence of oxygen vacancies in WGS catalysts, this chapter presents the study of the oxygen mobility in the $CePO_4$-based materials by means of $^{18}O_2$ and $C^{18}O_2$ isotopic exchange experiments. Differences in the extent and mechanism of exchange using both molecules are discussed, as well as their influence regarding the WGS reaction mechanism. Additionally, the interaction of the molecules with the solids is analyzed through IR spectroscopy.

5.1. Introduction

Along the previous chapter, the importance of the WGS reaction mechanism has been highlighted. The structure and specifically, the presence or not of oxygen vacancies, has demonstrated to play a substantial role regarding the WGS reaction mechanism in oxide supports [1-5]. Consequently, studying the mobility of the oxygen atoms contained in the solids becomes of great interest in order to justify the reaction path followed by the catalysts under study. Considering that migration rates of active species are frequently much higher than the turnover frequencies of the reaction, surface species are able to migrate and interact with a great number of active sites between two consecutive catalytic cycles [6, 7]. In this context, isotopic exchange techniques using molecules containing ^{18}O provide answers to characterize the catalysts behavior regarding the mobility and reactivity of the oxygen atoms constituting the solid, as well as the elucidation of reaction mechanisms [8, 9]. Generally, the exchange reaction mechanism includes three steps [10]:

1. Adsorption and dissociation of the labelled molecule ($*X_2$) to form atoms or ions adsorbed on the surface ($*X_{ads}$).
2. Exchange of these species ($*X_{ads}$) with the atoms or ions naturally present in the surface or the bulk of the solid (X_s).
3. Desorption of the exchanged elements in their molecular form ($*X_2$, X_2 or $*XX$) in the gas phase.

Additionally, diffusion phenomena can occur if the adsorbed labelled species and those present in the solid are not in the same region of the catalyst after the labelled molecule adsorption.

The change in the gas phase composition during the exchange reaction allows to calculate characteristic parameters of the isotopic exchange as the rate of exchange, the atomic fraction of ^{18}O in the gas phase, the diffusion coefficients in the surface and bulk and the number of exchanged and exchangeable oxygen atoms in the catalyst, which are useful parameters for the knowledge of the catalytic properties of the solids.

Particularly, isotopic exchange using $^{18}O_2/^{16}O_2$ and $C^{18}O_2/C^{16}O_2$ is a powerful technique for the study of the WGS reaction. Differences in the oxygen rate of exchange depending on the labelled molecule are a consequence of a difference in the mechanism: in the case of oxygen, a

dissociative mechanism in which the rate limiting step is the dissociation of the oxygen molecule, whereas in the case of CO_2 an associative mechanism takes place, *via* formation and decomposition of intermediate species such as carbonate, hydrogen carbonate or formate species. As mentioned in Chapter IV, two possible mechanisms are generally described for the WGS reaction: the redox and the associative mechanism. In this context, the isotopic exchange experiments using $^{18}O_2$ results of great interest for evaluating the absence or presence of oxygen vacancies in the supports, which have demonstrated to play an important role in the redox mechanism [1, 11, 12]. On the other hand, the experiments using $C^{18}O_2$ allow the evaluation of the formation of carbonate-like intermediate species, implied in the WGS associative mechanism. Thus, the use of these labelled molecules could provide information about the preferred mechanism and/or the competence between them, which are crucial aspects during the WGS reaction [13-15]. According to the DRIFTS studies presented in Chapter IV, the WGS reaction mechanism in the $CePO_4$-based catalytic systems seem to proceed *via* an associative mechanism. Thus, isotopic exchange experiments could help to understand why this mechanism occurs to a greater extent in these solids.

According to the aforementioned considerations, this chapter presents the $^{18}O_2/^{16}O_2$ and $C^{18}O_2/C^{16}O_2$ isotopic exchange studies on the prepared $CePO_4$ supports and the corresponding Pt catalysts. The obtained results are correlated to the WGS reaction mechanism in these solids and, finally, the interaction of the labelled molecules with the surface of the solids is discussed based on the results obtained by transmission IR spectroscopy and mass spectrometry.

5.2. $^{18}O_2/^{16}O_2$ isotopic exchange experiments

5.2.1. Isothermal $^{18}O_2/^{16}O_2$ isotopic exchange

In order to study the presence of oxygen vacancies, the mobility of oxygen in the $CePO_4$-based solids was firstly evaluated through the use of $^{18}O_2$ in isothermal conditions. The selected temperature to carry out these experiments was 300 °C, considering the high activity of the $CePO_4$-based catalysts at this temperature.

The evolution of the O_2 isotopic distribution as a function of the time during the exchange experiment at 300 °C on the CeP400 support is presented in Figure 5.1. At this temperature, the

concentration of $^{18}O_2$ does not decrease, whereas no formation of $^{16}O^{18}O$ and/or $^{16}O_2$ is detected, indicating that the oxygen exchange is not significative in this support. Similar results were obtained for the CeP600 support and the corresponding Pt catalysts (not presented).

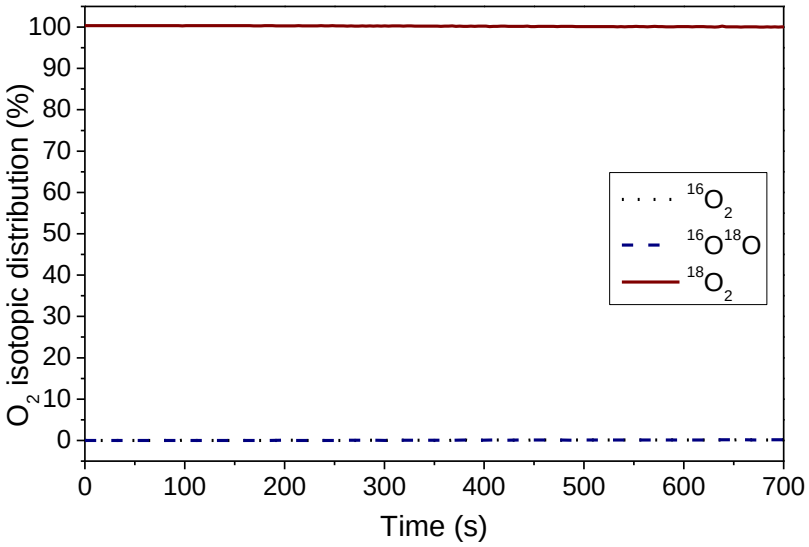

Figure 5.1. O_2 isotopic distribution (%) as a function of the time during isotopic exchange reaction at 300 °C over CeP400

5.2.2. Temperature- programmed $^{18}O_2/^{16}O_2$ isotopic exchange experiments

Since every solid presented no activity towards oxygen exchange at this temperature, temperature programmed exchange experiments were carried out to evaluate the oxygen exchange capacity as a function of the temperature.

5.2.2.1. $CePO_4$ supports

Results corresponding to the $CePO_4$ supports are displayed in Figure 5.2.

In both cases, the oxygen exchange is not significative in the temperature range of interest for the WGS reaction, that is from 200 to 350 °C. However, the solid CeP600 exchange oxygen from 400 °C, reaching a number of exchanged atoms (N_e) equal to 1.5 x 10^{21} atoms per gram of support at 600 °C, which corresponds to a 15% of the total number of atoms present in the solid. Given that the first specie detected in the gas phase is $^{16}O_2$, followed by $^{16}O^{18}O$, it can be concluded

that the exchange mechanism proceeds through a multiple mechanism, that is, with the participation of two oxygen atoms of the solid, according to:

$$^{18}O_{2(g)} + 2\ ^{16}O_{(s)} \leftrightarrow {}^{16}O_{2(g)} + 2\ ^{18}O_{(s)}$$

$$^{18}O_{2(g)} + {}^{16}O_{(s)} + {}^{18}O_{(s)} \leftrightarrow {}^{16}O^{18}O_{(g)} + 2\ ^{18}O_{(s)}$$

$$^{16}O_{2(g)} + {}^{16}O_{(s)} + {}^{18}O_{(s)} \leftrightarrow {}^{16}O^{18}O_{(g)} + 2\ ^{16}O_{(s)}$$

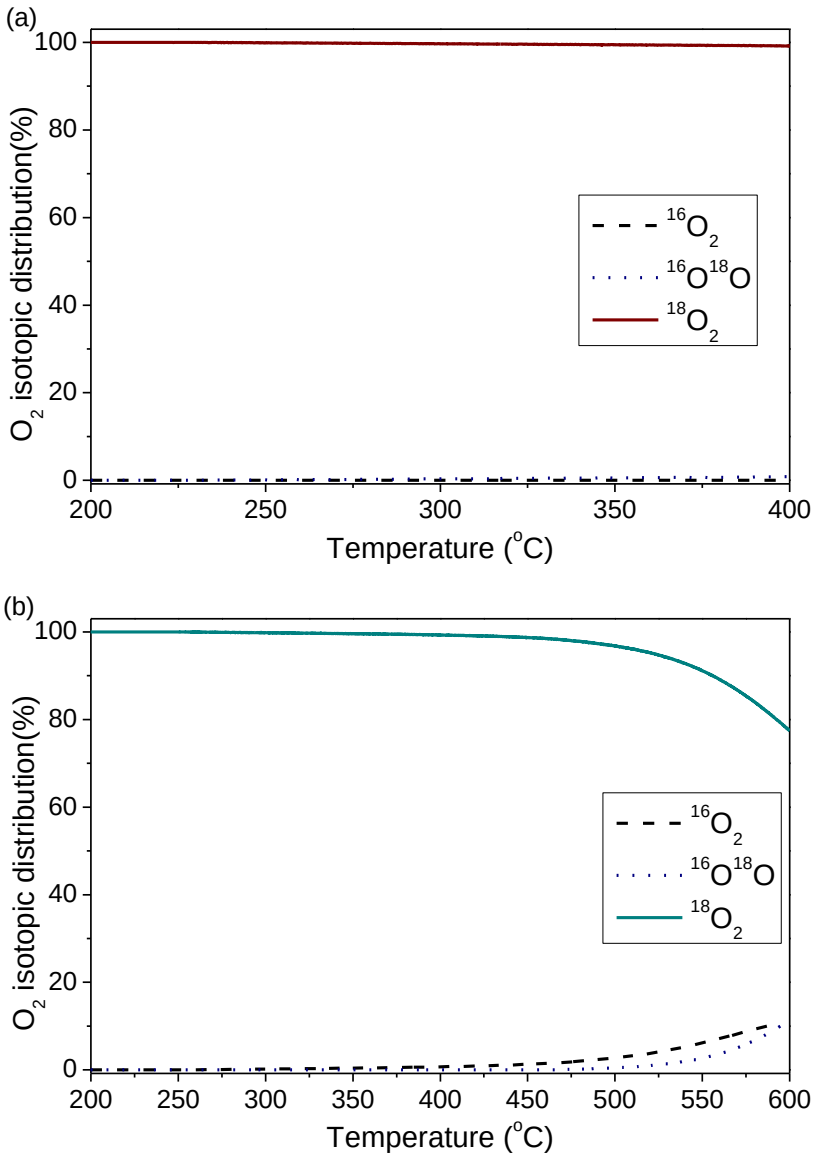

Figure 5.2. O_2 isotopic distribution (%) as a function of the temperature during temperature-programmed isotopic exchange reaction over (a) CeP400, (b) CeP600

5.2.2.2. Pt catalysts

The same experiments were performed over the corresponding Pt catalysts. Results are shown in Figure 5.3.

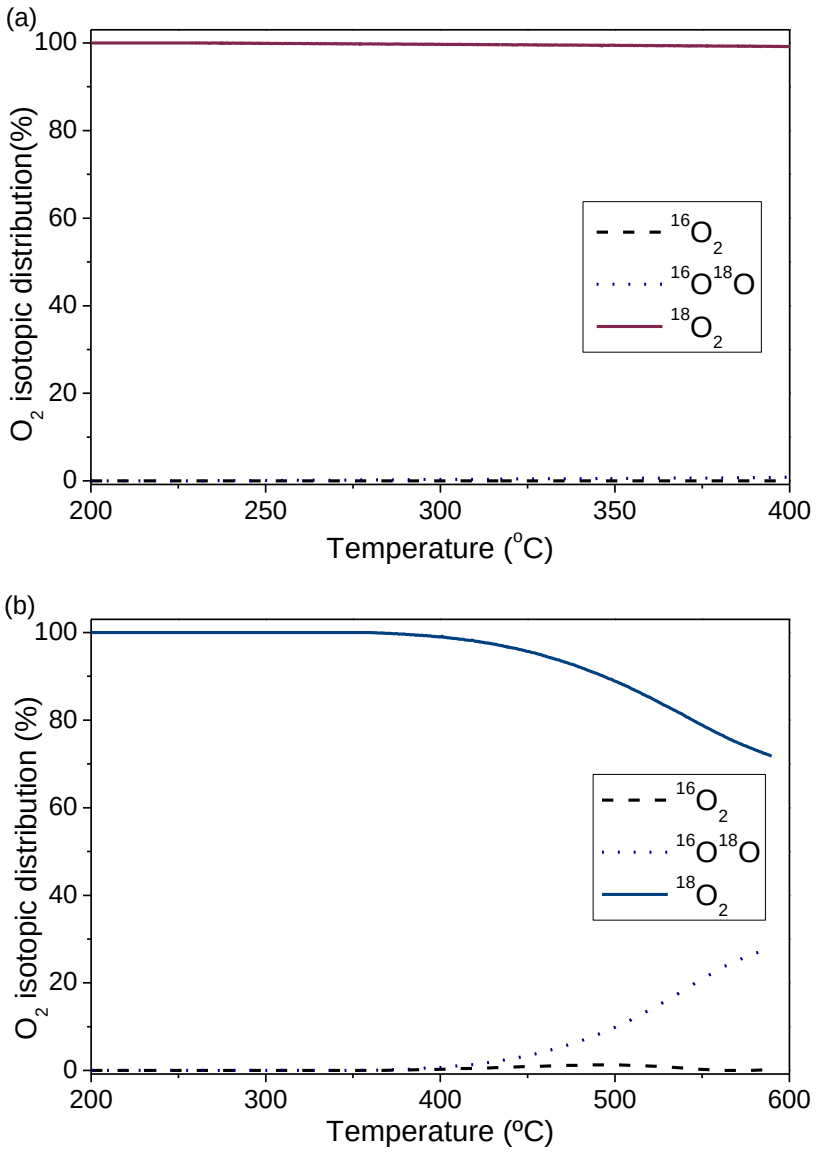

Figure 5.3. O_2 isotopic distribution (%) as a function of the temperature during temperature-programmed isotopic exchange reaction over (a) Pt/CeP400, (b) Pt/CeP600

Results obtained for the Pt/CeP400 catalyst does not show any difference with respect to the support. In the temperature range evaluated, no exchange occurs.

Regarding the Pt/CeP600 catalyst, the exchange starts at the same temperature than in the corresponding support, 400 °C. However, the number of oxygen exchanged atoms at 600 °C

corresponds to a 13% of the total oxygen atoms present in the support, thus being slightly smaller than that observed for the support. Additionally, the major specie observed during the experiment is $^{16}O^{18}O$ being the production of $^{16}O_2$ almost insignificant. This indicates that the exchange of oxygen species in the CeP600 support is influenced by the presence of Pt, presumably located in the nearby vicinity [16].

These results allow to confirm the absence of oxygen vacancies in the structure of both $CePO_4$ phases in the WGS temperature range, in good agreement with the lack of the Ce^{3+}/Ce^{4+} redox pair confirmed by means of the XPS presented in Chapter III. Since Pt does not allow to improve the exchange activity, it can be concluded that the rate limiting step in the incorporation or the mobility of oxygen atoms in the $CePO_4$ lattice. Consequently, the redox mechanism proposed for the WGS reaction, which implies the existence of oxidation-reduction cycles and the participation of the support oxygen atoms [1, 5, 17] can be discarded in this type of solids. Therefore, $^{18}O_2$ isotopic exchange results reinforce the occurrence of the associative mechanism demonstrated by DRIFTS in Chapter IV.

5.3. $C^{18}O_2/C^{16}O_2$ isotopic exchange experiments

5.3.1. $CePO_4$ supports

In view of the low activity of the $CePO_4$-based catalysts towards the oxygen exchange with $^{18}O_2$, the oxygen mobility was evaluated using $C^{18}O_2$ as labelled molecule.

Figure 5.4 shows the evolution of the CO_2 isotopic distribution at 300 °C for the $CePO_4$ supports. Results show that, contrary to what is observed in the presence of $^{18}O_2$, the oxygen exchange using $C^{18}O_2$ occurs at a high rate, giving rise to the formation of $C^{16}O^{18}O$ in the first place, followed by the generation of $C^{16}O_2$. According to these results, the mechanism of the $C^{18}O_2$ exchange reaction in both supports proceeds through two consecutive simple exchange mechanisms *via* transfer of one oxygen atom in every stage, expressed by:

$$C^{18}O_{2(g)} + {}^{16}O_{(s)} \leftrightarrow C^{16}O^{18}O_{(g)} + {}^{18}O_{(s)}$$

$$C^{16}O^{18}O_{(g)} + {}^{16}O_{(s)} \leftrightarrow C^{16}O_{2(g)} + {}^{18}O_{(s)}$$

The second stage involving the formation of $C^{16}O_2$ takes place almost instantly to the first one, which demonstrates a fast activation of CO_2 in the supports, as well as a great oxygen mobility in the bulk of the solids. Nevertheless, although the initial rate of exchange is high, long times are required to reach the equilibrium.

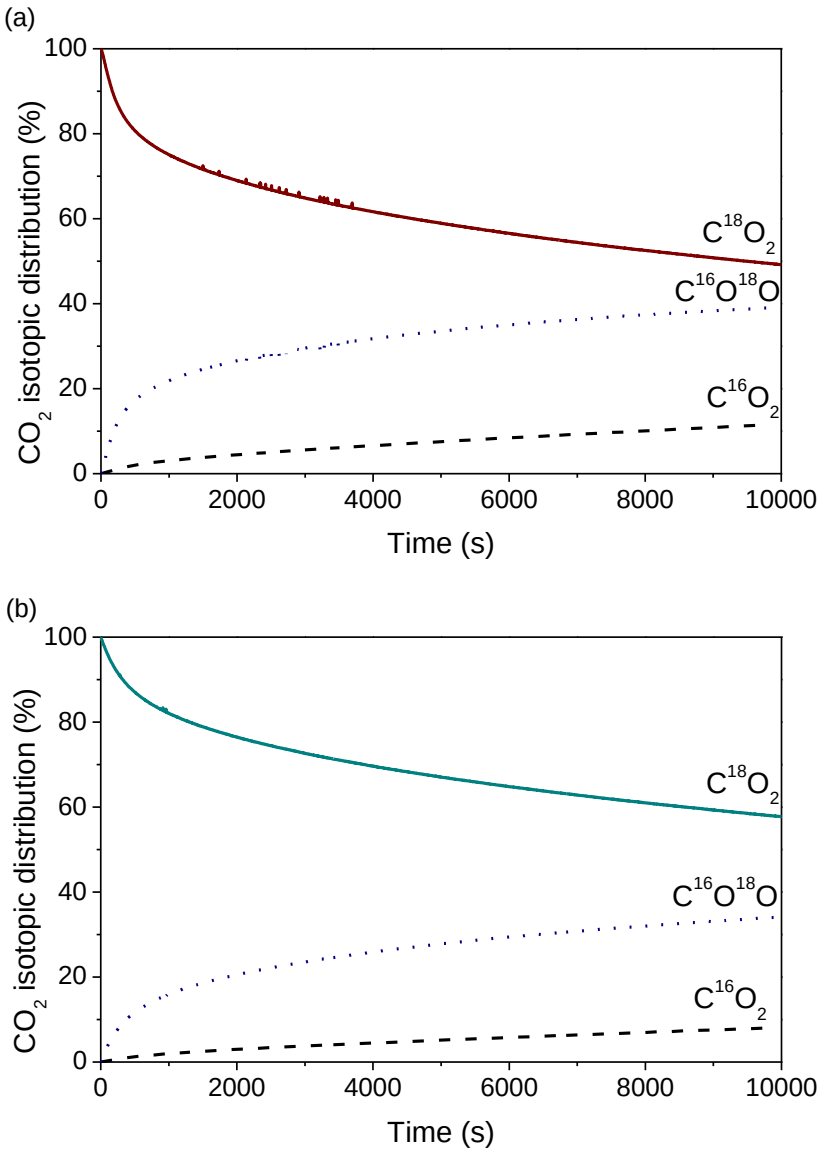

Figure 5.4. CO_2 isotopic distribution (%) as a function of the time during isotopic exchange reaction at 300 °C over (a) CeP400, (b) CeP600

In order to compare the oxygen mobility in both solids, the number of oxygen exchanged atoms of both supports (N_e) as a function of the time is shown in Figure 5.5. Additionally, N_e data after two hours of reaction and R_e are summarized in Table 5.1.

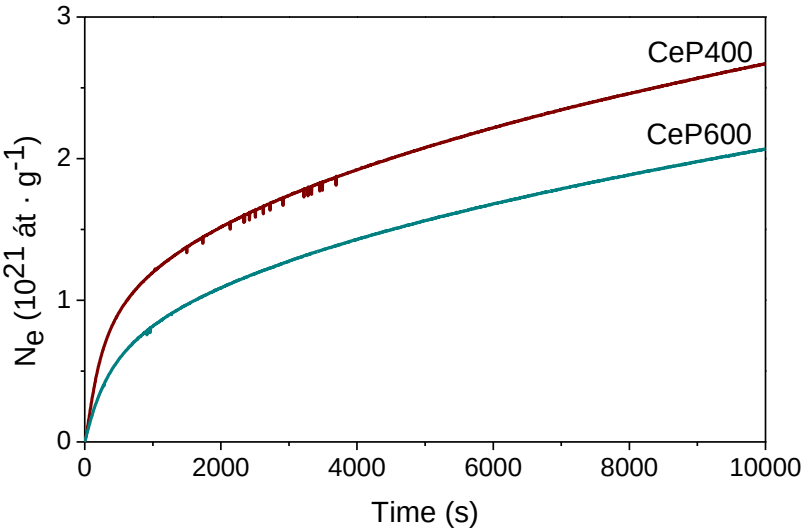

Figure 5.5. N_e evolution as a function of the time for the CeP400 and CeP600 supports

Table 5.1. Number of oxygen exchanged atoms (N_e) and $C^{18}O_2$ rates of exchange (R_e) of the $CePO_4$ supports at 300 °C

Sample	N_e (at·g^{-1})	R_e (at·g^{-1}·s^{-1})
CeP400	$2.7x10^{21}$	$4.6x10^{18}$
CeP600	$2x10^{21}$	$2.7x10^{18}$

Results demonstrate that the activation of the CO_2 molecule in the supports surface is not a limiting process, contrary to the activation of the O_2 molecule. Nevertheless, N_e and R_e values are superior for the support CeP400, indicating that the activation of CO_2 is more favorable on it than on the CeP600 support. Whereas the CeP400 support exchanges a 24% of the total atoms present in the solid, the CeP600 one exchanges a 20% of its atoms.

5.3.2. Pt catalysts

The same experiments were performed on the corresponding Pt catalysts. CO_2 isotopic distribution during the exchange reaction over the Pt/CeP400 and Pt/CeP600 catalysts is shown in Figure 5.6. As in the case of the support, the exchange occurs through two consecutive simple exchange mechanisms, implying the participation of one oxygen atom in each stage. The exchange reaction occurs also at high rate when the exchange reaction starts, being necessary long times to reach the equilibrium.

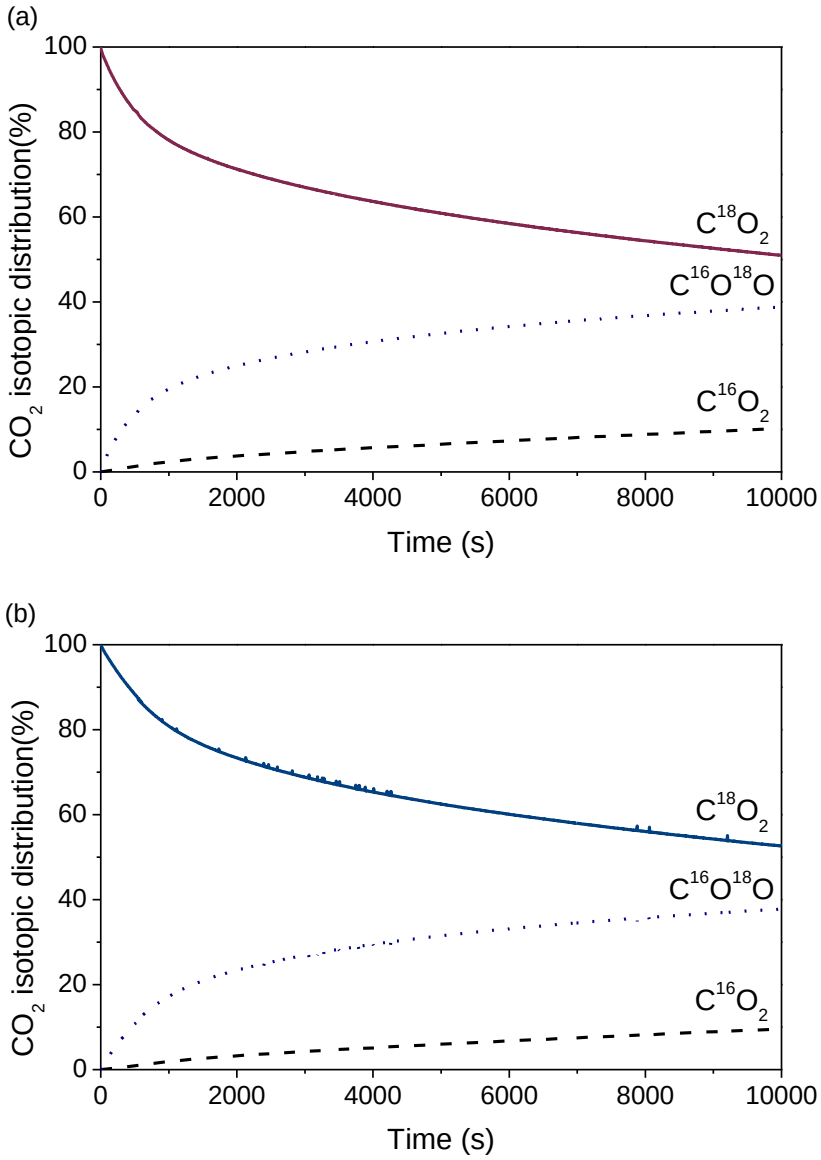

Figure 5.6. CO_2 isotopic distribution (%) as a function of the time during isotopic exchange reaction at 300 °C over (a) Pt/CeP400, (b) Pt/CeP600

Figure 5.7 shows the evolution of N_e of the Pt catalysts as a function of the time during the exchange reaction at 300 °C. In the presence of Pt, N_e becomes similar for both solids. Nevertheless, the Pt/CeP400 catalyst presents a slightly superior exchange capacity, particularly at the beginning of the reaction. According to the N_e and R_e values presented in Table 5.2, both N_e and R_e values for the Pt/CeP400 catalyst are smaller than those of the CeP400 support. Additionally, the number of oxygen exchanged atoms in Pt/CeP400 corresponds to a 21% of the total atoms present in the solid, very close to the 22% exchanged in the Pt/CeP600 catalyst.

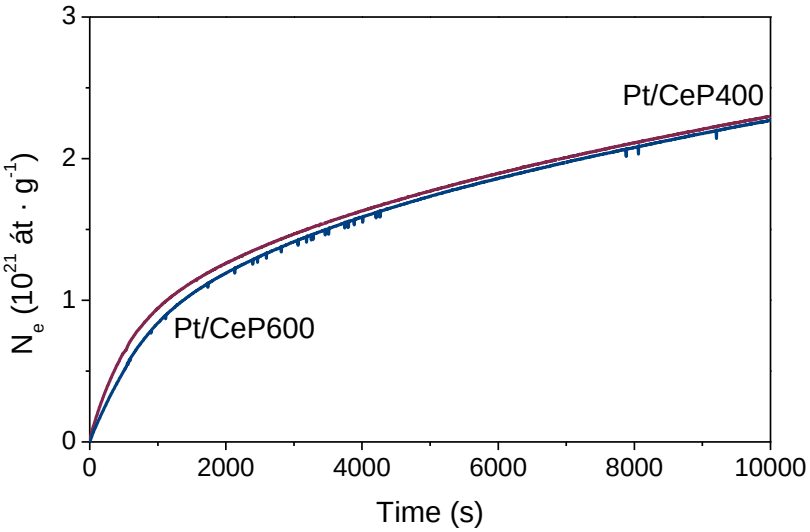

Figure 5.7. N_e evolution as a function of the time for the Pt/CeP400 and Pt/CeP600 catalysts

Table 5.2. Number of oxygen exchanged atoms (N_e) and $C^{18}O_2$ rates of exchange (R_e) of the Pt catalysts at 300 °C

Sample	N_e (at·g^{-1})	R_e (at·g^{-1}·s^{-1})
Pt/CeP400	$2.3x10^{21}$	$2.6x10^{18}$
Pt/CeP600	$2.3x10^{21}$	$2x10^{18}$

Considering that both the supports and catalysts need long times to reach the equilibrium, the calculation of the diffusion coefficient using Kakioka's model results of great interest. Linear fitting of the results and diffusion coefficient values are displayed in Figure 5.8 and Table 5.3, respectively. Diffusion coefficient of the support CeP400 is smaller than that of CeP600, which could be related with an enhanced oxygen diffusion in CeP400 as a consequence of the presence of channels in its structure. In the presence of Pt, no significant differences are observed between CeP600 and Pt/CeP600, thus denoting no influence of the metal particles during the diffusion processes. However, the diffusion coefficient of Pt/CeP400 decreases significantly with respect to CeP400. This fact could be related to the presence of Pt particles in the channels structure, which could hinder the diffusion of oxygen in the bulk of the CeP400 support.

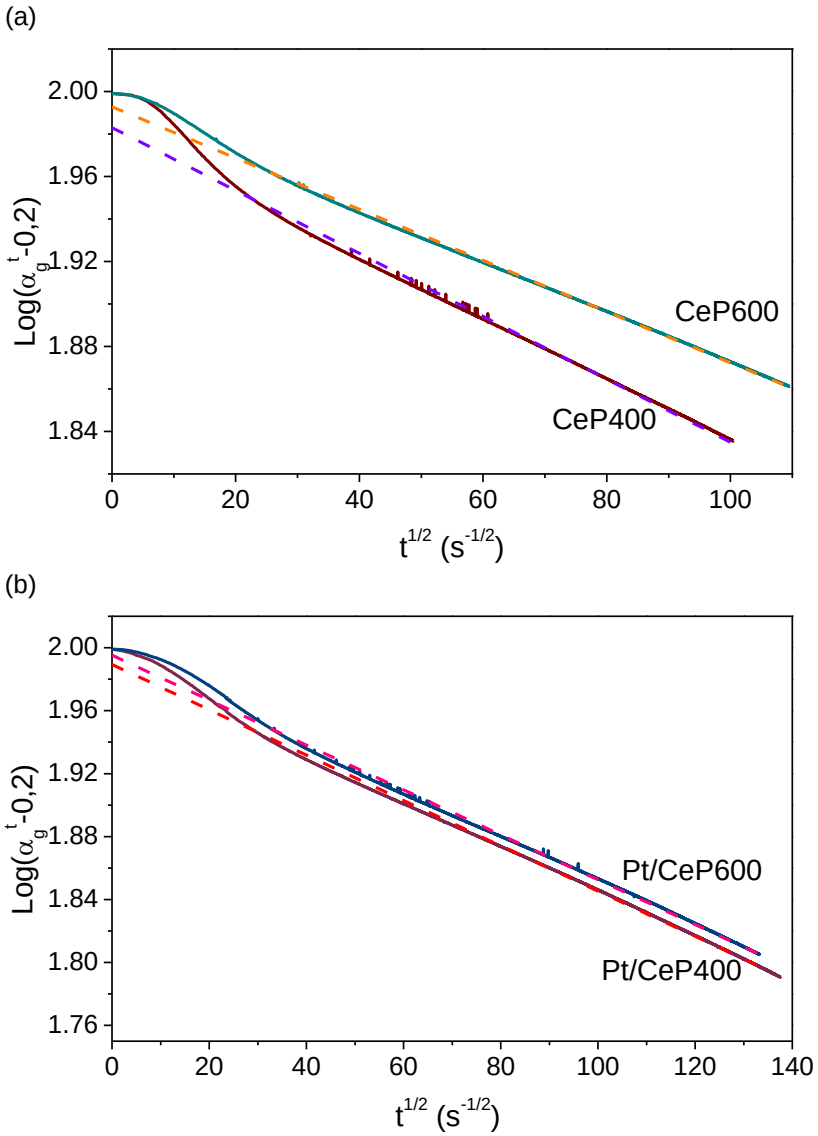

Figure 5.8. Linear fitting using Kakioka's model from CO_2 isotopic exchange results at 300 °C over (a) $CePO_4$ supports, (b) Pt catalysts

Table 5.3. Diffusion coefficient (D) of the $CePO_4$ supports and Pt catalysts calculated by Kakioka's model

Sample	D ($m^2 \cdot s^{-1}$)
CeP400	1.47×10^{-22}
CeP600	4.41×10^{-22}
Pt/CeP400	8.62×10^{-23}
Pt/CeP600	4.93×10^{-22}

5.4. *In situ* CO_2 adsorption followed by transmission IR spectroscopy

In order to understand the interaction of CO_2 with the supports and catalysts, CO_2 adsorption experiments followed by transmission IR spectroscopy and mass spectrometry were performed. CO_2 is an electron acceptor, thus being able to act as a Lewis acid toward O ions of the phosphate group, forming carbonate species, or basic OH surface groups to form hydrogen carbonate species [18] .

5.4.1. $CePO_4$ supports

In order to elucidate the possible species formed in both supports, CO_2 adsorption experiments at 30 °C were performed. The same experiment was carried out at 300 °C, that is, the temperature at which the isotopic exchange experiments were performed, in order to clarify which of the formed species remain in the catalyst at this temperature. For the sake of clarity, spectra are divided in three regions. Difference spectra of CeP400 at both temperatures are displayed in Figure 5.8. At 30 °C (Figure 5.8 (a), (b) and (c)) two doublets centered at 3716 cm^{-1} and 3615 cm^{-1} corresponds to the (v_1 + v_3) CO_2 combination band and the ($2v_2$ + v_3) combination/overtone band, respectively. Since the latter involves three excitations, its intensity is weaker than the (v_1 + v_3) combination band [19]. The band corresponding to the structural OH groups of the CeP400 support is also observed in this region (3667 cm^{-1}). Although it does not disappear completely, it undergoes a decrease in intensity and additionally, a growing contribution at 3703 cm^{-1} appears, meaning that the structural -OH groups react with CO_2 and gives rise to the generation of new OH groups. Thus, the band at 3703 cm^{-1} (vOH) together with the new bands at 1584 and 1380 cm^{-1} (v_{as}C-O and v_sC-O) denote the formation of hydrogen carbonate species [20-22]. Similar values for the C-O stretch vibrations have been reported in CeO_2 containing the Ce^{3+} cation [21], thus this result is in agreement with the presence of Ce^{3+} in CeP400 previously demonstrated by XPS (Chapter III). Although phosphate overtone and combination bands experience changes in the presence of CO_2, no negative bands are observed in that region, suggesting that the oxygen atoms of the phosphate groups are not participating in the reaction with CO_2. This fact added to the apparent absence of additional bands in the 1700-1300 cm^{-1} region demonstrates that the formation of carbonate species does not take place in the CeP400 support. Thus, the $C^{18}O_2/C^{16}O_2$ isotopic exchange in this solid seem to be possible uniquely by the formation of hydrogen carbonate species. Additionally, this result points out the Lewis acidity of the OH groups in the CeP400 solid.

At 300 °C (Figure 5.8 (d), (e) and (f)) no changes are observed in the OH region, whereas slight changes in the P-OH band (2884 cm^{-1}) and PO_4^{3-} overtones and combination modes region occur. A weak positive band is also observed at *ca.* 1580 cm^{-1}, but its intensity is insignificant. The fact that no intermediates are observed exposes the short lifetime of the hydrogen carbonate intermediates at this temperature [23-25].

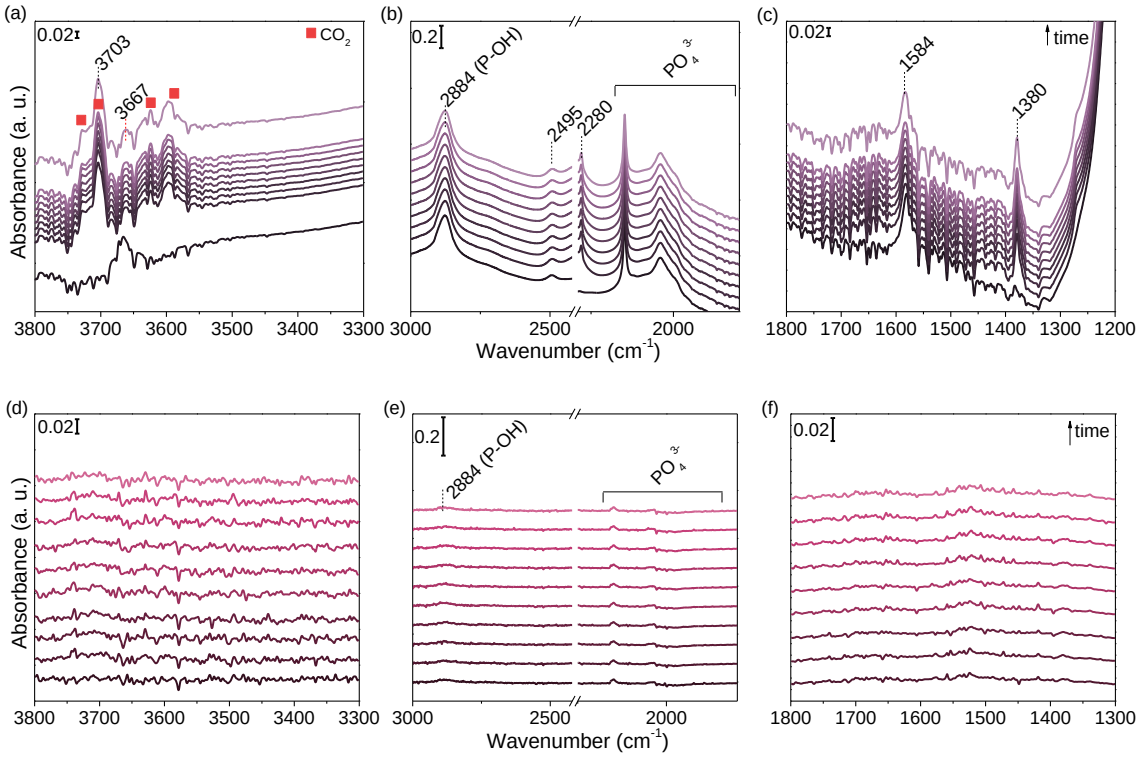

Figure 5.8. Difference spectra during CO_2 adsorption as a function of the time at (a, b, c) 30 °C and (d, e, f) 300 °C over CeP400

Results for the support CeP600 at 30 °C (Figure 5.9 (a), (b) and (c)) shows the appearance of the overtone/combination bands of CO_2 located in the OH region. Furthermore, the disappearance of the OH stretching band at 3670 cm^{-1} is observed, pointing out the formation of hydrogen carbonate species. In this case, two new OH species appear, indicating the formation of two types of hydrogen carbonate species in the CeP600 support. Similarly to the CeP400 support, the OH stretching vibration at 3703 cm^{-1}, with the bands at 1585 and 1380 cm^{-1} ascribed to the C-O asymmetric and symmetric stretching vibrations (ν_{as}C-O and ν_sC-O) denote the presence of hydrogen carbonate species coordinated to Ce^{3+} cations. The OH stretching vibration at 3678 cm^{-1} must be accompanied by growing bands in the 1632-1588 cm^{-1} and 1408-1132 cm^{-1} regions [21], but their identification becomes intriguing consider the simultaneous formation of carbonate species in this solid. The formation of carbonate species occurs as a consequence of the reaction of the CO_2 molecule with the oxygen atoms of the phosphate group. The participation of the oxygen is confirmed by the presence of negative bands at 1941 and 1905 cm^{-1}. The frequency of these bands is additionally shifted with respect to those observed after the activation treatment

(1948 and 1908 cm^{-1}), showing the symmetry changes induced in the phosphate groups due to this interaction. The simultaneous formation of carbonate and hydrogen carbonate species in CeP600 exposes that not only the OH groups but also the O atoms of the phosphate groups are basic in this support, thus being able to react with the CO_2 molecule.

Difference spectra during CO_2 adsorption on the CeP600 support at 300 °C (Figure 5.9 (c), (d) and (f)) shows, as well as at 30 °C, a weak negative contribution ascribed to the OH groups of the support. Nevertheless, the new OH generated are not observed due to their low intensity. Additionally, the vibrational modes corresponding to the C-O asymmetric and symmetric stretching (ν_{as}C-O) expected in the 1700-1300 cm^{-1} region are not observed at this temperature. However, several ill-defined contributions ascribed to carbonate species remain present at this temperature, which could indicate that these species do not act as intermediates during the $C^{18}O_2/C^{16}O_2$ isotopic exchange reaction. Therefore, the formation of carbonate species could block surface sites [26], leading to a minor formation of hydrogen carbonate species in the CeP600 support and consequently, decreasing both the number of exchanged atoms (N_e) and the rate of exchange (R_e) in this solid compared to CeP400.

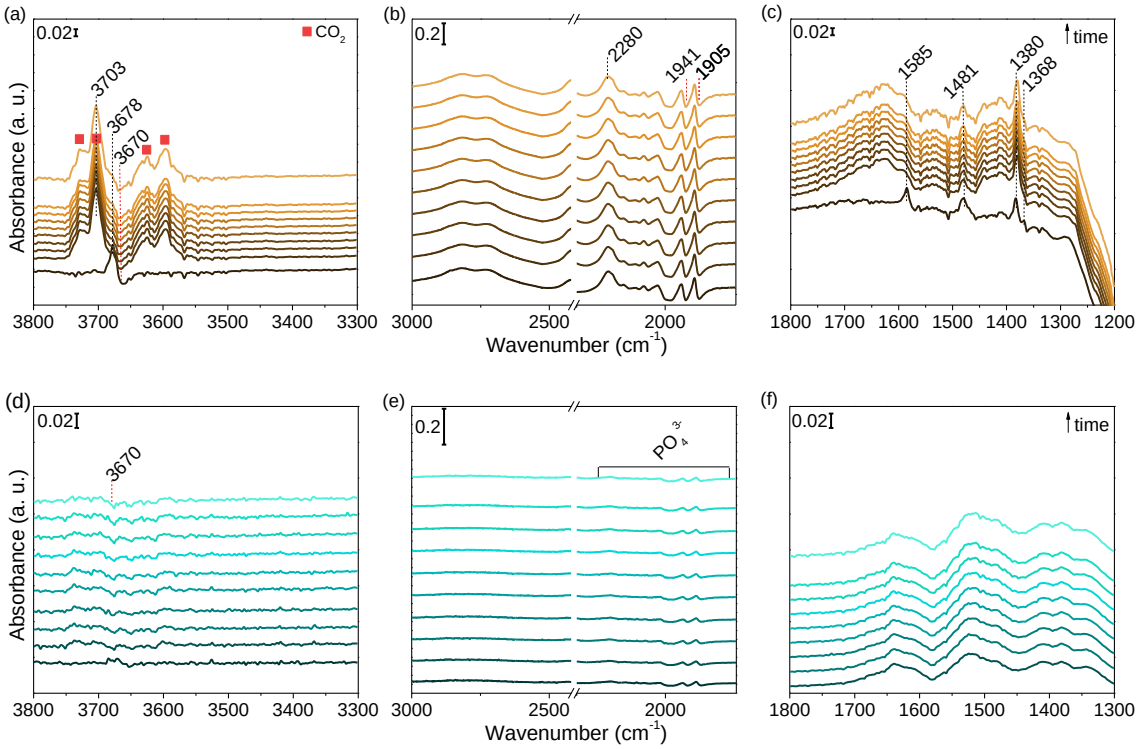

Figure 5.9. Difference spectra during CO_2 adsorption as a function of the time at (a, b, c) 30 °C and (d, e, f) 300 °C over CeP600

CO_2 adsorption experiments at 30 °C were additionally followed by mass spectrometry. The evolution of the CO_2 mass-on-charge (m/z= 44) as a function of the time presented in Figure 5.10, shows that the adsorption capacity of the support CeP400 is significantly superior to that of the support CeP600, in agreement with its greater oxygen exchange capacity during the reaction with $C^{18}O_2$.

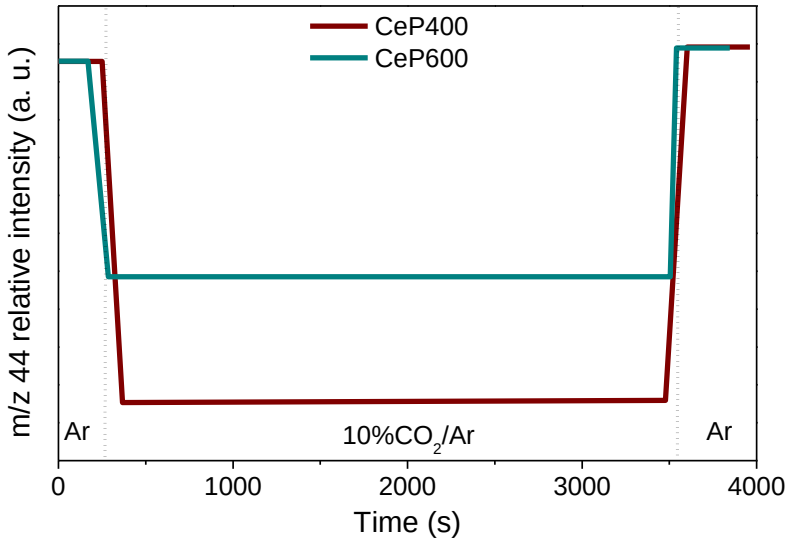

Figure 5.10. Mass spectra of CeP400 and CeP600 as a function of the time during CO_2 adsorption experiments

5.4.2. Pt catalysts

Difference spectra during CO_2 adsorption experiments on the Pt catalysts are presented in Figure 5.11. In the presence of Pt, significative changes are observed with respect to the corresponding supports.

For Pt/CeP400 at 30 °C (Figure 5.11 (a), (b), (c)), the intensity of the OH stretching mode decreases and a new OH group appears at 3702 cm^{-1}, which accompanied by the growing bands at 1588 and 1380 cm^{-1} indicates the formation of hydrogen carbonate species, as observed in the spectra of CeP400, although the intensity of the contributions is significantly smaller than in the support. Furthermore, additional bands near to 1600 cm^{-1} and 1400 cm^{-1} are observed, which involves the formation of new types of hydrogen carbonate species not present in the absence of Pt. Interestingly, the formation of different types of carbonates is also detected, accompanied by great changes in the region where overtones and combination bands of the phosphate group

appears. Negative bands at 1977 and 2017 cm^{-1}, corresponding to the $v_{3(P-O)} + v_{(P=O)}$ and $2v_{3(P-O)}$ combination/overtone bands, suggest the participation of the oxygen atoms of the phosphate groups in the formation of the carbonate species. Besides, a shift in their frequency is observed with respect to those observed in CeP400 after the activation treatment (1987 and 2025 cm^{-1}), pointing out the symmetry change induced in the phosphate group in the presence of CO_2. In addition, a band at 2060 cm^{-1} appears, which is not attributed to a phosphate mode. The presence of this contribution could be attributed to CO linearly adsorbed on Pt, suggesting the possibility that the dissociative adsorption of the CO_2 molecule into CO + O occurs in the presence of Pt. A similar result has been previously obtained in Pt/TiO_2 catalysts, where the formation of carbonates has been attributed to surface changes induced by the dissociation of the CO_2 molecule [27]. Thus, the formation of new species on Pt/CeP400 not detected on CeP400 has been tentatively attributed to the interaction of CO with both the OH groups and the O atoms of the phosphate group, according to the capacity of CO to react with either acidic or basic sites [22]. Another possibility for the formation of carbonates could be a change in the acid-base properties of the support induced by the platinum complex used as precursor during the catalyst synthesis [28].

When CO_2 adsorption is carried out at 300 °C (Figure 5.11 (d), (e), (f)), the dissociation of CO_2 into CO + O becomes evident in accordance with the appearance of bands assigned to CO linearly adsorbed on Pt at 2073 and 2065 cm^{-1}. At the exchange reaction temperature, no hydrogen carbonate species are observed, whereas ill-defined bands corresponding to carbonate species remain present. Taking into account that the $C^{18}O_2/C^{16}O_2$ exchange reaction occurs *via* formation of hydrogen carbonate species in CeP400, the formation of carbonates provoked by the presence of Pt seems to hinder the formation of hydrogen carbonates by blocking surface sites [26]. This fact could explain the decrease of N_e and R_e during the isotopic exchange reaction in Pt/CeP400 compared to the bare support.

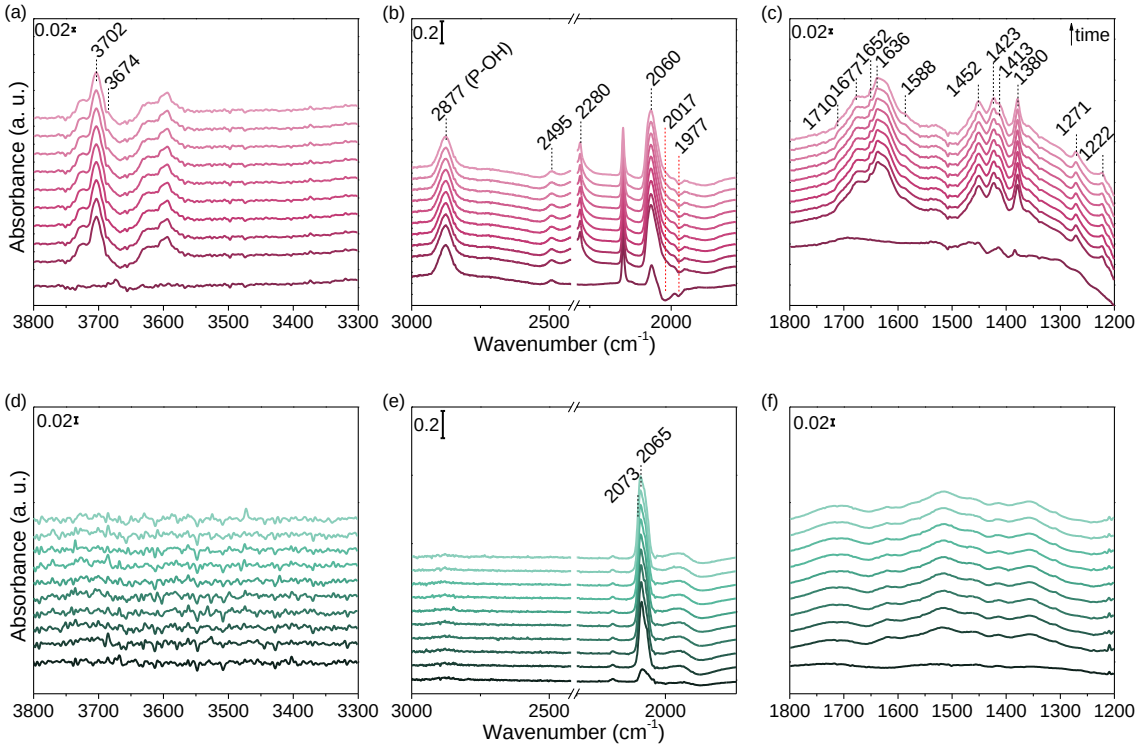

Figure 5.11. Difference spectra during CO_2 adsorption as a function of the time at (a, b, c) 30 °C and (d, e, f) 300 °C over Pt/CeP400

Difference spectra during CO_2 adsorption on Pt/CeP600 at 30 °C (Figure 5.12 (a), (b) and (c)) are similar to those observed for the CeP600 support. That is, formation of carbonate and two types of hydrogen carbonate species is detected. Additionally, the band at 2067 cm^{-1} suggests the dissociative adsorption of CO_2 into CO + O, as observed in the catalyst Pt/CeP400.

At 300 °C, the observation of hydrogen carbonate species is not possible, but weak bands corresponding to carbonate groups remain in the spectra.

Thus, results obtained for the Pt/CeP600 catalyst are similar to those obtained for the bare support, giving a reasonable explanation for the results obtained during the $C^{18}O_2/C^{16}O_2$ isotopic exchange experiments. Considering that the interaction of CO_2 with both the CeP600 support and the corresponding Pt catalyst is similar, that is, giving rise to the formation of carbonate and hydrogen carbonate species, it results reasonable that the extent of the oxygen exchange is similar in the absence and in the presence of Pt. This explains the similarity of the N_e and R_e values in CeP600 and Pt/CeP600.

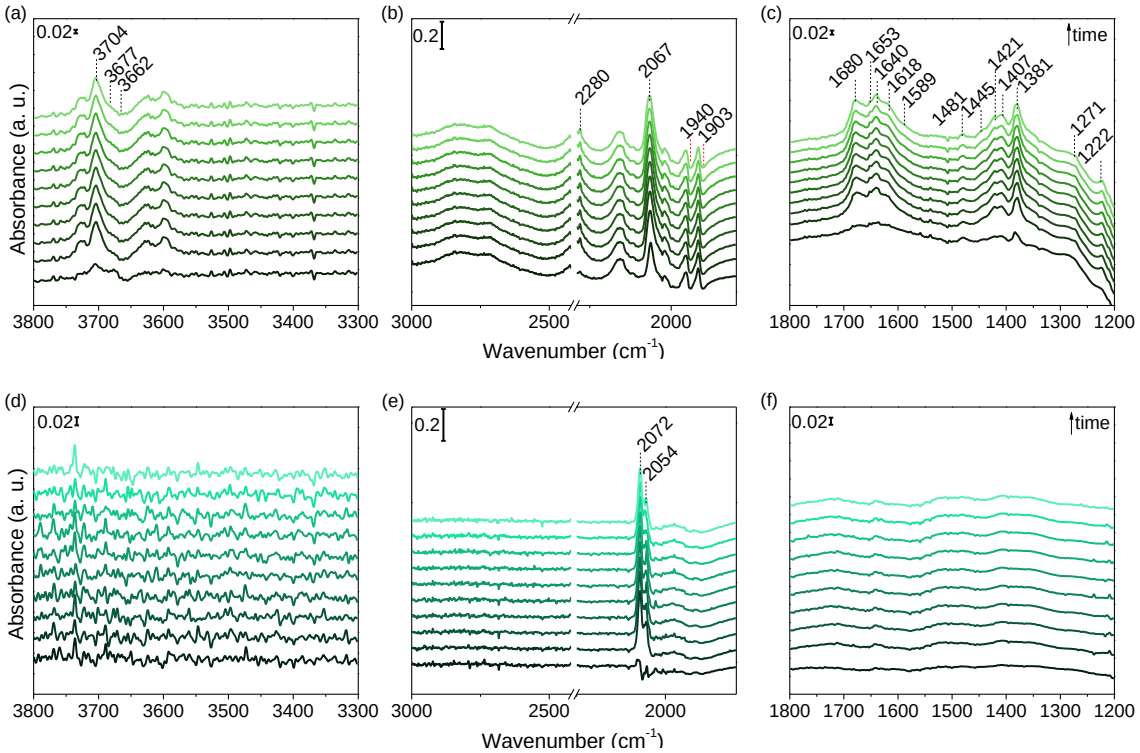

Figure 5.12. Difference spectra during CO_2 adsorption as a function of the time at (a, b, c) 30 °C and (d, e, f) 300 °C over Pt/CeP600

Simultaneously to the adsorption experiments, the mass spectra was recorded. Results are presented in Figure 5.13. In this case, the CO_2 adsorption capacity of Pt/CeP400 is just slightly superior to that of Pt/CeP600, in good agreement with the results obtained during the $C^{18}O_2$ isotopic exchange experiment, where the extent of the $C^{18}O_2/C^{16}O_2$ isotopic exchange on Pt/CeP400 was only slightly superior to that on Pt/CeP600.

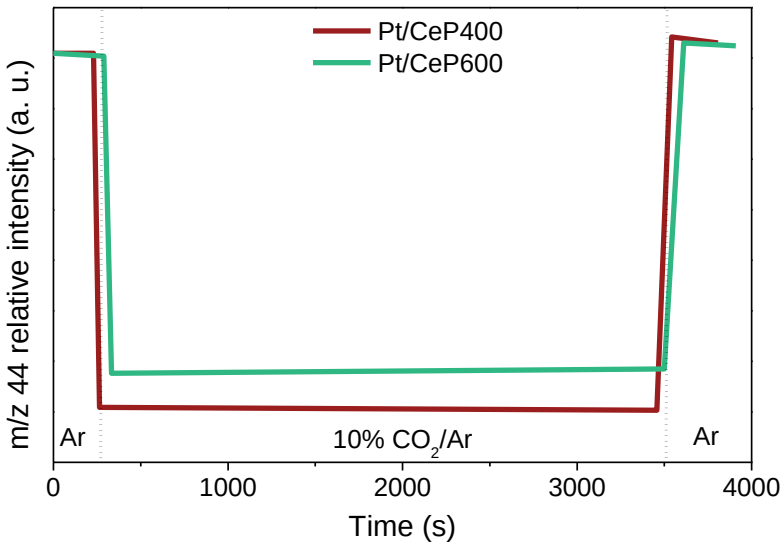

5.5. Partial conclusions

Oxygen isotopic exchange experiments have been performed over the $CePO_4$-based systems. Results using $^{18}O_2$ as labelled molecule demonstrate that both the supports and the Pt catalysts present no activity towards the oxygen exchange in the temperature range selected for the study of the WGS reaction (200-350 °C). This points out the lack of oxygen vacancies in these solids and, consequently, the WGS redox mechanism can be discarded. On the contrary, the $CePO_4$-based systems present great oxygen exchange activity using $C^{18}O_2$, which place the associative mechanism as the preferred path for the WGS reaction in these solids. Whereas the CeP400 support exceeds the exchange capacity of CeP600, a decrease of such exchange takes place in the presence of Pt, although it is still superior to that of Pt/CeP600. Additionally, no significative changes are observed between the exchange capacity of CeP600 in the absence or the presence of Pt. CO_2 adsorption experiments followed by IR spectroscopy and mass spectrometry allow to conclude that the $C^{18}O_2$ isotopic exchange reaction takes place mainly through the formation of hydrogen carbonate intermediate species. However, carbonate species seem to decrease the exchange capacity of the solids, suggesting that the participation of carbonates in the exchange reaction is unlikely and they act probably as spectator species blocking surface sites. Thus, the presence of surface carbonate species seems to hinder the formation of hydrogen carbonates that contribute to the exchange. Consequently, the exchanged oxygen atoms in the $CePO_4$ solids come mainly from the OH groups and not from the phosphate group oxygen ions.

5.6. References

[1] J. Vecchietti, A. Bonivardi, W. Xu, D. Stacchiola, J.J. Delgado, M. Calatayud, S.E. Collins, Understanding the Role of Oxygen Vacancies in the Water Gas Shift Reaction on Ceria-Supported Platinum Catalysts, ACS Catalysis, 4 (2014) 2088-2096.

[2] R. Jain, A.S. Poyraz, D.P. Gamliel, J. Valla, S.L. Suib, R. Maric, Comparative study for low temperature water-gas shift reaction on Pt/ceria catalysts: Role of different ceria supports, Applied Catalysis A: General, 507 (2015) 1-13.

[3] C.G. Maciel, T.d.F. Silva, E.M. Assaf, J.M. Assaf, Hydrogen production and purification from the water–gas shift reaction on CuO/CeO2–TiO2 catalysts, Applied Energy, 112 (2013) 52-59.

[4] C.M. Kalamaras, D.D. Dionysiou, A.M. Efstathiou, Mechanistic Studies of the Water–Gas Shift Reaction over Pt/CexZr1–xO2 Catalysts: The Effect of Pt Particle Size and Zr Dopant, ACS Catalysis, 2 (2012) 2729-2742.

[5] M. González-Castaño, T. R. Reina, S. Ivanova, L.M. Martínez Tejada, M.A. Centeno, J.A. Odriozola, O 2 -assisted Water Gas Shift reaction over structured Au and Pt catalysts, Applied Catalysis B: Environmental, 185 (2016) 337-343.

[6] D. Duprez, Study of surface reaction mechanisms by 16O/18O and H/D isotopic exchange, Catalysis Today, 112 (2006) 17-22.

[7] S. Ojala, N. Bion, S. Rijo Gomes, R.L. Keiski, D. Duprez, Isotopic Oxygen Exchange over Pd/Al2O3 Catalyst: Study on C18O2 and 18O2 Exchange, ChemCatChem, 2 (2010) 527-533.

[8] I. Maupin, J. Mijoin, T. Belin, C. Morais, V. Montouillout, D. Duprez, N. Bion, Direct evidence of the role of dispersed ceria on the activation of oxygen in NaX zeolite by coupling the 17O/16O isotopic exchange and 17O solid-state NMR, Journal of Catalysis, 300 (2013) 136-140.

[9] W. Yang, R. Zhang, B. Chen, N. Bion, D. Duprez, L. Hou, H. Zhang, S. Royer, Design of nanocrystalline mixed oxides with improved oxygen mobility: a simple non-aqueous route to nano-LaFeO3 and the consequences on the catalytic oxidation performances, Chemical Communications, 49 (2013) 4923-4925.

[10] D. Duprez, Isotopes in Heterogeneous Catalysis, Imperial College Press2006.

[11] T. Rajesh, N. Devi, Role of oxygen vacancies in the water gas shift reaction: activity study on BaCe0.98-xYxPt0.02O3-delta perovskites, Journal of Physical Chemistry C, 118 (2014) 20867-20874.

[12] M. González-Castaño, S. Ivanova, T. Ioannides, M.A. Centeno, J.A. Odriozola, Deep insight into Zr/Fe combination for successful Pt/CeO2/Al2O3WGS catalyst doping, Catalysis Science & Technology, 7 (2017) 1556-1564.

[13] J. Nakamura, J.M. Campbell, C.T. Campbell, Kinetics and Mechanism of the Water-gas Shift Reaction Catalysed by the Clean and Cs-promoted Cu(110) Surface: A Comparison with Cu(111), Journal of the Chemical Society, Faraday Transactions, 86 (1990) 2725-2734.

[14] K.C. Petallidou, C.M. Kalamaras, A.M. Efstathiou, The effect of La3+, Ti4+ and Zr4+ dopants on the mechanism of WGS on ceria-doped supported Pt catalysts, Catalysis Today, 228 (2014) 183-193.

[15] O. Thinon, K. Rachedi, F. Diehl, P. Avenier, Y. Schuurman, Kinetics and Mechanism of the Water–Gas Shift Reaction Over Platinum Supported Catalysts, Topics in Catalysis, 52 (2009) 1940-1945.

[16] V. Ducarme, J.C. Vedrine, Study of Surface Atom Behaviour on Pt/SiO2 and Pt/Al2O3 Catalysts by Isotopic Exchange of Oxygen from CO2, Journal of the Chemical Society, Faraday Transactions 1, 74 (1977) 506-508.

[17] N. García-Moncada, M. González-Castaño, S. Ivanova, M.Á. Centeno, F. Romero-Sarria, J.A. Odriozola, New concept for old reaction: Novel WGS catalyst design, Applied Catalysis B: Environmental, 238 (2018) 1-5.

[18] C. Binet, M. Daturi, J.-C. Lavalley, IR study of polycristalline ceria properties in oxidised and reduced states, Catalysis Today, 50 (1999) 207-225.

[19] S.A. Sandford, L.J. Allamandola, The physical and infrared spectral properties of CO2 in astrophysical ice analogs, The Astrophysical Journal, 355 (1990) 357-372.

[20] G. Busca, V. Lorenzelli, Infrared spectroscopic identification of species arising from reactive adsorption of carbon oxides on metal oxide surfaces, Materials Chemistry, 7 (1982) 89-126.

[21] G.N. Vayssilov, M. Mihaylov, P.S. Petkov, K.I. Hadjiivanov, K.M. Neyman, Reassignment of the Vibrational Spectra of Carbonates, Formates, and Related Surface Species on Ceria: A Combined Density Functional and Infrared Spectroscopy Investigation, The Journal of Physical Chemistry C, 115 (2011) 23435-23454.

[22] J.-C. Lavalley, Infrared spectrometric studies of the surface basicity of metal oxides and zeolites using adsorbed probe molecules, Catalysis Today, 27 (1996) 377-401.

[23] F. Wang, Z. Liu, G. Weng, Profiling the short-lived cationic species generated during catalytic dehydration of short-chain alcohols, Communications Chemistry, 51 (2018) 1-7.

[24] S.M. Senkan, High-throughput screening of solid-state catalyst libraries, Nature, 394 (1998) 350-353.

[25] D.W. Robbins, J.F. Hartwig, A simple, multidimensional approach to high-throughput discovery of catalytic reactions, Science, 333 (2011) 1423-1427.

[26] F.C. Meunier, D. Tibiletti, A. Goguet, D. Reid, R. Burch, On the reactivity of carbonate specieson a Pt/CeO2 catalyst under various reaction atmospheres: Application of the isotopic exchange technique, Applied Catalysis A: General, 289 (2005) 104-112.

[27] K. Tanaka, J.M. White, Dissociative Adsorption of CO2 on Oxidized and Reduced Pt/TiO2, The Journal of Physical Chemistry, 86 (1982) 3977-3980.

[28] S. Santiago-Pedro, V. Tamayo-Galván, T. Viveros-García, Effect of the acid-base properties of the support on the performance of Pt catalysts in the partial hydrogenation of citral, Catalysis Today, 213 (2013) 101-108.

Chapter VI

Preliminary study of Ca and Ti phosphate-type supports: Comparison with $CePO_4$

Abstract

Considering the suitability of the $CePO_4$ supports for the WGS reaction, the objective of this chapter is the exploration of other phosphate-based systems as supports for the WGS reaction, in particular calcium and titanium phosphate-type supports. Their textural, structural and surface properties are evaluated and related to their behavior during the WGS reaction. Additionally, their interaction mechanism with the water molecule is studied by means of *in situ* water adsorption experiments followed by DRIFTS and mass spectrometry. The obtained results are compared with those obtained for the CeP400 and CeP600 supports.

6.1. Introduction

Throughout this work, the possibility of adapting the $CePO_4$ conduction properties to WGS catalytic systems has been highlighted. Consequently, the presented results suggest that the same could be possible with another phosphate-type materials presenting similar conduction properties. Additionally, the main potential of phosphate-type solids lies in the possibility of tuning their chemical and structural properties and consequently, their texture and surface properties. In this sense, the texture of the support, especially its porosity, influences both the adsorption and ion-exchange abilities of the material [1-3], whereas the selection of the metal cation and the inorganic anion becomes crucial for the effective control of the surface acid-base properties [4]

In this context, calcium hydroxyapatite, $Ca_{10}(PO_4)_6(OH)_2$, has demonstrated to present ionic conduction properties even at high temperatures, which have allowed its use as ion-conducting membrane in fuel cells and as humidity sensor, among others [5, 6]. These conduction properties have been attributed to the migration of protons in adsorbed and/or condensed water [7] and to the presence of OH groups in the structure [5, 8]. Furthermore, such properties have demonstrated to be influenced by several aspects, as the hydration degree or the size of the structural defects [9]. In addition, the calcium hydroxyapatite system has been already used as support for the WGS reaction, being its catalytic performance attributed to a superior water activation rate due to its structural stability, hydrophilicity and the possibility of cationic and anionic isomorphous substitutions [10, 11].

Another interesting solid due to its remarkable proton conductivity is TiP_2O_7, previously used as fuel cell electrolyte [12, 13]. In the presence of high humidity, formation of P-OH groups takes place in this solid [14], enabling the proton conduction phenomena by providing protons able to be exchanged between neighboring groups, surface water and hydroxyl groups. Although the conduction mechanism in this solid is not clearly determined, it seems to be dependent of the calcination temperature and the phosphorous content of the solid [15], which, at the same time, influence its structural and textural characteristics.

Thus, the conduction properties shown by the Ca and Ti phosphate-type systems in the presence of water suggest the possibility for these materials to be used as supports for WGS catalysts and

influence the interaction with the water molecule which, consequently, determine the WGS reaction mechanism.

Considering the aspects mentioned above, two phosphate-type supports containing Ca and Ti have been synthesized, characterized and evaluated as supports for WGS Pt catalysts. Additionally, *in situ* water adsorption experiments followed by DRIFTS and mass spectrometry were performed in order to evaluate their interaction with the water molecule. Their structural and surface properties, as well as their catalytic behavior have been compared with those of the CeP400 and CeP600 supports.

6.2. Supports and Pt catalysts synthesis

Two phosphate-type supports containing different cations (Ca and Ti) were prepared by a hydrothermal method, with nominal molar ratios Ca/P 1.67:1 and Ti/P 1:1. The obtained solids were labelled as CaP and TiP respectively.

CaP was prepared similarly to CeP400 and CeP600 [16, 17]. 50 ml of aqueous solutions of phosphoric acid 85% (Panreac) 0.6 M and calcium nitrate tetrahydrate (VWR) 1 M were mixed in a flask and stirred at 40 °C. Then, 50 ml of an aqueous solution of sodium citrate dihydrate (Sigma) 0.017 M was added and the pH was adjusted to 10 by means of the addition of ammonia 30%. The resultant solution was maintained at 40 °C for 8 hours under stirring and finally transferred to a Teflon-lined autoclave, in which the mixture was aged at 100 °C for 8 hours. The material was finally filtered, washed with distilled water and dried overnight at 100 °C. The obtained solid was finally calcined at 350 °C.

The synthesis of TiP was carried out by means of an adapted hydrothermal method [18]. 50 ml of a phosphoric acid 85% (Panreac) aqueous solution 0.7 M were mixed with $6 \cdot 10^{-4}$ moles of P123 (BASF) and maintained under stirring until complete dissolution of the surfactant. 0.04 moles of $C_{12}H_{29}O_4Ti$ (Aldrich) were then added and the resultant solution was stirred for 2 hours. The mixture was sealed in a Teflon-lined autoclave and aged at 80 °C for 24 h. The obtained product was filtered, washed with water, dried overnight at 60 °C and finally calcined at 600 °C in order to ensure the complete elimination of the surfactant.

The Pt catalysts with a nominal metal content of 2 wt.% were prepared, similarly to the Pt/CeP catalysts, by the wet impregnation method. For this purpose, an aqueous solution of $Pt(NH_3)_4(OH)_2$ 0.053 M was prepared, and the corresponding amount of support was added. The mixture was maintained under stirring for 24 hours and dried at 60 °C. Finally, the obtained catalysts were calcined at 350 °C for 2 hours.

6.3. Physicochemical characterization

6.3.1. X-ray diffraction (XRD) analyses

X-ray diffraction patterns of the prepared solids are shown in Figure 6.1 (a). CeP400 and CeP600 supports present the diffraction lines corresponding to the rhabdophane and monazite-type phases of $CePO_4$, as described in Chapter III. The diffraction pattern of CaP corresponds to the hexagonal calcium hydroxyapatite structure ($P6_3/m$ space group), with formula $Ca_{10}(PO_4)_6(OH)_2$ (JCPDS-ICDD 01-074-0566). According to the literature [16, 19], the hydroxyapatite framework is constituted by the assembly of calcium ions and tetrahedral phosphate groups delimiting two types of unconnected channels oriented along the *c* axis: one of them has a diameter of 2.5 Å and is bordered by calcium ions, and the second one possesses a diameter of approximately 3.5 Å and is bordered not only by calcium ions but also by oxygen atoms. These channels contain the structural OH groups which balance the positive charge of the compound. Conversely to the previous supports, the support TiP seems to present either a low degree of crystallinity or a crystalline nature but small crystallite size. The amorphization degree of TiP have been previously related to the time and temperature conditions of the hydrothermal method employed during the synthesis [20, 21]. Nevertheless, it is possible to distinguish a broad diffraction line at 25.2 °2θ, related to the presence of the anatase phase of TiO_2 (JCPDS-ICDD 00-002-0387). Although the anatase-rutile transition phase takes place between 500 and 600 °C, the presence of phosphorous has demonstrated to increase the thermal stability of the anatase phase [22], which explains the presence of this phase after calcination at 600 °C. Additionally, a diffraction peak at 22.4 °2θ, corresponding to the most intense diffraction line of TiP_2O_7 (JCPDS-ICDD 00-038-1468) is observed. An enlargement of this region is presented in Figure 6.1 (b). Thus, this solid consists in a mixture of TiP_2O_7 and TiO_2, in good agreement with the loss of phosphorous induced by the calcination treatment revealed by chemical analysis. After Pt deposition and calcination of the

solids, no diffraction lines corresponding to Pt species are observed, indicating the small particle size of the metallic particles in all the samples. Nevertheless, the catalyst Pt/TiP presents an increase of the diffraction peak at 25.2 °2θ, suggesting that the segregation of anatase occurs after Pt deposition and calcination.

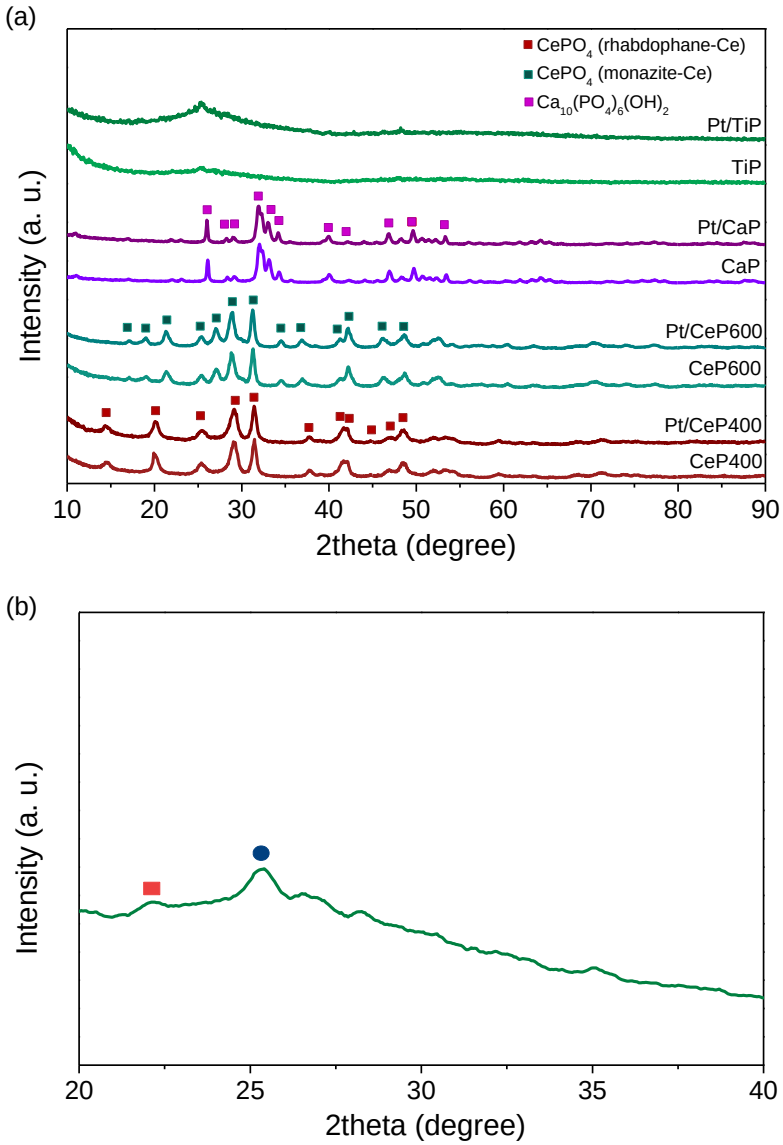

Figure 6.1. (a) XRD patterns of the prepared solids, (b) enlargement of the TiP XRD pattern

6.3.2. Physicochemical and textural properties

Table 6.1 summarizes the physicochemical properties of the prepared solids. Specific surface area values of the supports are in the range between 41 and 248 m^2 g^{-1}, being that of TiP significantly higher compared to the other prepared supports. Pore volume values are comprised

between 0.32 and 0.62 $cm^3\ g^{-1}$, corresponding the maximum value to TiP. After Pt deposition and calcination, no significative changes on these values are observed, being similar to those of the supports. Regarding the cation/phosphorous (C/P) molar ratio of the supports, the values obtained are those expected from the synthesis procedure except for the solid TiP, which indicates that a loss of phosphorous has taken place in this solid.

Table 6.1. Physicochemical properties of the supports and catalysts

Sample	S_{BET} ($m^2\ g^{-1}$) (nm)	V_p ($cm^3\ g^{-1}$)	D_p	Pt mean particle size (nm)[a]	Metal loading (wt %)	C/P ratio
CeP400	65	0.32	17.2	-	-	-
CeP600	41	0.35	28.2	-	-	-
CaP	69	0.39	16.8	-	-	-
TiP	248	0.62	8.5	-	-	-
Pt/CeP400	71	0.32	16.6	1	1.5	1
Pt/CeP600	44	0.30	23.2	1.2	1.4	1
Pt/CaP	73	0.47	19.4	0.7	1.4	1.7
Pt/TiP	246	0.58	8.2	2.6	1.6	2.2

[a] Calculated from TEM micrographs

Figure 6.2 presents the N_2 adsorption/desorption isotherms and the BJH pore size distribution curves of the supports after calcination. Figure 6.2 (a) shows that supports containing Ce and Ca present a pronounced adsorption at $p/p_0 \approx 0.8$, indicating that multilayer adsorption starts at high relative pressure in these solids, thus denoting a great mesopore population. However, the adsorption isotherm of the support TiP shows a superior adsorption capacity from $p/p_0 \approx 0.5$, thus pointing out that this material exhibits a greater microporosity feature. In addition, the middle section of the curve is less defined that in the other supports, which shows that formation of mono- and multilayer are overlapped. Considering the hysteresis loop [23], both CeP supports present a H1 hysteresis, typical of solids containing uniform channels, as in the support CeP400 or constituted by aggregates of particles, as in CeP600. The solid CaP gives rise to a H2 hysteresis, characteristic of solids containing cylindrical channels with non-uniform size and shape, being consistent with the description of the hydroxyapatite structure in which two types of structural channels have been described [16, 24]. The solid TiP presents a H3 hysteresis, typically found in non-rigid aggregates of particles and thus, not representing a reliable description of the porosity of the material [23, 25]. According to the BJH pore size distribution derived from the isotherm (Figure 6.2 (b)), the mesopore volume decreases in the order: CaP > CeP400 > CeP600 > TiP.

Although this distribution could include interparticle voids, this trend is in agreement with the description of the supports features shown in Table 6.1. This reduction of the mesopore volume is accompanied by a broadening of the pore size distribution. After Pt deposition, the evolution of the adsorption isotherms and the pore size distribution (not shown) follow the same trend observed for the supports.

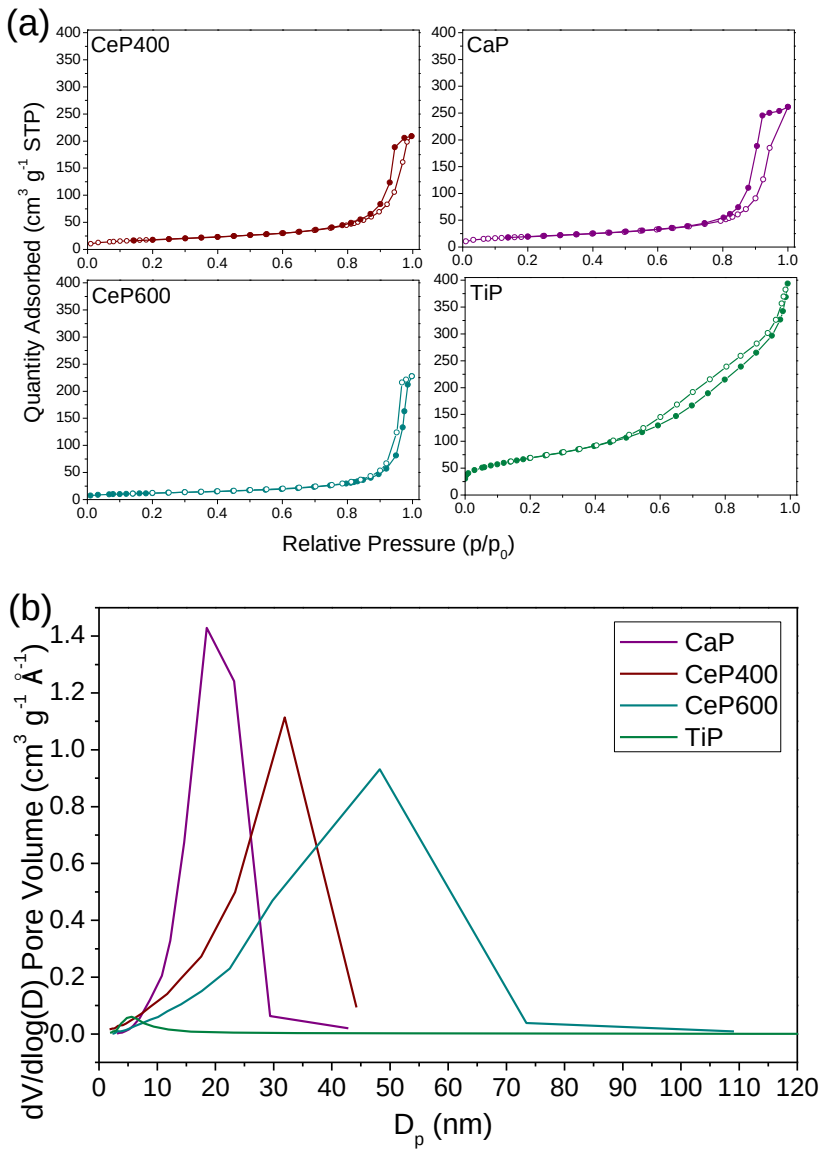

Figure 6.2. (a) N_2 adsorption/desorption isotherms and (b) BJH pore size distribution of the supports after calcination

6.3.3. Transmission electron microscopy (TEM)

Figure 6.3 shows the TEM micrographs and the Pt particle size distribution of the prepared catalysts. In the rhabdophane-type phase of $CePO_4$, the particles are bar-shaped with a length of

ca. 120 nm. The oxygen atoms of the structure are forming a series of parallel channels along the *c* axis, in which water molecules can be accommodated [26-29]. The bar-like structure of the support is maintained after calcination at 600 °C, but a decrease of the bars length takes place, along with the disappearance of the structural channels, due to the formation of the monazite-type phase of $CePO_4$, as reported in Chapter III [29]. Calcium hydroxyapatite consists in bar-like particles of ca. 38 nm, with structural channels along the hexagonal axis, well known for their capacity of trapping molecules [30], whereas support TiP present an irregular shape and no cavities are observed in its structure. The Pt species are highly dispersed on these solids, in good agreement with the XRD results, with particle sizes between 0.7 and 2.6 nm. However, supports with structural channels CeP and CaP show narrower particle size distributions, as well as a preferential arrangement of the Pt particles in the direction of the structural channels. This could be attributed to the structural characteristics of the support. Well-ordered channel structures have demonstrated to favor good dispersion of the metal particles, as well as prevent them of sintering [31].

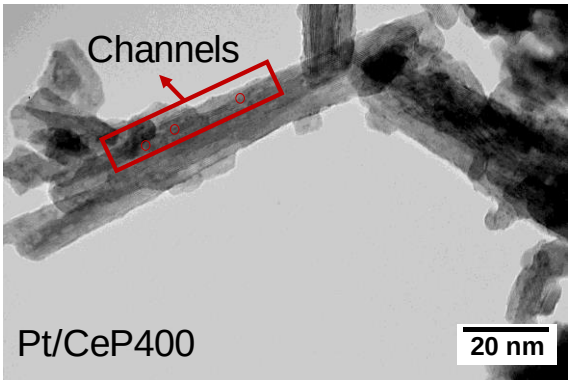

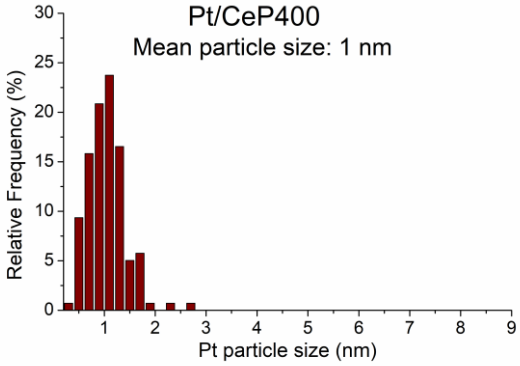

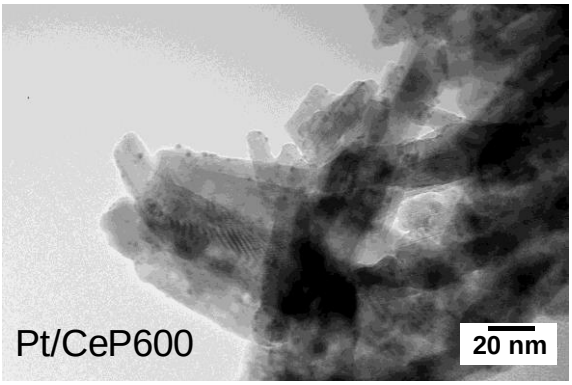

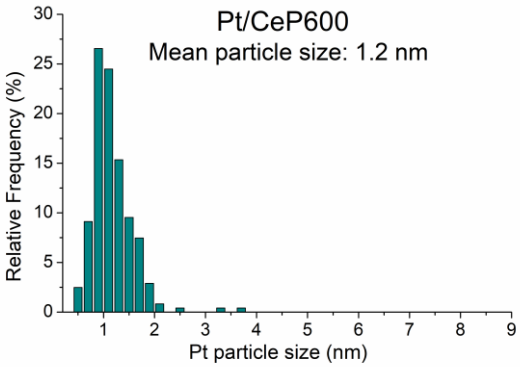

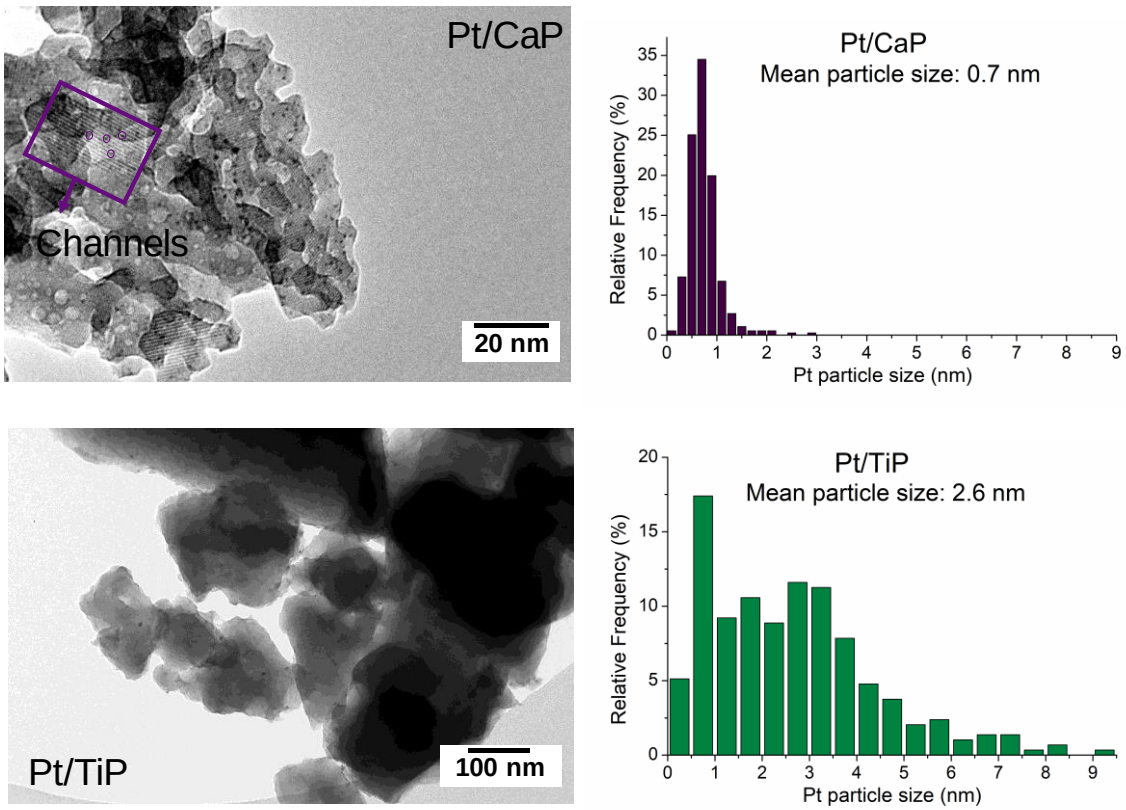

Figure 6.3. TEM micrographs and particle size distribution of the prepared catalysts

6.4. Catalytic activity of the phosphate-based catalysts on the WGS reaction

Catalytic activity tests of the prepared solids were carried out using the so-called feed-stream B, described in Chapter II. The volume percent composition of both feed-streams is shown in Table 6.2. Every experience was performed at WHSV = 30 $L \cdot g^{-1} \cdot h^{-1}$, according to equation 2.9 (Chapter II).

Table 6.2. Composition of the WGS reaction mixture

Reactant	Feed B (Vol %)
CO	7
H_2O	30
N_2	4
CO_2	9
H_2	50

Figure 6.4 shows the catalytic activity results of the Pt catalysts.

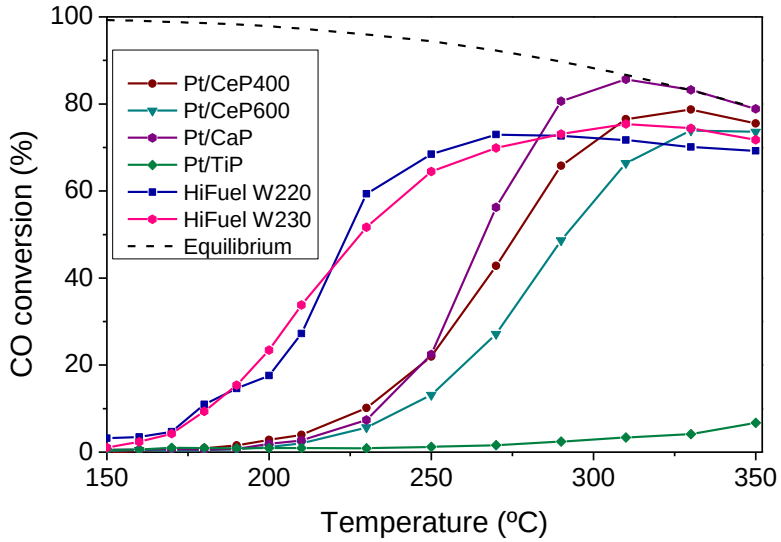

Figure 6.4. CO conversion of phosphate-supported Pt catalysts and commercial catalysts as a function of the reaction temperature under feed-stream B (7% CO, 9% CO_2, 30% H_2O, 50% H_2 and 4% N_2). WGS equilibrium curve is also presented

The catalytic performance of the evaluated solids decreases in the order: Pt/CaP > Pt/CeP400 > Pt/CeP600 > Pt/TiP. Whereas the catalyst Pt/CaP reaches the equilibrium conversion at 310 °C, those supported on CeP achieve it at 350 °C, and the Pt/TiP catalyst present a limited catalytic activity, with a CO conversion value lower than 10% at 350 °C. This result could be attributed to the mean Pt particle size in every sample as well as to the interaction of the support with the water molecule during the reaction, directly related with the pore size and volume of each support as confirmed by the N_2 physisorption results. The trend followed by the Pt catalysts indicates that supports with structural channels, rather those supported on CaP or CeP400, lead to an enhancement of the catalytic behavior. Considering that CO_2 and H_2 are potential reactants for the methanation reaction, it has been generally reported that their presence induces a negative effect on the WGS catalytic activity [32]. However, no methane was detected at the reactor outlet with the studied phosphate-supported catalysts. The catalytic activity of Cu-based LT (HiFuel W220) and MT (HiFuel W230) WGS commercial catalysts (Alfa Aesar™) is showed for comparison. The commercial catalysts exceed the activity of the Pt/TiP catalyst in all the temperature range evaluated, and those of the remaining solids in the temperature range between 150 and 290 °C. However, from 310 °C, the catalysts Pt/CaP and Pt/CeP400 exceed the CO

conversion achieved by the commercial catalysts, whereas the system Pt/CeP600 becomes more active than the catalyst HiFuel W230 and equal to the catalyst HiFuel W220 from 330 °C. Furthermore, none of the commercial catalysts reach the equilibrium conversion in the evaluated conditions, in contrast to the CaP and CeP supported catalysts. These results point out the suitability of the studied phosphate-based systems for the WGS reaction, particularly those containing channels, that is CaP and CeP400.

A correlation between the catalysts pore volume and the temperature at which they reach a particular value of CO conversion value is shown in Figure 6.5. Given that the description of the porosity of Pt/TiP is not representative of the real characteristics of the material, which presents mainly micropores, this correlation is not presented for this catalyst. However, it exists a clear connection between the mesopore volume of the remaining catalysts and their catalytic activity, demonstrating that an increasing mesopores population in the solid gives place to a decrease of the temperature at which they reach a certain conversion value. Whereas the catalyst Pt/CeP600, with a lower pore volume, requires higher temperatures, the catalysts whose supports present structural channels, and hence a superior pore volume, lead to an improvement of the catalytic activity, which is consistent considering that the porosity of the support seems to influence the interaction of the catalyst with the water molecule and consequently the availability of water during the WGS reaction [29].

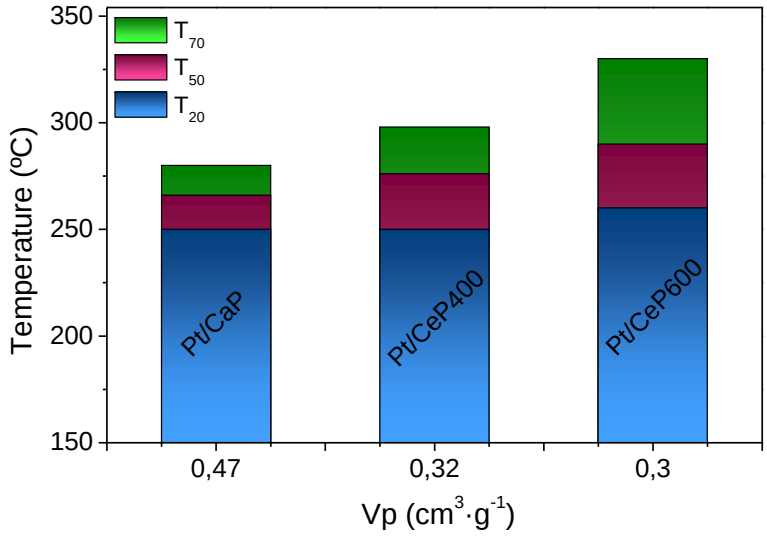

Figure 6.5. Temperature at which Pt catalysts reach a 20 (T_{20}), 50 (T_{50}) and 70% (T_{70}) of CO conversion as a function of the pore volume of the catalysts

6.5. *In situ* water adsorption experiments followed by DRIFTS and Mass Spectrometry

Water adsorption experiments (10% H_2O/Ar) followed by DRIFTS and mass spectrometry were carried out in order to understand the influence of the water-support interactions on the WGS catalytic performance. DRIFT spectra of the evaluated supports after the activation treatment are presented in Figure 6.6 and assignment of the vibration bands are summarized in Table 6.3. Every support present bands in the OH stretching region (Fig. 6.6 (a)), indicating the presence of structural OH groups, as well as bands corresponding to the P=O stretching mode (figure 6.6 (b)) [33, 34]. Although the solid TiP present low IR activity, weak bands in these regions can be intuited. The shift of the P=O stretching in the solid TiP towards higher wavenumbers is related to the deformation of the P=O bonds by the Ti-O environment [22]. Additional phosphate vibration modes are not observed in this solid, which is consistent with the loss of phosphorous induced during the calcination treatment.

As explained in Chapter IV the solids CeP400 and CeP600 show a band at 3670 cm^{-1} ascribed to surface -OH groups. Bands in the 900-1100 cm^{-1} range, corresponding to the symmetric P-O stretching (v_1) and asymmetric P-O stretching modes (v_3) are also observed, as well as a group of bands in the 2100-2400 cm^{-1} range (not shown), ascribed to overtone and combination bands of the phosphate vibrations [35]. Regarding the solid CeP400, a band at 2884 cm^{-1}, attributed to the P-OH stretching mode characteristic of acid ortophosphates (PO_4^{3-} + H_2O) is also observed [29, 33].

Contrary to the CeP supports, the solid CaP present several bands in the -OH stretching region. The band at 3568 cm^{-1} has been attributed to the stretching vibration of OH ions on lattice sites of the hydroxyapatite structure [16, 36, 37], whereas the presence of carbonate groups in the structure could also explain the appearance of a shoulder at 3535 cm^{-1}, previously attributed to surface OH groups locally perturbed by the presence of CO_3^{2-} groups [37]. Additionally a series of very weak bands at higher wavenumbers are observed, which have been assigned previously to either surface $Ca(OH)_2$ or surface P-OH groups. Particularly the weak band at about 3660 cm^{-1} could appear due to the presence of P-OH groups belonging to surface acidic phosphate ions HPO_4^{2-}, since a band at this frequency has been observed in phosphoric acid impregnated silica gels [36, 38]. Bands in the 900-1100 cm^{-1} region are also observed considering the presence of

phosphate groups. Both the differences on the vibration frequency values and the number of bands in this region indicate different degree of distortion of the PO_4^{3-} tetrahedra as a consequence of the phosphate group environment in every solid [29, 35]. As in the CeP supports, an additional set of bands attributed to overtones and combination bands of the phosphate group appears in the 2100-2400 cm^{-1} range [35]. Hydroxyapatites are characterized by the substitution of OH^- or PO_4^{3-} groups by CO_3^{2-} groups, giving rise to the so called type A and type B substitution respectively [39]. Therefore, vibrations corresponding to the CO_3^{2-} group are present. A-type carbonate species in apatite structures are characterized by absorption bands at 1545 and 1450 cm^{-1}, corresponding to the asymmetric and symmetric stretching respectively, and a singlet at 880 cm^{-1}, whereas the B-type carbonate species are expected at 1455, 1410 and 875 cm^{-1}. In this sample, two intense bands at 1417 and 1448 $cm^{-1}$are observed, as well as a singlet at 872 cm^{-1}, which allows to conclude that a type B substitution has taken place in this solid. This result is in agreement with the previously described band at 3535 cm^{-1}, related to the presence of carbonates.

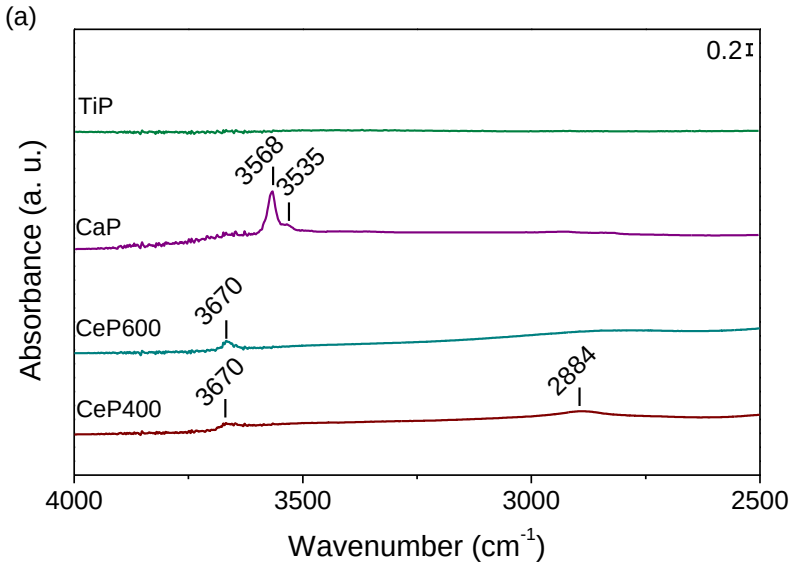

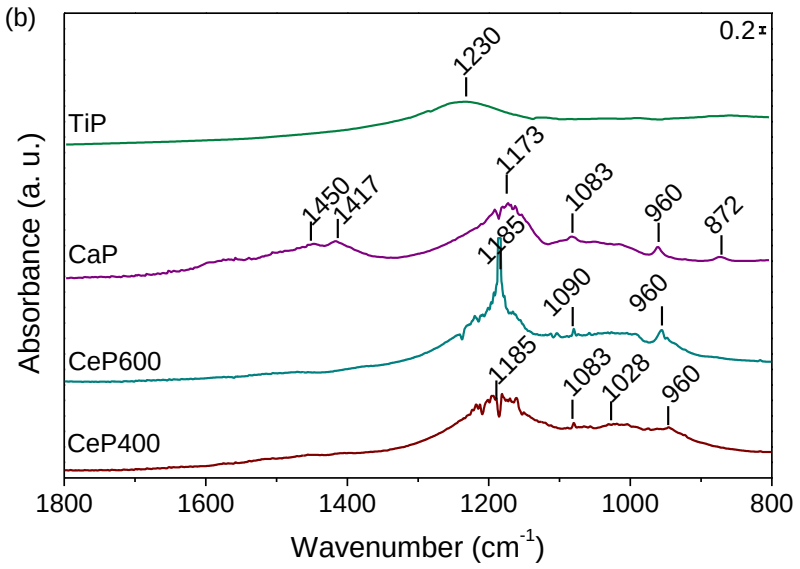

Figure 6.6. DRIFT spectra of the studied supports after the activation treatment under 10% H_2/Ar, taken at 150 °C under Ar atmosphere, a) 4000-2500 and b) 1800-800 cm^{-1} spectral regions

Table 6.3. Assignment of the supports vibration modes after the activation treatment

Solid	Band frequency (cm^{-1})	Assignment
CeP400 CeP600 CaP TiP	5319 5259 5345 -	Water combination bands $v + \delta(H_2O)$
CeP400 CeP600 CaP TiP	3670 3670 3568 3535 3740 (vw)	OH stretching
CeP400	2884	P-OH stretching of acid ortophosphates
CeP and CaP TiP	2400-2100 -	Overtone and combination bands of PO_4^{3-} vibrations
CeP400 CeP600 CaP TiP	1185 1185 1173 1230	P=O stretching
CeP400 CeP600 CaP TiP	1028 1090 1016-1083 -	P-O asymmetric stretching v_3 (P-O)
CeP and CaP	960	P-O symmetric stretching v_1 (P-O)
CaP	1448, 1417, 872	CO_3^{2-} vibrations

The behavior of the surface species in the presence of water was analyzed through the monitoring of the water adsorption experiments. Difference spectra of the supports (taking the spectra after the activation treatment as reference) are presented in figure 6.7. All the evaluated supports

present bands between 3500 and 2500 cm^{-1} characteristics of adsorbed molecular water. These bands are particularly weak in the support TiP, which shows the low affinity of water by this support and explains the low activity of the Pt/TiP catalyst on the WGS reaction. Although this support presents the greatest specific surface area value, the loss of phosphorous and the absence of mesopores in its structure suppose a poor interaction with the water molecules.

The spectra of CeP400 and CeP600 show the growth of bands at ca. 5300 cm^{-1} corresponding to water combination modes ($\nu + \delta(H_2O)$), indicating a great affinity of both solids with water in its molecular form. Additionally, these supports present a band in this region at relatively low frequency ($\sim$ 5200 cm^{-1}), which points out the presence of H-bonded H_2O species [40], as well as a weak and broad band about 4000 cm^{-1}, where combination modes of the -OH groups ($\nu + \delta(OH)$) appear. A negative band corresponding to the -OH stretching modes (3670 cm^{-1}) is observed in the presence of water, thus these -OH groups are participating in the hydrogen bonding. At the same time, a band at 3690 cm^{-1} appears, attributed to -OH groups belonging to the water molecule, since this band is contributing to the combination bands at 5318 cm^{-1} and 5259 cm^{-1} for CeP400 and CeP600, respectively. The observation of the H-O-H bending mode ($\delta_{H\text{-}O\text{-}H}$) region allows to determine also the type of interaction between the water molecule and the surface. Since the water molecule is amphoteric, it is able to interact with both acidic surface sites (through the lone pair electrons of the oxygen atom) and with basic sites (through the formation of hydrogen bonding). When the interaction occurs via hydrogen bonding, the $\delta_{H\text{-}O\text{-}H}$ mode shifts to higher wavenumbers while the interaction via the oxygen atom produces a shift of the $\delta_{H\text{-}O\text{-}H}$ mode towards lower wavenumbers [40-42]. According to that, the water in the solids CeP400 and CeP600 are interacting through hydrogen bonding, due to the high H-O-H bending mode frequencies at 1625 and 1630 cm^{-1} respectively. CeP400 spectrum shows also a band at 1586 cm^{-1} as the temperature increases.

Falk [42] found a relationship between the $\delta_{H\text{-}O\text{-}H}$ frequency shift and the formal charge of the cation with which the water molecules were interacting. For the cation Ce^{3+} this value would be found at ca. 1532 cm^{-1}, a value much lower than that found in this sample, thus this vibration mode has been assigned to the water present in the structural channels of the rhabdophane-type phase of $CePO_4$ [29]. Simultaneously to the growing of the water-related modes, the intensity of the overtone and combination bands of the phosphate groups (2100-2400 cm^{-1}) decrease in both

solids, which indicates that the water molecule is interacting with the phosphate groups. In CeP400 and CeP600, water seems to remain as molecular water in all the temperature range, pointing out that CeP supports present a diffusion mechanism, meaning that the proton transport is assisted by the translational dynamics of the water molecule [43, 44].

The spectrum of the support CaP presents also a combination band of the water modes (5319 cm^{-1}), but its intensity is lower than that of the supports CeP. In addition, a series of growing bands appear in the 3750-3600 cm^{-1} range (inset figure 6.7) when water is adsorbed, denoting the generation of new -OH groups and thus suggesting the ability of the hydroxyapatite for dissociating the water molecule, in contrast to the behavior showed by the CeP supports, where water species remain as molecular water [29].

As occurring in the solids CeP, a decrease in intensity of the overtone and combination bands of the phosphate group occurs, indicating the participation of the phosphate group in the interaction with water. Regarding the $\delta_{H\text{-}O\text{-}H}$ region, the spectrum shows two different contributions, one at 1642 cm^{-1}, corresponding to the bending mode of hydrogen-bonded species and another one at 1568 cm^{-1}. The average value of the $\delta_{H\text{-}O\text{-}H}$ mode interacting with a cation with charge 2+ should appear at 1560 cm^{-1} [42], close to the value found for this mode in the CaP spectrum. Consequently, this vibration could be assigned to that of the water molecules interacting via the lone electron pair of oxygen with the Ca^{2+} ions of the hydroxyapatite structure. This band remains even at 350 °C, exposing that this interaction is stronger than that via hydrogen bonding. This result allows to conclude that a Grotthuss mechanism could take place in the support CaP, i. e., the water molecules show pronounced local dynamics but they stay at their sites, being the protons transferred within hydrogen bonds from one molecule to another.

Liu et al. [45] have demonstrated that proton conduction properties can be tuned by controlling the crystal structure, porous network and chemical functionality of the conductor solids, thus, the differences observed in the studied phosphate-type supports can be ascribed to the differences in their crystallographic structure and porosity.

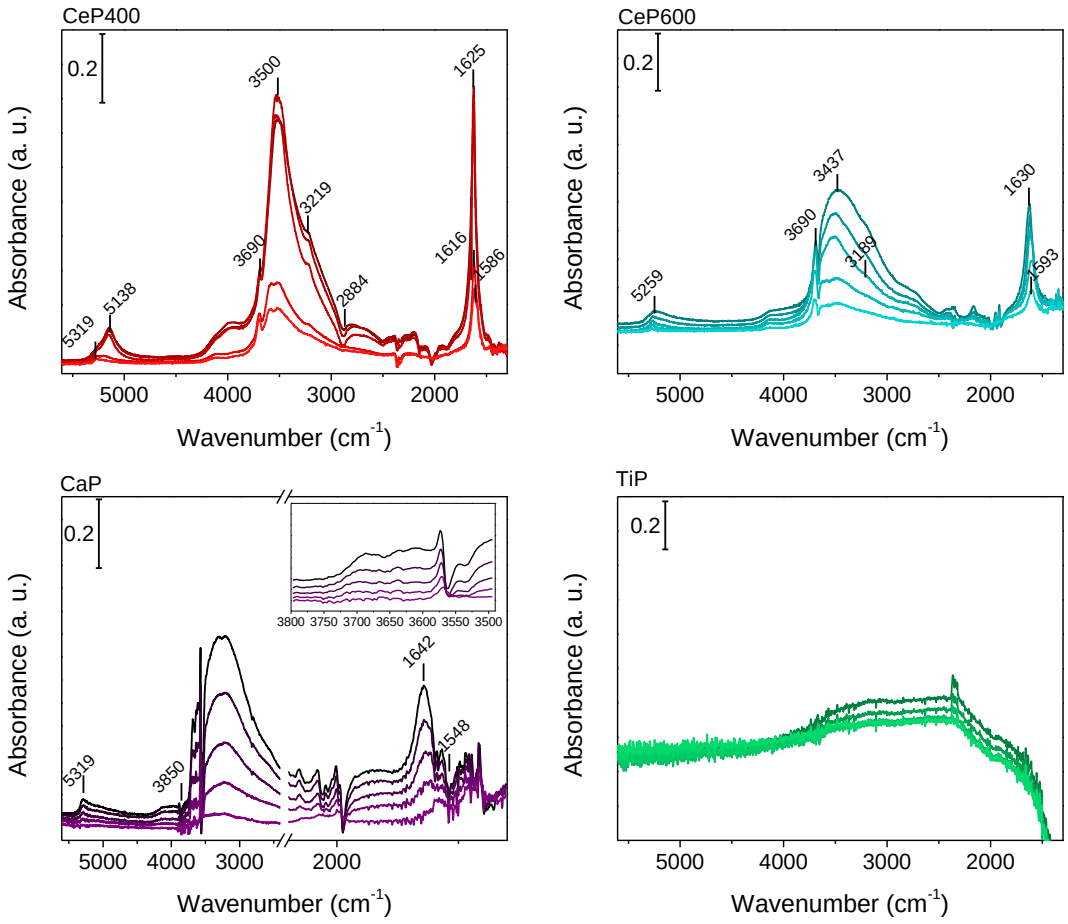

Figure 6.7. Evolution of the difference spectra of the supports during the adsorption of 10% H_2O/Ar, from 150°C (top) to 350°C (bottom)

The evolution of the relative intensity of the mass-on-charge (m/z) 18 during the water adsorption experiments, shown in Figure 6.8, is in agreement with the results described above. Water adsorption capacity of the evaluated supports decreases in the order: CaP > CeP400 > CeP600 > TiP, which coincides with the trend followed by the corresponding catalysts on the WGS reaction.

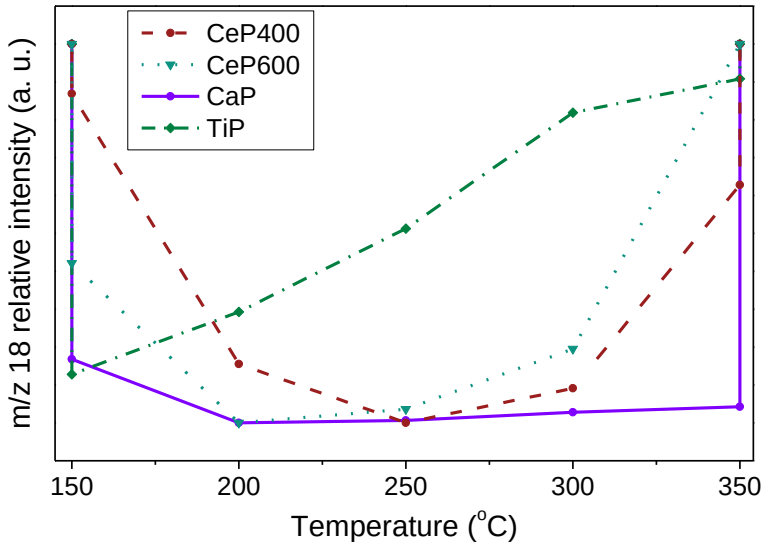

Figure 6.8. Evolution of the mass-on-charge (m/z) 18 as a function of the temperature during the adsorption of 10% H_2O/Ar

The support CaP shows an excellent water adsorption capacity, being able to greatly retain the water in the whole temperature range evaluated. This fact can be attributed to the interaction of the water molecule not only with the phosphate and -OH groups but also with the Ca^{2+} ions, as proved by DRIFTS. This result is in agreement with previous studies, which have demonstrated that calcium hydroxyapatite interacts strongly with the water molecule through electrostatic/hydrogen bonding with the Ca^{2+} and phosphate ions of the apatite surface. Furthermore, the charge density on the Ca^{2+} ions is more localized than on the phosphate groups in the presence of water, provoking a dramatical decrease on the water molecule mobility in the proximity of the apatite surface and thus favoring the retention of water on the structure even at high temperatures [46-48]. This fact added to the water dissociation ability of CaP allows a superior enhancement of the WGS catalytic performance. The support CeP400, however, reaches a maximum adsorption capacity at 250 °C, which decreases when this temperature is exceeded. As reported in Chapter IV [29], the hexagonal structure of $CePO_4$ has demonstrated a great interaction ability with the water molecule that has been attributed to the interaction of the latter with the phosphate groups of the support and the influence of their structural -OH groups. Since this support interacts with the water molecule uniquely by hydrogen bonding with the phosphate groups of the support and it is unable to dissociate the water molecule, it seems reasonable its lower catalytic performance. In addition, considering that the support CaP contains

a greater pore volume than CeP400, the interaction of water with the channels of this solid is favored. The support CeP600 shows a great affinity for water, although its adsorption capacity starts to decrease at 200 °C and is lower than that of CeP400 in all the temperature range. In spite of the interaction of the surface phosphate groups of the monoclinic phase of $CePO_4$ with the water molecule, the absence of the structural channels present in the hexagonal phase gives rise to a diminishing of the strength of this interaction. Finally, the support TiP presents a strong adsorption of water at 150 °C, which decreases drastically while the temperature increases. This fact could be attributed to the loss of phosphorous in this support during the calcination procedure and the subsequent impossibility of the water molecule to interact with the phosphate groups. Thus, the water retention capacity of the supports is directly related with the catalytic trend observed for the Pt catalysts in the WGS reaction and with the selectivity of the reaction. These results evidence the fundamental role of the water availability for an enhanced WGS catalytic performance, demonstrating that the WGS reaction could be improved through the modulation of the structural characteristics of the employed phosphate-type supports.

6.6. Partial conclusions

A series of phosphate-based compounds containing Ca and Ti have been used as supports for Pt catalysts, evaluated in the WGS reaction and compared with $CePO_4$ supports. Considering that the availability of water plays a fundamental role in the WGS reaction mechanism, the structure and water adsorption capacity of these supports have been related to the WGS catalytic performance. Results show that catalytic activity decreases in the order: Pt/CaP > Pt/CeP400 > Pt/CeP600 > Pt/TiP. Supports containing structural channels, that is CaP and CeP400, favor the interaction with water, although different mechanisms of interaction have been observed between both supports. CaP dissociates the water molecule, presenting the so-called “Grotthus” mechanism. In addition, the water interaction takes place via hydrogen bonding with the phosphate groups and via strong electrostatic interaction with the Ca^{2+} ion, which explains the superior catalytic activity of the Pt/CaP system. On the other hand, CeP400 retains water in its molecular form, thus presenting a diffusion mechanism. In this case, the water molecule is interacting via hydrogen bonding with the phosphate groups but not with the Ce^{3+} ion, and consequently giving rise to a relative decrease of the catalytic activity of the catalyst. When

channels are not present in the phosphate structure, as ocurring in the support CeP600, the interaction of water with the phosphate groups is weakened and thus the catalytic activity decreases. Finally, the support TiP experienced a loss of phosphorous during the calcination procedure, decreasing the surface phosphate population and consequently, the interaction with the water molecule and the WGS catalytic activity. These results expose that phosphate-type compounds constitute appropriate supports for WGS catalysts, allowing to enhance their interaction with the water molecule during the reaction through the tuning of their surface and structural properties.

6.7. References

1. Iriarte-Velasco, U., et al., *Transition metals supported on bone-derived hydroxyapatite as potential catalysts for the Water-Gas Shift reaction.* Renewable Energy, 2018. **115**: p. 641-648.

2. Ghahfarrokhi, A.M., P. Moshiri, and M. Ghiaci, *Studies on calcined cow bone and pyrolyzed wood, suitable supports for inmobilizing hybrid nanoparticles of Co-Mn as new catalysts for oxidation of 2,6-diisopropyl naphtalene.* Applied Catalysis A: General, 2013. **456**: p. 51-58.

3. Wijzen, F., et al., *Texture and Structure of Amorphous Co-Precipitated Silica-Aluminium Phosphate Catalyst Supports.* Journal of Catalysis, 1998. **177**: p. 96-104.

4. Kanai, S., et al., *A bifunctional cerium phosphate catalyst for chemoselective acetalization.* Chemical Science, 2017. **8**(4): p. 3146-3153.

5. Nagai, M. and T. Nishino, *Surface conduction of porous hydroxyapatite ceramics at elevated temperatures.* Solid State Ionics, 1988. **28**: p. 1456-1461.

6. Liu, D., K. Savino, and M.Z. Yates, *Microstructural Engineering of Hydroxyapatite Membranes to Enhance Proton Conductivity.* Advanced Functional Materials, 2009. **19**(24): p. 3941-3947.

7. Yamazoe, N. and Y. Shimizu, *Humidity sensors: Principles and Applications.* Sensors and Actuators, 1986. **10**: p. 379-398.

8. Horiuchi, N., et al., *Proton conduction related electrical dipole and space charge polarization in hydroxyapatite.* Journal of Applied Physics, 2012. **112**(7): p. 074901.

9. Bouhaouss, A., et al., *Mechanism of ionic conduction in oxy and hydroxyapatite structures.* International Journal of Inorganic Materials, 2001. **3**: p. 743-747.

10. Miao, D., et al., *Water-gas shift reaction over platinum/strontium apatite catalysts.* Applied Catalysis B: Environmental, 2017. **202**: p. 587-596.

11. Miao, D., A. Goldbach, and H. Xu, *Platinum/Apatite Water-Gas Shift Catalysts.* ACS Catalysis, 2016. **6**(2): p. 775-783.

12. Nalini, V., R. Haugsrud, and T. Norby, *High-temperature proton conductivity and defect structure of TiP2O7.* Solid State Ionics, 2010. **181**(11-12): p. 510-516.

13. Rodríguez-Castellón, E., et al., *Proton conductivity of mesoporous MCM type of zirconium and titanium phosphates.* Solid State Ionics, 1999. **125**: p. 407-410.

14. Hogarth, W., et al., *Proton conduction mechanism and the stability of sol–gel titanium phosphates.* Solid State Ionics, 2007. **177**(39-40): p. 3389-3394.

15. Lapina, A., et al., *Electrical conductivity of titanium pyrophosphate between 100 and 400 °C: effect of sintering temperature and phosphorus content.* Journal of Solid State Electrochemistry, 2013. **18**(1): p. 39-47.

16. Domínguez, M.I., et al., *Gold/hydroxyapatite catalysts: Synthesis, characterization and catalytic activity to CO oxidation.* Applied Catalysis B: Environmental, 2009. **87**(3-4): p. 245-251.

17. Romero-Sarria, F., et al., *CO oxidation at low temperature on Au/CePO4: Mechanistic aspects.* Applied Catalysis B: Environmental, 2011. **107**(3-4): p. 268-273.

18. Ren, T.-Z., et al., *Tailoring the Porous Hierarchy of Titanium Phosphates.* Langmuir, 2006. **22**.

19. Boukha, Z., et al., *Methane dry reforming on Ni loaded hydroxyapatite and fluoroapatite.* Applied Catalysis A: General, 2007. **317**(2): p. 299-309.

20. Wang, L., et al., *Structural and morphological transformations of mesostructured titanium phosphate through hydrothermal treatment.* Journal of Colloid and Interface Science, 2007. **316**(2): p. 954-961.

21. Takahashi, H., T. Oi, and M. Hosoe, *Characterization of semicrystalline titanium(iv) phosphates and their selectivity of cations and lithium isotopes.* Journal of Materials Chemistry, 2002. **12**(8): p. 2513-2518.

22. Kőrösi, L. and I. Dékány, *Preparation and investigation of structural and photocatalytic properties of phosphate modified titanium dioxide.* Colloids and Surfaces A: Physicochemical and Engineering Aspects, 2006. **280**(1-3): p. 146-154.

23. Leofanti, G., et al., *Surface area and pore texture of catalysts.* Catalysis Today, 1998. **41**: p. 207-219.

24. Elliot, J.C., *Structure and Chemistry of the Apatites and other Calcium Ortophosphates*. 1994: Elsevier Science.

25. *Handbook of Heterogeneous Catalysis*. 2nd edition ed, ed. G. Ertl, et al. Vol. 1. 2008: Wiley-VCH.

26. Horváth, I., A. Bondar, and L.P. Mezentseva, *Termochemistry of Hydrated Rare Earth Ortophosphates.* Journal of Thermal Analysis, 1988. **33**: p. 755-760.

27. Mooney, R.C.L., *X-ray Diffraction Study of Cerous Phosphate and Related Crystals. I. Hexagonal modification.* Acta Crystallographica, 1950. **3**: p. 337-340.

28. Mooney, R.C.L., *Crystal Structures of a Series of Rare Earth Phosphates.* The Journal of Chemical Physics, 1948. **16**(10): p. 1003-1003.

29. Navarro-Jaén, S., et al., *Pt/CePO4 catalysts for the WGS reaction: influence of the water-supplier role of the support on the catalytic performance.* Journal of Materials Chemistry A, 2018. **6**: p. 17001-17010.

30. *Hydroxyapatite and related materials*, ed. P.W. Brown and B. Constantz. 1994: CRC Press.

31. Parapat, R.Y., et al., *Support effect in the preparation of supported metal catalysts via microemulsion.* RSC Adv., 2014. **4**(92): p. 50955-50963.

32. Ratnasamy, C. and J.P. Wagner, *Water Gas Shift Catalysis.* Catalysis Reviews, 2009. **51**(3): p. 325-440.

33. Dayanand, C., et al., *Structural investigations of phosphate glasses: a detailed infrared study of the x(PbO)-(1-x)P2O5 vitreous system.* Journal of Materials Science, 1996. **31**: p. 1945-67.

34. Nazaraly, M., et al., *Synthesis and characterization of CeIV(PO4)(HPO4)0.5(H2O)0.5.* Journal of Physics and Chemistry of Solids, 2006. **67**(5-6): p. 1075-1078.

35. Baddiel, C.B. and E.E. Berry, *Spectra structure correlations in hydroxy and fluorapatite.* Spectrochimica Acta, 1966. **22**: p. 1407-1416.

36. Ishikawa, T., M. Wakamura, and S. Kondo, *Surface characterization of calcium hydroxylapatite by Fourier transform infrared spectroscopy.* Langmuir, 1989. **5**(1): p. 140-144.

37. Bertinetti, L., et al., *Surface Structure, Hydration, and Cationic Sites of Nanohydroxyapatite: UHR-TEM, IR, and Micrograviметric Studies.* Journal of Physical Chemistry C, 2007. **111**: p. 4027-4035.

38. Low, M.J.D. and P. Ramamurthy, *Infrared study of the surface properties of phosphoric acid impregnated silica.* Journal of Physical Chemistry, 1968. **72**: p. 3161-3167.

39. Berzina-Cimdina, L. and N. Borodajenko, *Infrared Spectroscopy- Materials Science, Engineering and Technology*, ed. T.M. Theophanides. 2012: InTech.

40. Vimont, A., et al., *Investigation on Acid Sites in a Zeotypic Giant Pores Chromium(III) Carboxylate.* Journal of the American Chemical Society, 2006. **128**: p. 3218-3227.

41. Burneau, A., *Near infrared spectroscopic study of the structures of water in proton acceptor solvents.* Journal of Molecular Liquids, 1990. **46**: p. 99-127.

42. Falk, M., *The frequency of the H-O-H bending fundamental in solids and liquids.* Spectrochimica Acta, 1984. **40A**: p. 43-48.

43. Kreuer, K.-D., *Proton Conductivity: Materials and Applications.* Chemistry of Materials, 1996. **8**: p. 610-641.

44. Kreuer, K.-D., et al., *Transport in Proton Conductors for Fuel-Cell Applications: Simulations, Elementary Reactions, and Phenomenology.* Chemical Reviews, 2004. **104**: p. 4637-4678.

45. Liu, M., et al., *Three-dimensional protonic conductivity in porous organic cage solids.* Nature Communications, 2016. **7**: p. 12750.

46. Zahn, D. and O. Hochrein, *Computational study of interfaces between hydroxyapatite and water.* Physical Chemistry Chemical Physics, 2003. **5**(18): p. 4004-4007.

47. Zhao, W., et al., *Surface energetics of the hydroxyapatite nanocrystal-water interface: a molecular dynamics study.* Langmuir, 2014. **30**(44): p. 13283-92.

48. Bolis, V., et al., *Coordination chemistry of Ca sites at the surface of nanosized hydroxyapatite: interaction with H2O and CO.* Philosophical Transactions of the Royal Society A, 2012. **370**(1963): p. 1313-36.

General Conclusions

$CePO_4$ has been successfully synthesized by a hydrothermal method. By calcination at 400 and 600 °C, the rhabdophane ($CePO_4 \cdot nH_2O$) and monazite-type ($CePO_4$) phases of this solid have been obtained.

Characterization results demonstrate that the rhabdophane-type phase (CeP400) contains a series of structural channels along the (100) plane, in which water molecules are located. On the contrary, the calcination treatment at higher temperature provokes the complete dehydration of the rhabdophane-type phase, giving rise to the formation of the monazite-type one (CeP600), in which the structural channels are vanished. Differences in the structural features of both phases influence their water adsorption capacity, which is greater for the phase containing channels. Despite these differences, both solids present only Ce^{3+} in their structure, ruling out the presence of the Ce^{3+}/Ce^{4+} redox pair typically observed in CeO_2.

Afterwards, 2 wt.% Pt catalysts supported on both $CePO_4$ phases (Pt/CeP400 and Pt/CeP600) have been prepared by wet impregnation. Characterization results show that the supports characteristics remain unaltered after the deposition of the metal. Additionally, homogeneous Pt particle size distributions have been obtained in both solids, with mean particle sizes of *ca.* 1 nm. Interestingly, Pt particles in the rhabdophane-based catalyst seem to follow the direction of the structural channels of the support, suggesting a preferential arrangement of the metal particles in this solid.

The prepared supports and Pt catalysts have been evaluated in the WGS reaction. Whereas supports presented no activity, Pt catalysts were highly active and selective, not being observed the formation of methane in any case. However, the catalytic activity of the Pt/CeP400 catalyst is superior to that of Pt/CeP600.

In order to evaluate the interaction of the water molecule with the solids in the WGS temperature range, *in situ* water adsorption experiments followed by DRIFTS were performed. Results showed a greater adsorption capacity of CeP400 with respect to CeP600, although the dissociation of the water molecule does not take place on these solids. Adsorption experiments on the Pt catalysts showed similar results to the corresponding supports, although some changes are observed in the phosphate overtone/combination bands region, indicating that the interaction of the phosphate groups with water are influenced by the presence of Pt.

Operando DRIFTS results of the supports in the presence of CO and H_2O demonstrated no formation of intermediates in all the temperature range; additionally, no CO_2 was detected at the exit cell, in agreement with the catalytic activity results. For the Pt catalysts, formate-intermediate species are formed. Since new OH groups are not formed on the support, the dissociation of the water molecule seems to occur on the Pt particles, positioning the $CePO_4$ supports as water suppliers.

With the purpose of understanding the structural characteristics of the solids influencing the reaction mechanism, $^{18}O_2/^{16}O_2$ and $C^{18}O_2/C^{16}O_2$ experiments were performed. Results using $^{18}O_2$ point out the absence of oxygen vacancies on the supports in the WGS temperature range, which is in agreement with the presence of uniquely Ce^{3+} in these solids and discard the possibility of a redox mechanism, where the oxygen vacancies play an important role regarding the dissociation of the water molecule. In the presence of Pt, no significative changes are observed.

However, both the supports and Pt catalysts present a great oxygen exchange capacity when using $C^{18}O_2$, suggesting an associative mechanism as the preferred path in these solids, in good agreement with the DRIFTS studies. In every case, the exchange capacity of the CeP400-based solids is superior to that of the CeP600-based systems, although the presence of Pt on CeP400 induces a decrease of the exchange extent. The lower exchange capacity of CeP600-based systems has been explained by the formation of carbonate species on the solids surface, which could block active sites for the formation of hydrogen carbonates. For the same reason, the decrease of the exchange in Pt/CeP400 with respect to CeP400 is related to the presence of carbonates in the surface. Since hydrogen carbonates are the intermediate species giving rise to the exchange reactions, it is possible to conclude that the oxygen atoms of the OH groups are those participating in the exchange.

Finally, Pt catalysts supported on phosphate-type supports containing Ca (CaP) and Ti (TiP) as cations are explored and compared to the $CePO_4$-based systems. The WGS catalytic activity decreases in the order: Pt/CaP > Pt/CeP400 > Pt/CeP600 > Pt/TiP. The greater catalytic activity of Pt/CaP and Pt/CeP400 has been attributed to the presence of channels in the support structure, which favors the availability of water during the WGS reaction. However, different interaction mechanisms with the water molecule have been observed. The CaP system interacts with water

not only through the phosphate groups, but also through the Ca^{2+} ion. This interaction is particularly strong and favors the retention of water. Furthermore, this support dissociates the water molecule, whereas such behavior is not observed on CeP400. This fact explains the greater catalytic activity of the Pt/CaP catalyst during the WGS reaction. The lower catalytic activity of Pt/CeP600 is explained by the absence of channels in the CeP600 support, which supposes a weaker interaction with the water molecule. Finally, the Pt/TiP catalyst present a low catalytic activity, not reaching a 10% CO conversion even at 350 °C. This result is explained by the loss of phosphorous in the TiP support induced by the calcination treatment, which supposes an insignificant interaction of the water molecule with this support.

Resumen

1. Introducción

La problemática generada por el uso de combustibles fósiles, relacionada con el agotamiento de éstos y los problemas medioambientales derivados de su uso, ha dado lugar a la búsqueda de fuentes de energía alternativas. En este contexto, el hidrógeno resulta un sustituto interesante, debido a que es una energía limpia, puede almacenarse y transportarse de manera segura y posee un alto valor calorífico (122 $kJ \cdot g^{-1}$) [1, 2].

Dicho hidrógeno es producido generalmente a través de procesos de reformado, lo cual implica la presencia de otros componentes no deseados en la corriente, tales como el monóxido de carbono. Por tanto, la purificación de la corriente de hidrógeno constituye un paso fundamental [3, 4]. Para ello, la reacción de desplazamiento de gas de agua o *Water-Gas Shift* (WGS, Ec. 1.1) resulta de gran importancia, ya que retira la mayor parte del monóxido de carbono y, simultáneamente, enriquece la corriente en hidrógeno [5].

$$CO + H_2O \leftrightarrow CO_2 + H_2 \qquad \text{(Ec. 1.1)}$$

Por tanto, este proceso es utilizado tanto a escala industrial como dentro de la tecnología de celda de combustibles. El uso de estas últimas resulta de gran interés, ya que consisten en dispositivos capaces de convertir la energía química del hidrógeno en energía eléctrica [6].

Dentro del contexto de las celdas de combustible, los catalizadores más eficaces han demostrado ser aquellos usando metales nobles como fase activa. Entre ellos, los sistemas que contienen Au y Pt han demostrado ser los más eficaces en los rangos de baja y media temperatura, respectivamente [7]. Además de la fase activa, la influencia de los soportes catalíticos utilizados también ha sido ampliamente estudiada [8-10]. A este respecto, se ha concluido de manera general que el comportamiento catalítico de los sólidos en la reacción de WGS se debe a un efecto sinérgico entre fase activa y soporte [11, 12]. Por tanto, las características electrónicas y estructurales de los catalizadores empleados determinan el comportamiento catalítico en la reacción de WGS y, en consecuencia, el mecanismo de reacción de ésta.

La reacción de WGS puede transcurrir, de manera general, a través de dos mecanismos: el mecanismo redox o disociativo, y el mecanismo asociativo o regenerativo [13].

En el mecanismo redox, el CO es adsorbido en los sitios metálicos, difunde a la interfase metal/soporte y reacciona con el oxígeno de la red de soporte, produciendo CO_2. Este paso da lugar a la formación de vacantes de oxígeno y, por tanto, a la reducción del soporte. El H_2O, por su parte, se adsorbe disociativamente en los sitios reducidos del soporte, reoxidándolo y dando lugar a la producción de H_2.

En el mecanismo asociativo, el CO y el H_2O son adsorbidos en los sitios activos del catalizador, dando lugar a la formación de intermedios de reacción, tales como carbonatos, bicarbonatos o formiatos, los cuales reaccionan o se descomponen para dar los productos de reacción, CO_2 e H_2 [14].

Sea cual sea el mecanismo de reacción a través del cual transcurre la reacción, el paso limitante de la velocidad en el proceso de WGS es la disociación de la molécula de H_2O [5, 15]. Por tanto, el conocimiento del mecanismo de reacción resulta crucial, con el fin de facilitar dicho paso limitante y diseñar catalizadores activos y selectivos en la reacción de WGS.

En este aspecto, trabajos previos han puesto de manifiesto el papel determinante de la presencia de vacantes de oxígeno en el soporte. Así, el uso de CeO_2 como soporte para catalizadores de WGS ha sido resaltado en la literatura, gracias a sus propiedades electrónicas, es decir, la presencia del par redox Ce^{3+}/Ce^{4+} en su estructura, que favorece la presencia de ciclos redox y, en consecuencia, la formación de vacantes de oxígeno, que facilitan la disociación del agua [12]. Además, se ha demostrado que la formación de vacantes de oxígeno se ve favorecida por la adición de dopantes en la estructura del CeO_2, los cuales dan lugar a una mejora en la concentración de especies OH y H durante la reacción de WGS [16].

Siguiendo en esta línea, trabajos posteriores han puesto de manifiesto el interés de usar conductores iónicos como soporte de catalizadores para WGS. Dichos conductores consisten en óxidos de tierras raras dopados con cationes aliovalentes, los cuales dan lugar a una excelente mejora en cuanto a la concentración de vacantes de oxígeno [17].

De acuerdo con estos estudios, dos conceptos podrían ser de gran importancia para el diseño de nuevos catalizadores para WGS: la presencia de Ce y, en consecuencia, la posible influencia del par redox Ce^{3+}/Ce^{4+}, y la adición de conductores iónicos en la formulación. De esta manera, la utilización de $CePO_4$ como soporte para la reacción de WGS podría resultar interesante, dada

la presencia de Ce en su estructura y el uso previo de los fosfatos de tierras raras como membranas protónicas en celdas de combustible [18]. Estos factores podrían influenciar el comportamiento de los sistemas catalíticos con respecto a la molécula de agua y, en consecuencia, el desempeño catalítico de éstos y el mecanismo de la reacción de WGS.

Además, el $CePO_4$ puede presentar dos estructuras cristalinas. La fase *rhabdophane* pertenece al sistema cristalino hexagonal, y presenta una serie de canales estructurales a lo largo del eje *c*, donde se alojan moléculas de agua. La fase *monazita* pertenece al sistema monoclínico, y surge como resultado de la deshidratación total de la fase *rhabdophane*, lo cual da lugar a la desaparición de dichos canales [19, 20]. La Figura 1 presenta una representación de ambas estructuras.

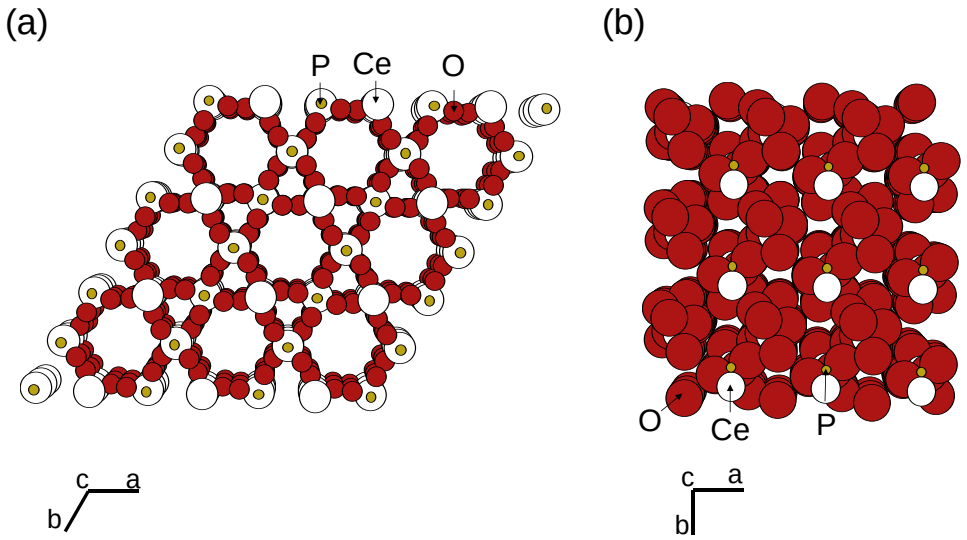

Figura 1. Vista a lo largo del eje *c* de las posibles fases del $CePO_4$, (a) Rhabdophane, (b) Monazita

2. Estructuración de la Tesis Doctoral

El presente trabajo de investigación ha sido estructurado en seis capítulos:

El capítulo I presenta la introducción y motivación de esta tesis doctoral;

En el capítulo II, los principios de las técnicas de caracterización empleadas, así como las condiciones de medida utilizadas, son especificadas. De la misma manera, se presenta el

dispositivo experimental en el que se llevan a cabo los test catalíticos y se especifican las condiciones de reacción utilizadas;

El capítulo III recoge la síntesis de los materiales y los resultados obtenidos mediante las distintas técnicas de caracterización empleadas;

En el capítulo IV se presentan los resultados de actividad catalítica durante la reacción de WGS, así como un estudio mediante espectroscopía infrarroja de la interacción del agua y los reactivos de la reacción de WGS con los sólidos sintetizados.

El capítulo V presenta los resultados obtenidos mediante experimentos de intercambio isotópico usando $^{18}O_2$ y $C^{18}O_2$, con el fin de relacionar la movilidad de oxígeno en los sólidos con el mecanismo de reacción observado en los sólidos.

En el capítulo VI, el estudio del $CePO_4$ se extiende a otros soportes tipo fosfato conteniendo Ca y Ti en su estructura. Sus características estructurales, la interacción con la molécula de agua y la actividad catalítica en la reacción de WGS son evaluadas y comparadas con las de los sistemas basados en $CePO_4$.

3. Resultados representativos y breve discusión

En este apartado se presentan algunos de los resultados más representativos del presente trabajo.

En primer lugar, se ha llevado a cabo la síntesis de las dos posibles estructuras cristalinas del $CePO_4$ empleadas como soportes catalíticos: la fase hexagonal (rhabdophane, $CePO_4 \cdot nH_2O$) y la fase monoclínica (monazita, $CePO_4$), denominadas CeP400 y CeP600 a lo largo del trabajo. La formación de ambas estructuras ha sido confirmada mediante distintas técnicas de caracterización (Capítulo III).

De acuerdo con los resultados de caracterización, la principal diferencia estructural entre ambos materiales reside en la presencia de una serie de canales paralelos a lo largo del plano (100) en la fase CeP400, que desaparecen en la fase CeP600, de acuerdo con las micrografías TEM presentadas en la Figura 2.

A pesar de las diferencias estructurales entre ambos soportes, los análisis por XPS demuestran que en ambos soportes el Ce se encuentra en estado de oxidación +3, descartando la presencia del par redox Ce^{3+}/Ce^{4+} típicamente observado en CeO_2. Los resultados se recogen en la Figura 3.

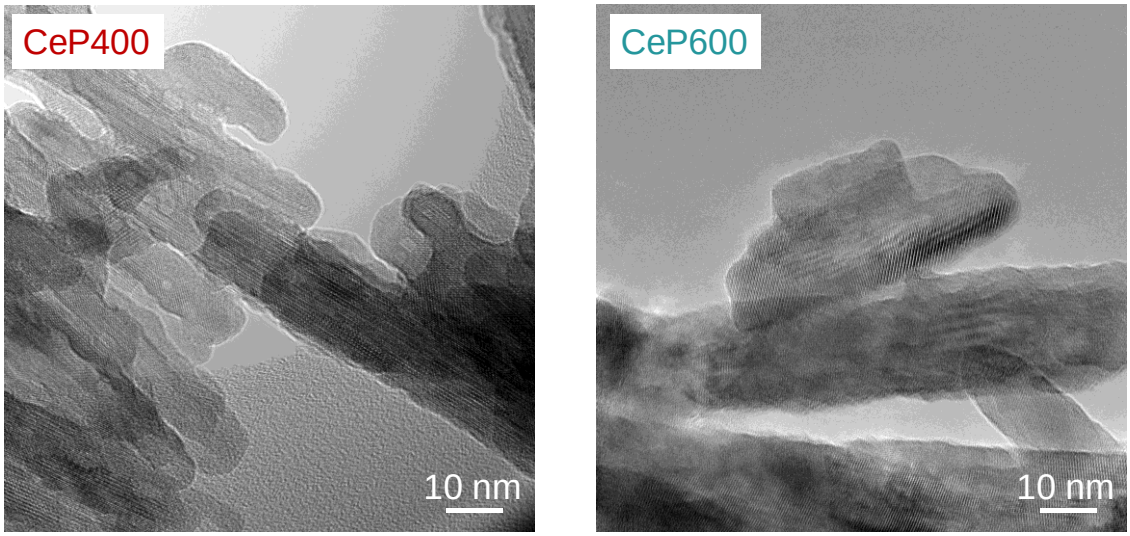

Figura 2. Micrografías TEM de los soportes

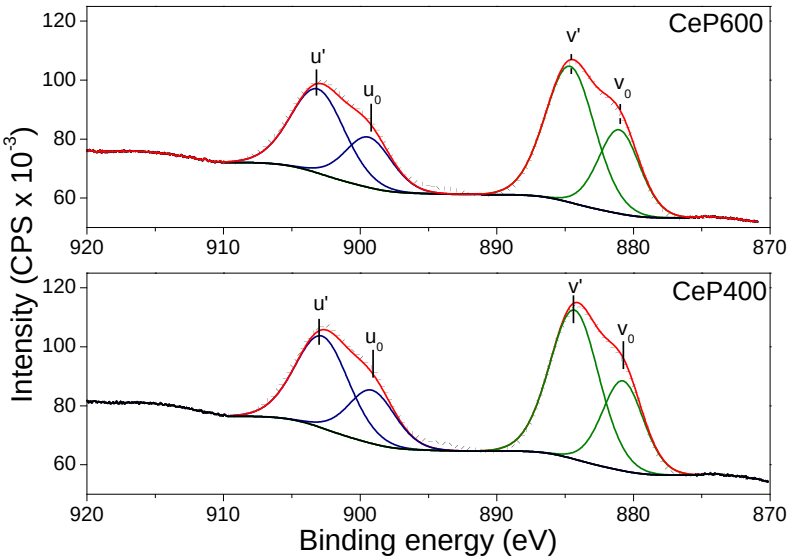

Figura 3. Región Ce 3d del espectro XPS de los soportes

Posteriormente, los consiguientes catalizadores de Pt con un contenido nominal de 2% p/p fueron preparados mediante impregnación húmeda. El contenido de Pt de las muestras ha sido determinado mediante ICP. En ambos casos, las cargas de metal han sido cercanas a las

nominales (Capítulo III). Las características estructurales de los soportes no se han visto modificadas tras el depósito de Pt y las especies metálicas no han sido detectadas mediante XRD, lo que confirma el pequeño tamaño de cristalito de las especies metálicas, de acuerdo con los resultados mostrados en la Figura 4. Además, se obtuvo una distribución de tamaño de partícula de Pt en ambas muestras, con un tamaño promedio de aproximadamente 1 nm, de acuerdo con las micrografías de TEM presentadas en el capítulo III.

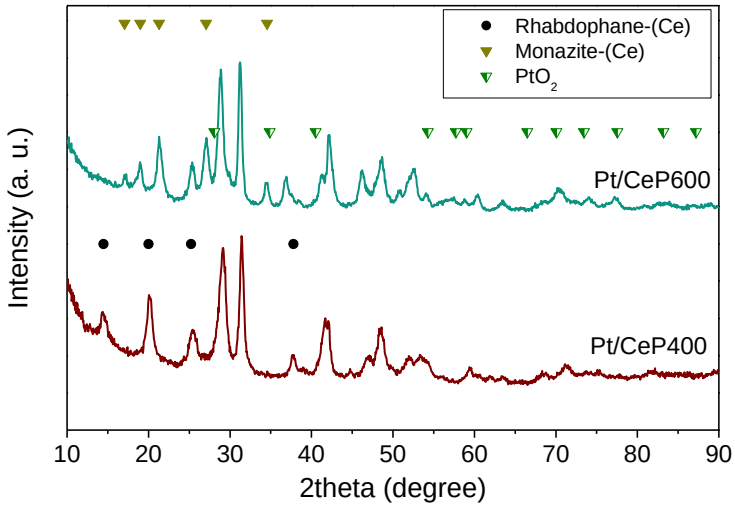

Figura 4. Patrones de difracción de rayos X de los catalizadores de Pt

La actividad catalítica de los soportes y catalizadores sintetizados fue evaluada en la reacción de WGS. Mientras que los soportes no presentaron actividad, ambos catalizadores demostraron ser altamente activos y selectivos, no observándose en ningún caso formación de metano. En todas las condiciones evaluadas, el desempeño catalítico del catalizador Pt/CeP400 fue superior al del sólido Pt/CeP600, como se muestra en la Figura 5.

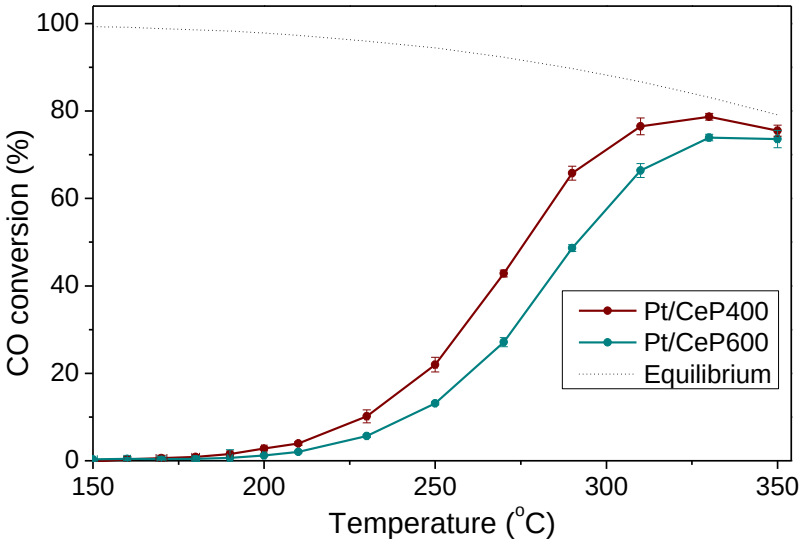

Figura 5. Conversión de CO en función de la temperatura en presencia de la corriente B (7% CO, 9% CO_2, 30% H_2O, 50% H_2 y 4% N_2)

Con el fin de elucidar el papel del agua durante la reacción de WGS, se llevaron a cabo experimentos de adsorción de H_2O seguidos por DRIFTS (Capítulo IV). Bandas asociadas a la presencia de agua molecular son observadas en los espectros de ambos soportes, situadas a 5200-5100 cm^{-1}, 3500-3200 cm^{-1} y 1625 cm^{-1}. La evolución de la altura de estas bandas (5200 y 1625 cm^{-1}) en función de la temperatura se muestra en la Figura 6.

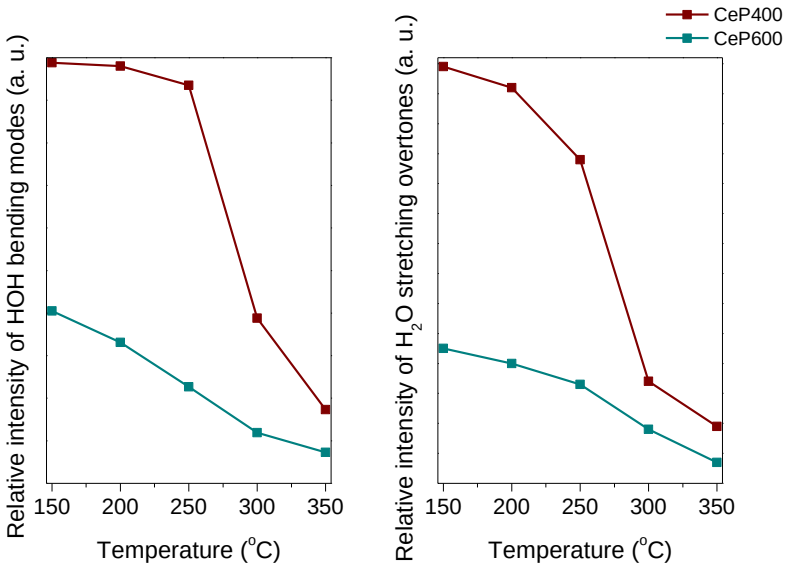

Figura 6. Evolución de las bandas relacionadas con el agua en función de la temperatura durante los experimentos de adsorción de H_2O

En el rango de temperaturas estudiado, la capacidad de adsorción de H_2O del soporte CeP400 es significativamente superior que la del soporte CeP600, de acuerdo con la presencia de canales estructurales que favorecen la retención del agua en este sólido. No obstante, en ningún caso se observa la formación de nuevos grupos OH, lo cual indica que los soportes no disocian la molécula de agua, actuando como proveedores de agua durante la reacción de WGS.

De acuerdo con estos resultados, los estudios IR *operando* en presencia de la mezcla de reacción muestran que el mecanismo de la reacción de WGS en ambos sólidos tiene lugar a través de un mecanismo asociativo, siendo los intermedios de reacción especies formiato (Capítulo IV). Esto sugiere que la disociación de agua en estos sólidos tiene lugar en los sitios metálicos.

Los resultados de intercambio isotópico con oxígeno muestran que en presencia de la molécula marcada $^{18}O_2$ ni soportes ni catalizadores intercambian oxígeno en el rango de temperatura de la reacción de WGS, lo cual pone de manifiesto la ausencia de vacantes de oxígeno en estos sólidos, de acuerdo con la presencia de solo Ce^{3+} en los soportes. Esto explica que la molécula de agua no sea disociada en el soporte. Sin embargo, cuando la molécula marcada es $C^{18}O_2$, el intercambio tiene lugar muy rápidamente mediante la formación de bicarbonatos superficiales, tanto en soportes como en catalizadores, lo cual concuerda con el mecanismo asociativo observado mediante DRIFTS. Ejemplos representativos del soporte CeP400 se muestran en la Figura 7.

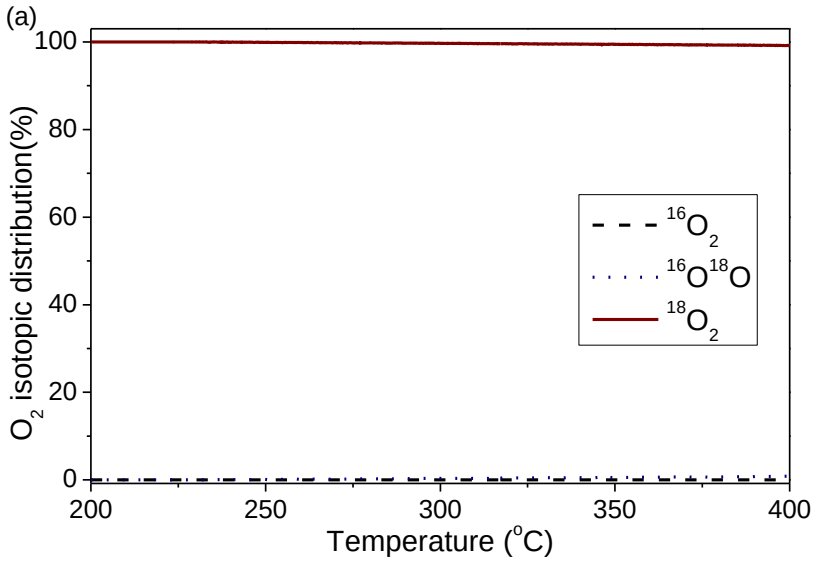

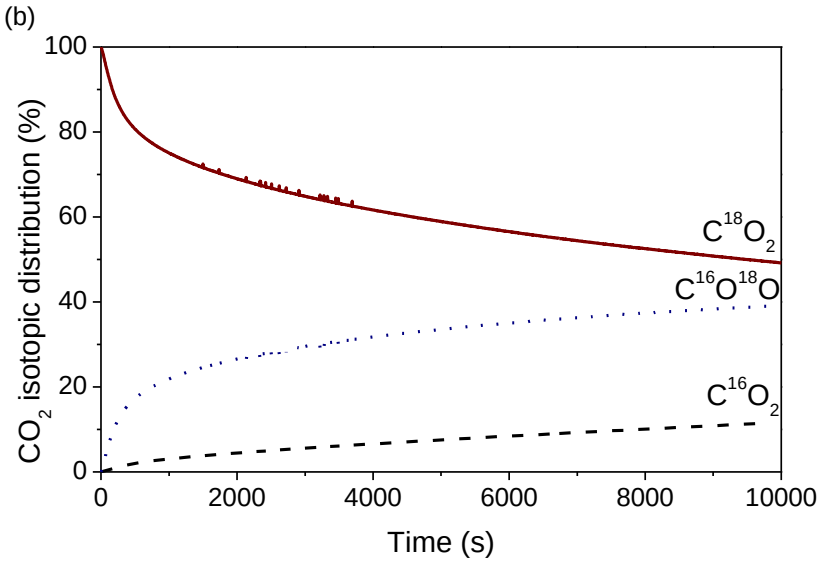

Figura 7. Distribución isotópica de (a) O_2 y (b) CO_2 durante los experimentos de intercambio isotópico sobre el soporte CeP400

Tras el análisis de los sólidos basados en $CePO_4$, el capítulo V hace un análisis de la posible extrapolación de estos resultados a otros sistemas tipo fosfato conteniendo Ca (CaP) y Ti (TiP). El sólido CaP presenta la estructura cristalina del hidroxiapatito cálcico, mientras que el sólido TiP es amorfo y pierde fósforo durante el tratamiento de calcinación (Capítulo VI). Los resultados de actividad catalítica de los correspondientes catalizadores de Pt demuestran que el catalizador soportado sobre CaP presenta el mejor desempeño catalítico, seguido de Pt/CeP400 y Pt/CeP600. El catalizador Pt/TiP presenta muy baja actividad (Capítulo VI).

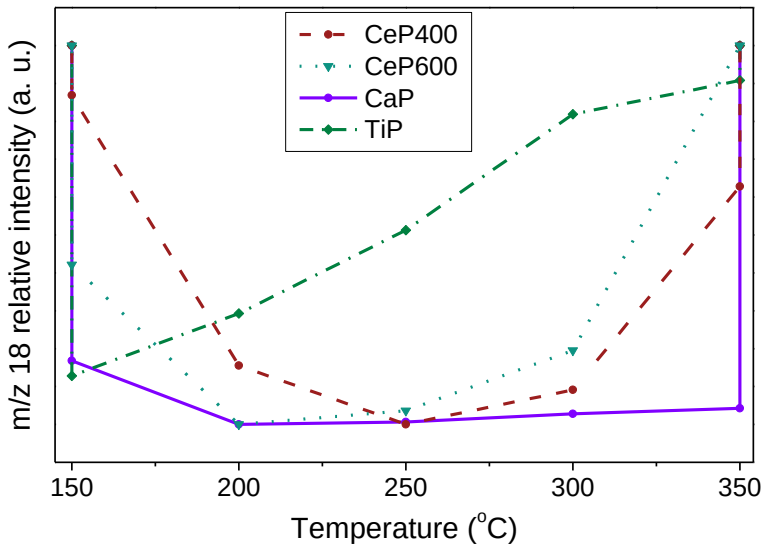

Figura 8. Evolución de la relación masa-carga 18 (H_2O) en función de la temperatura durante los experimentos de adsorción de H_2O

Estos resultados se relacionan con la capacidad de adsorción de agua de cada soporte registrada por espectrometría de masas (Figura 8). Dichos resultados ponen de manifiesto la posible extrapolación de los resultados obtenidos en el $CePO_4$ a otros sistemas basados en fosfato y su aplicación en la reacción de WGS.

4. Referencias

1. Han, S.-K. and H.-S. Shin, *Biohydrogen production by anaerobic fermentation of food waste.* International Journal of Hydrogen Energy, 2004. **29**: p. 569-577.

2. Turner, J.A., *Sustainable Hydrogen Production.* Science, 2004. **305**: p. 972-974.

3. Song, C., *Fuel processing for low-temperature and high-temperature fuel cells: Challenges and opportunities for sustainable development in the 21st century.* Catalysis Today, 2002. **77**: p. 17-49.

4. González-Castaño, M., et al., *O 2 -assisted Water Gas Shift reaction over structured Au and Pt catalysts.* Applied Catalysis B: Environmental, 2016. **185**: p. 337-343.

5. González-Castaño, M., et al., *Tailoring structured WGS catalysts: Impact of multilayered concept on the water surface interactions.* Applied Catalysis B: Environmental, 2018. **222**: p. 124-132.

6. Ratnasamy, C. and J.P. Wagner, *Water Gas Shift Catalysis.* Catalysis Reviews, 2009. **51**(3): p. 325-440.

7. Smirniotis, P. and K. Gunugunuri, *Water Gas Shift Reaction: Research Developments and Applications*. 1st ed. 2015: Elsevier.

8. Andreeva, D., et al., *Low temperature water gas shift reaction over Au-α-Fe_2O_3.* Journal of Catalysis, 1998. **158**: p. 354-355.

9. Boccuzzi, D.F., et al., *Gold, silver and copper catalysts supported on TiO_2 for pure hydrocarbon production.* Catalysis Today, 2002. **75**: p. 169-175.

10. Panagiotopoulou, P. and D.I. Kondarides, *Effect of the nature of the support on the catalytic performance of noble metal catalysts for the water–gas shift reaction.* Catalysis Today, 2006. **112**(1-4): p. 49-52.

11. Grenoble, D.C., M.M. Estadt, and D.F. Ollis, *The Chemistry and Catalysis of the Water Gas Shift Reaction, 1. The Kinetics over Supported Metal Catalysts.* Journal of Catalysis, 1981. **67**: p. 90-102.

12. Vecchietti, J., et al., *Understanding the Role of Oxygen Vacancies in the Water Gas Shift Reaction on Ceria-Supported Platinum Catalysts.* ACS Catalysis, 2014. **4**(6): p. 2088-2096.

13. Bunluesin, T., R.J. Gorte, and G.W. Graham, *Studies of the water-gas-shift reaction on ceria-supported Pt, Pd and Rh: Implication for oxygen storage properties.* Applied Catalysis B: Environmental, 1998. **15**: p. 107-114.

14. Kalamaras, C.M., et al., *Effects of Reaction Temperature and Support Composition on the Mechanism of Water–Gas Shift Reaction over Supported-Pt Catalysts.* The Journal of Physical Chemistry C, 2011. **115**(23): p. 11595-11610.

15. Mandapaka, R. and G. Madras, *Zinc and platinum co-doped ceria for WGS and CO oxidation.* Applied Catalysis B: Environmental, 2017. **211**: p. 137-147.

16. González-Castaño, M., et al., *Deep insight into Zr/Fe combination for successful Pt/CeO2/Al2O3WGS catalyst doping.* Catalysis Science & Technology, 2017. **7**(7): p. 1556-1564.

17. García-Moncada, N., et al., *A direct in situ observation of water-enhanced proton conductivity of Eu-doped ZrO 2 : Effect on WGS reaction.* Applied Catalysis B: Environmental, 2018. **231**: p. 343-356.

18. Anfimova, T., et al., *Thermal Stability and Proton Conductivity of Rare Earth Ortophosphates Hydrates.* International Journal of Electrochemical Science, 2014. **9**: p. 2285-2300.

19. Mooney, R.C.L., *Crystal Structures of a Series of Rare Earth Phosphates.* The Journal of Chemical Physics, 1948. **16**(10): p. 1003-1003.

20. Mooney, R.C.L., *X-ray Diffraction Study of Cerous Phosphate and Related Crystals. I. Hexagonal modification.* Acta Crystallographica, 1950. **3**: p. 337-340.